# The Back-Forward Drivable Torsion Torque Control of Two-Inertia System For Environment Interaction

Yusuke KAWAI

February, 2020

# Table of Contents

# List of Figures

# List of Tables

# Chapter1

# Introduction

## 1.1 Background

In the future, the increasing world population is expected according to the United Nations. Meanwhile, the aging population has been increasing in recent years and various problems such as productivity and a lowering of the quality of life (QoL) have been progressing [1]. Especially, not only Japanese population is decreasing, but also aging population is increasing; thus, worker population is also decreasing [2].

For such problems, automation of human tasks by the robot has been expanding in industrial fields until now, e.g., welding, handling, transporting in the manufacturing lines. This automation has mainly used position/velocity control of the robot. Position/velocity control is high servo stiffness and the contact objects or the actuator may be broken when contacting the environment. Therefore, flexible interaction with an environment is not able to be realized. So far, industrial robots have been used in the fence that human does not enter. Moreover, to expand the productivity, the force control realizes some applications, such as assembling mechanical parts, grasping, polishing, etc [3, 4]. However, such applications are often used in the fence.

According to the International Federation of Robotics [5], the installation of robots is expanding and not only manufacturing applications but also cooperative applications have attracted attention

in the industrial fields [6–10]. The introduction of cooperative robots is progressing in the factory for helping labor forces. In the past years, the lightweight and flexible manipulator is developed in cooperative robots of industrial fields. However, the number of cooperative robots installed is still very low.

Moreover, in recent years, cooperative robots for human-robot interaction are also expanding in non-industrial fields, such as medical and welfare fields [11–25]. Sankai has developed Hybrid Assistive Limb (HAL) for augmenting power of normal persons [17, 18]. The Berkeley Lower ExtremityExoskeleton (BLEEX) is developed by Kazerooni *et al.* as exoskeleton for military applications [19, 20]. Kong *et al.* has proposed exoskeleton for patients and old people at Sogang university (EXPOS) [21]. The exoskeleton is developed based on tendon-driven actuator [22, 23]. Kong *et al.* has proposed human-assist system (SUBAR) that has large assist torque [24]. Welfare utilization by robotic technology is also considered as important issues in the Ministry of Economy, Trade, and Industry [26]. Most important things when using the robots are safety against contacting human and objects in the coexistence of human and robots.

Human support systems, such as rehabilitation and collaborative/cooperative robots, are essential to improve our QoL for industrial as well as non-industrial fields. In particular, such applications require solving issues below.

- Back drivability
- Robustness against environmental stiffness variation
- Stable contact realization without bouncing from free motion.

First, back drivability [27] is defined as a characteristic of being pushed back in a flexible manner according to the force applied to the actuator. Thus, when realizing high back drivability, it is easy to manipulate the robot arm by human hands, easily. Moreover, impact torque is reduced. Second, robust force control is required for stable contact and pushing motion against various environments because recently, automation of human tasks by robots as well as human-robot interaction, such as

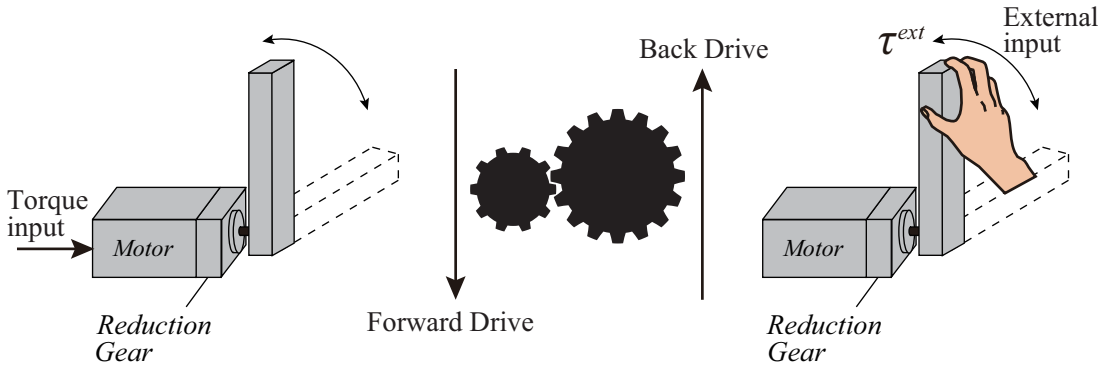


Figure1.1: Schematic of forward and back drivable motions.

collaborative/cooperative tasks by robots are increasing. There are human impedance and hard objects, such as iron, rubber, and so on in the environments. Therefore, robustness against the various environments is important in force control system. Third issue is also related to second issue. Free motion includes human operation, such as direct teaching motion, and command response of the control system in non-contact with the environment. It is well known that high-performance force control system is acceleration-based force control. However, velocity response becomes lamped signal when step force command is added in the case of acceleration-based force control. Actually, the realization of contact control by the constant velocity is important because contact velocity affects impact torque, greatly. Therefore, even though the force control on the acceleration dimension is realized, it is necessary to provide a force control system is capable of stable contact for the environment at a constant velocity. To achieve a stable contact realization without bouncing, velocity and acceleration need to be brought to zero after contact with an environment.

In this study, force control approaches for three issues are considered. Firstly, back drivability is discussed. Fig.1.1 shows the schematic of forward and back drivable motions.

In Fig.1.1, a forward drive means normal actuator control that operates according to a command signal. In contrast, back drive means the actuator control that operates according to a external signal, i.e.,disturbance or load-side input characteristics. Therefore, realizing high back drivability means that the robot actuator is able to be easily manipulated by human hand, and the impact force is able to

be reduced when in contact with the environment. However, the robot requires a high torque density for high precision, high speed, and assistance by the robot such as a powered exoskeleton. Therefore, the reduction gear is used for the robot. However, back drivability is deteriorated owing to the friction increased by the reduction gear.

To overcome these disadvantages, various approaches have been proposed: 1) the development of a new actuator that has back drivability [28–36], 2) a direct drive motor that does not have reduction gear [37–39], and 3) an improvement in the back drivability using a robot combined with a load-side sensors [40–44].

For 1), a high-power and back-drivable electro-hydrostatic actuator has been developed [30, 31]. Such approaches are focused on the development of a high back drivable actuator. In addition, both force sensitivity and back drivability are evaluated for the development of actuator [32]. This back drivable actuator is also applied to humanoid robot [33], and the effectiveness is experimentally verified. The SEA proposed by Pratt *et al.* satisfies the compliance requirement by using a spring mounted on the load-side of the gear [34]. Moreover, Kong *et al.* has developed a rotary SEA and human-assist motion is realized based on force regulation and disturbance observer (DOB) [24, 35]. Moreover, Miura *et al.* have developed series clutch actuator (SCA) [36]. By controlling clutch current, motor-side and load-side are able to be separated and back drivability is improved. A spiral motor with high-thrust and high back drivability has been developed [37]. However, it is not easy to introduce a new back drivable actuator for industrial and rehabilitation/medical fields from the perspective of view of implementation.

For 2), a direct drive motor is used in haptics in particular [38,39] because it is easy to achieve high back drivability and high operability; however, a direct drive motor has low-torque density. Thus, the size of the motor increases in the case of human-robot interactions such as rehabilitation and for a powered exoskeleton, which requires a large amount of torque.

Approach 3) is easy to introduce in many fields because the load-side sensors (e.g., acceleration sensor [40], torsion torque sensor [41, 42], and double encoder [43, 44]) are simply combined with

an existing robot. In addition, the costs of sensors become low in recent years. Some researchers have proposed compliance control and force control for improving the back drivability. Additionally, theoretical evaluation of back drivability is conducted and the back drivability is usually validated experimentally [32, 45]. In [45], ideal back drivability is realized by zeroing the backdrive-resistance defined by the dynamics of the reduction gear, and this manuscript focuses on the development of reduction gear that has a small backdrive-resistance. In [32], enhancing the force sensitivity is required to improve the back drivability and it is necessary to reduce the effect of friction. Although the improvement of the back drivability is validated, theoretical analysis of the ideal drivability in the control system is not discussed fully. Moreover, back drivability is not discussed, but improvement of robot compliance is demonstrated by shaping potential energy through motor position feedback as well as shaping motor inertia through joint torque feedback [46]. In [46], the authors have focused on impedance behavior such as mass, damper, and spring.

In stable contact motion, compliance controls that include an impedance control [47–57] and a control method that switches between position/velocity and force controls are used [58–63]. Compliance control is effective for interaction to the environmental objects, but it is known that compliance control becomes unstable in case of stiff environments [56, 57]. Position and force controls are switched considering the initial values of the integrators for each controller [59]. In addition, position and force controls are smoothly switched based on the known contact point [60]. For switching control systems and for emergency stop for robots, collision detection methods have been proposed [61–63]. Collision detection methods use momentum-based disturbance observer and an impedance control is used after collision detection [62]. However, it is difficult to construct a control system without a switching controller that is able to stop the actuator in a continuous/smooth fashion after contacting the environment for human-robot interaction such as direct teaching and rehabilitation, etc. Switching controller-less control methods are promising for realizing smooth contact motion. Cascade force control and compliance control are effective for stable contact realization, such as direct teaching and rehabilitation, but force response is slow and back drivability is also low. This is because of using

velocity feedback or virtual viscosity that reduce the back drivability.

Meanwhile, for cooperative and human-robot interaction applications, the realization of the stable contact is also needed, and such applications that use force/torque controls have gained popularity in both industrial and non-industrial fields. These include polishing, deburring, and assembling in human task automation, and there are direct teaching and collaborative operations in human-robot interaction [3,4,9,10]. As these applications consider the contact motion against the environment, it is necessary to consider the environmental dynamics when designing the force control system that includes contact motion, such as teaching operation including contact with the environment for polishing motion as one of the application tasks. Generally, the robot actuators are modeled as a two-inertia system. Thus, stable force control requires vibration suppression for these applications [64–72]. The state feedback is widely used for vibration suppression [65, 66]. Moreover, the vibration suppression method has been proposed based on wave equation [70, 71]. Two degrees of freedom (DoF) control based on DOB have been proposed [67–69]. The resonance ratio control (RRC) proposed by Yuki *et al.* is used as an effective vibration suppression method [64, 72, 73]. In this RRC, the resonance ratio in position control is determined as $\sqrt{5}$ and the motor-side inertia is regulated by the resonance ratio gain. The RRC achieves a robust and smooth position control. On the other hand, the resonance ratio in force control is determined as $\sqrt{6}$ and smooth force control is achieved [64]. However, this control system needs an inverse system to achieve smooth force control. The RRC in [64, 72] is constructed using acceleration control based on DOB [75, 76]. Meanwhile, in recent years, the sensor has made strides in accuracy and cost efficiency. The double encoder system provides vibration suppression by self-resonance cancellation [77]. Vibration suppression using acceleration sensor is also developed [78]. Moreover, force control for contact with environment is improved by acceleration [79–81]. The spring ratio control has been proposed by combining instantaneous state observer (ISOB) based on an acceleration sensor for stable force control [40]. In addition, the smooth contact control including contact process is proposed by switching force control and velocity controls [82].

## 1.2 Motivation of This Dissertation

In the previous section, the environmental interaction control requires satisfying back drivability, robustness against environmental stiffness variation, stable contact realization without bouncing free motion. However, the environmental interaction control that satisfies three issues has not been proposed. In addition, in recent years, owing to improved cost and performance of the sensors in terms of safety and reliability, it is hopeful for a further stable human-friendly system. The research objective in this dissertation is to realize the stable environmental interaction control that satisfies the above issues using a geared surface permanent magnetic synchronous motor (SPMSM) with a torsion torque sensor [83], which is mounted at the load side of the gear shaft.

**High Back-Forward Drivable Torsion Torque Control**

As mentioned in previous section, the back drivability is experimentally discussed, but ideal back drivability in the control system is not discussed fully. Especially, force control based on acceleration control is well known as the robust force control. This control concept is based on the Newton's law, i.e., $F = ma$, not including spring and damper. However, back drivability is not discussed on the dimension of acceleration. Moreover, definition of back drivability in the two-inertia system is not suitable for evaluating the environmental interaction control. In the dissertation, drivability for two-inertia system is defined as bidirectional drivability matrix, firstly. Load-side input characteristics are important for evaluating the environmental interaction performance in the control system. Thus, back-forward drivability, i.e., $a_l/\tau_l^{ext}$ is focused to evaluate the environmental interaction control. In addition, the vibration has occurred in case of using conventional back-forward drivable control based on acceleration control. To realize the ideal back-forward drivability, back-forward drivable torsion torque control is proposed for achieving vibration suppression as well as back-forward drivability. This approach is designed neglecting the environmental dynamics. Back-forward drivable response is drastically improved by back-forward drivable torsion torque control.

**High-Robust Back-Forward Drivable Torsion Torque Control against Environmental Stiffness Variation**

For realizing stable contact and pushing motion for various environment, it is necessary to consider the environmental dynamics in the force control design. Moreover, the manipulator modeled as two-inertia system needs vibration suppression control. Conventionally, force control based on RRC and ISOB using acceleration sensor is proposed. This approach uses the external torque feedback and back-forward drivability on acceleration is realized. However, there is unstable condition against environmental stiffness variation. In the dissertation, equivalent RRC (ERRC) is proposed based on the torque-velocity duality for improving robustness of environmental stiffness variation. The ERRC is constructed from two-spring system using motor-side velocity control. Motor-side velocity control is collocated side; therefore, back-forward drivable torsion torque control using ERRC is proposed and the control stability is improved. As a result, robustness of environmental stiffness variation is improved.

**Stable Contact Realization using Force Impulse Based on Back-Forward Drivable Torsion Torque Control**

To achieve stable contact motion without bouncing to the environmental object, the switching controller or compliance controller is mainly used. However, realizing stable contact control using only a single controller is hopeful for reducing the control complexity. Compliance control deteriorates the back drivability due to the use of impedance parameters, including damper. Thus, back drivable and stable force control system is required. For stable contact realization without bouncing phenomena, velocity and acceleration need to be brought to zero after contact with the environment. However, in case of focusing on Newton's law: $F = ma$, acceleration is also regulated to zero, but velocity does not become zero when the force is regulated to zero. This is because velocity has two conditions: $\omega = 0$ or $\neq 0$ when $a = 0$. It means ideal back drivable control is not able to realize the stable contact motion because bouncing phenomena has occurred when contacting the environment. Therefore, for achieve the stable contact motion, force impulse is focused and stable contact control using force im-

pulse based on back-forward drivable torsion torque control is proposed because that velocity is also controlled by controlling force impulse. The force impulse control based on back-forward drivable torsion torque control realizes both stable contact and back drivable motions, such as direct teaching operation for polishing motion.

## 1.3 Chapter Organization of The Dissertation

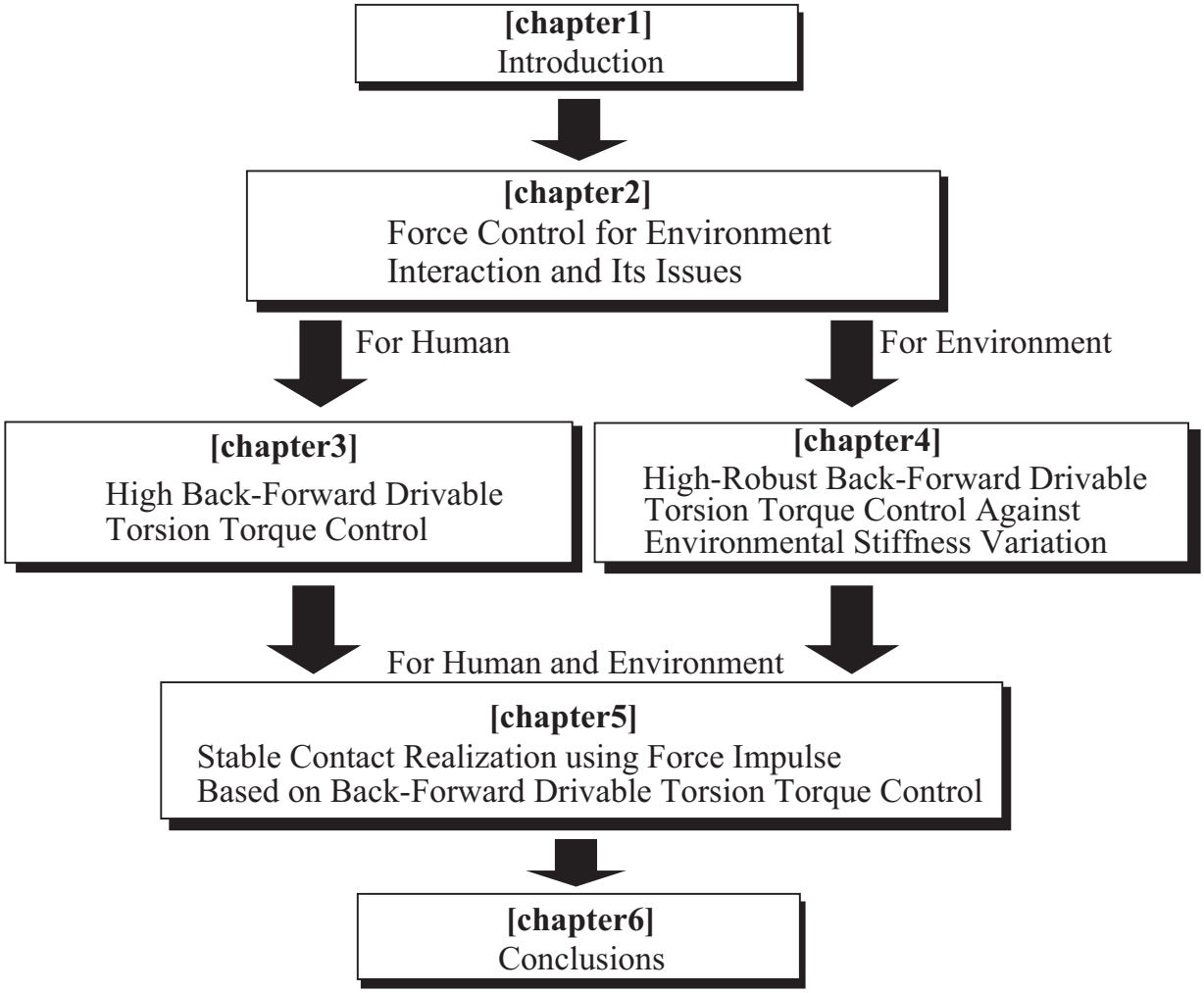


Figure1.2: Overview of dissertation.

The dissertation is organized as shown in Fig.1.2. Chapter 1 introduces the background and objective of the research. The outline of the Thesis is also described.

Chapter 2 discusses ideal drivability in single- and two-inertia systems focusing on acceleration-based force control. This chapter describes the force control system based on external torque feedback that has back-forward drivability on acceleration. Conventional force control systems for environment interaction are indicated. The environment includes humans and contact objects, such as iron, rubber, and so on. This chapter discusses some problems of conventional force control in human and environmental interactions. Furthermore, this chapter indicates the back-forward drivable torsion torque control that is the proposal in this dissertation. The force control approaches that satisfy three targets are realized by the back-forward drivable torsion torque control.

Chapter 3 focuses on only realizing ideal drivability, and high back-forward drivable torsion torque control is proposed. Proposed back-forward drivable torsion torque control achieve the vibration suppression while maintaining back-forward drivability defined in the dissertation. The effectiveness of proposed method is verified through the numerical simulations and experiments.

Chapter 4 describes the high-robust back-forward drivable torsion torque control against the environmental stiffness variation. This force control is based on the torque-velocity duality and is designed considering environmental dynamics for ensuring the robustness against the environmental stiffness variation. The effectiveness of proposed approach is verified through robust stability analysis using open-loop characteristics, numerical simulations and experiments.

Chapter 5 discusses the force control approach that realizes the back-forward drivability and stable contact realization. This approach employs the force impulse controller based on back-forward drivable torsion torque control. This target example is considered as a direct teaching operation for polishing motion. The proposed stable contact control is constructed by the force impulse controller based on the torsion torque controller and ERRC. Therefore, back-forward drivability, as well as the robustness of environmental stiffness variation, are also achieved. The stable contact motion is verified by numerical simulations and experiments.

Finally, in Chapter 6, the contribution of the dissertation is summarized and future issues are described.

# Chapter2

# Force Control for Environment Interaction and Its Issues

## 2.1 Introduction

This dissertation aims to realize high back-forward drivable torsion torque control systems for applications of environment interaction, such as direct teaching for polishing motion, as shown in Fig.2.1. There are humans, soft objects, hard objects, etc, in the environment. For environment interaction, the flexibility of the robots that are capable of external input and interaction to the various environments is required. Currently, force control design considering the vibration modes of the manipulator is required according to the high performance of robot motion control. The motion control

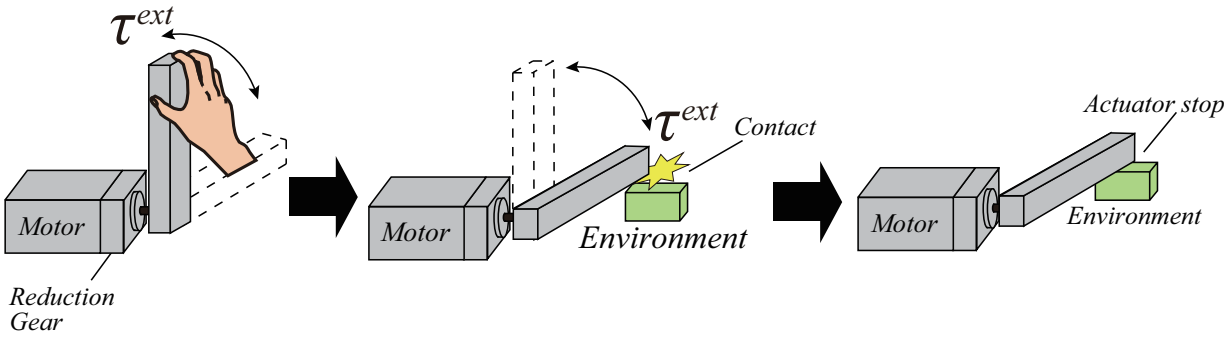


Figure2.1: Example of interaction control from free motion to stable contact with the environment.

of the manipulator so far utilizes position/velocity controls. Therefore, a force control system employs the cascade force control that is designed at the outer loop of position/velocity controls from the ease of introduction in industrial fields. The cascade force control is applied for assembling, deburring, pushing applications. In addition, compliance control is also utilized based on position/velocity control in minor loop. These systems are a cascade-type control system, and stable contact motion is realized. However, the control bandwidth of minor-loop is limited due to vibration modes in the plant system. As a result, control performance in force/compliance controls of the outer loop is also limited by the control performance of the minor-loop system. Back-forward drivable control system is not able to be achieved.

In this dissertation, a conventional high-performance force control approach that is not cascade system is discussed and some issues are summarized to improve the performance of environmental interaction control. This chapter firstly introduces the general force control based on acceleration control.Force control based on acceleration control is discussed on single- and two-inertia system. In addition, to achieve stable contact with environmental objects, force control design is required considering the environmental dynamics. Currently, the RRC is widely utilized for vibration suppression and stable force control based on RRC has been proposed for a two-inertia system with the environment. However, robustness against the environmental stiffness variation is not considered. In this chapter, conventional force control based on RRC is discussed and some issues are summarized. Finally, to overcome the above issues, back-forward drivable torsion torque control is discussed in this dissertation.

## 2.2 Force Control Based on Acceleration Control in Single-Inertia System for Human Interaction

First of all, force control based on acceleration control in single-inertia system is discussed. Acceleration control is generally realized based on the DOB. Force control based on acceleration control is

widely used for real world haptics, industrial application and human-robot interaction. Fig.2.2 shows the block diagram of DOB in single-inertia system.

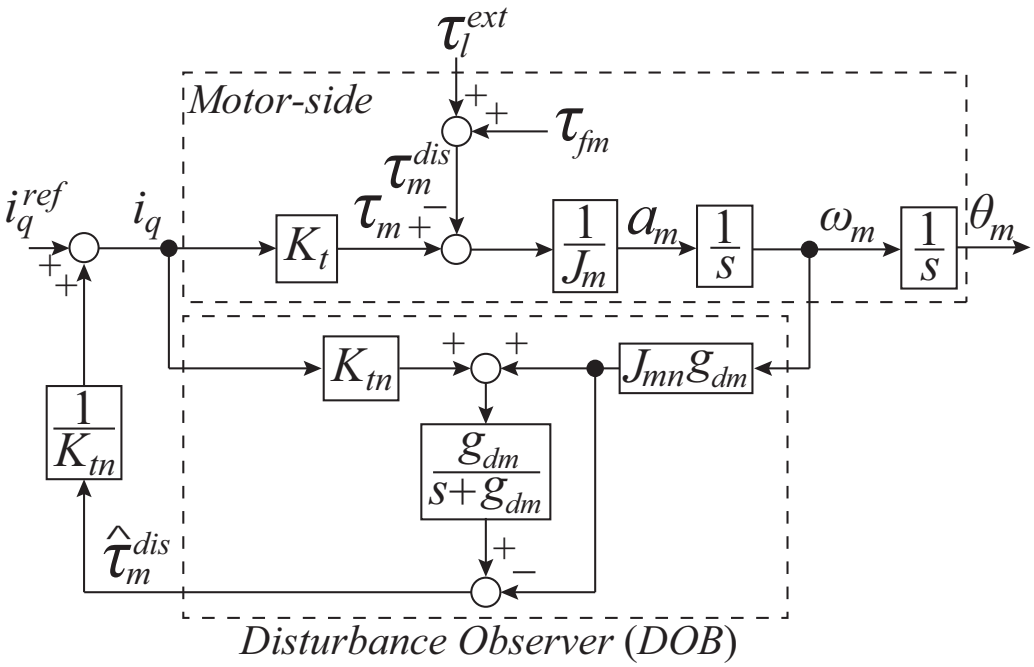


Figure2.2: Block diagram of DOB in single-inertia system.

In this figure, $K_t$, $J_m$, $g_{dm}$ denote the torque constant, motor-side inertia, and bandwidth of DOB, respectively. Here, the motor-side disturbance $\tau_m^{dis}$ is defined as

$$\tau_m^{dis} = \tau_l^{ext} + \tau_{fm} + \Delta J_m s\omega_m - \Delta K_t i_q \tag{2.1}$$

$$\tau_{fm} = D_m\omega_m + \tau_f, \tag{2.2}$$

where $\Delta J_m$, $\Delta K_t$, $\tau_l^{ext}$, $\tau_{fm}$, $D_m$, and $\tau_f$ are motor-side inertia variation, torque constant variation, external torque, friction torque, motor-side viscosity, and nonlinear friction. The motor-side disturbance $\tau_m^{dis}$ is estimated using current $i_q$ and motor-side velocity $\omega_m$ as follows:

$$\hat{\tau}_m^{dis} = \frac{g_{dm}}{s+g_{dm}}(K_{tn}i_q + J_{mn}g_{dm}\omega_m) - J_{mn}g_{dm}\omega_m. \tag{2.3}$$

From (2.3), the DOB estimates the motor-side disturbance $\tau_m^{dis}$ using motor current $i_q$ and motor-side velocity $\omega_m$. The motor-side disturbance is able to be compensated by feeding back the estimated

disturbance torque to motor current; thus, the motor-side parameters are normalized and robust control system is realized. Here, the estimation dynamics $L_{dm}$ of DOB is calculated as

$$L_{dm}(s) = \frac{\hat{\tau}_m^{dis}}{\tau_m^{dis}} = \frac{g_{dm}}{s + g_{dm}}. \tag{2.4}$$

Then, force control based on acceleration control is shown in Fig.2.3.

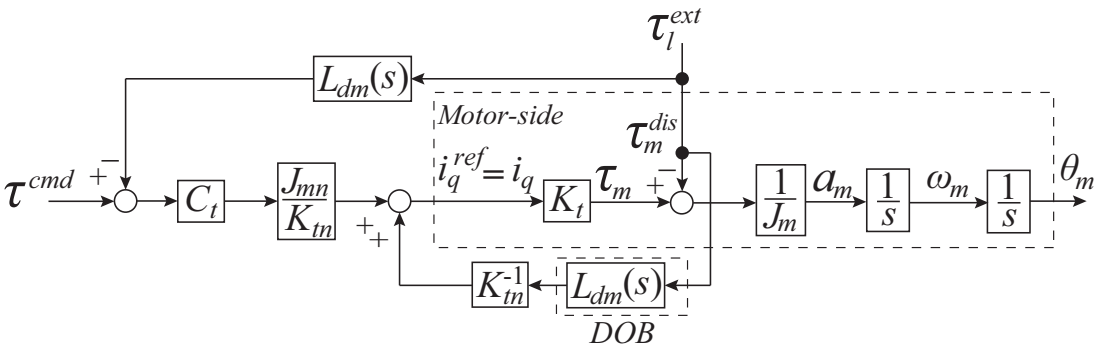


Figure2.3: Block diagram of DOB-based torque control in one-mass system.

Here, let us consider the back drivability of force control system in Fig.2.3, where the motor-side disturbances except the external torque is neglected. According to [27], back drivability is defined as a characteristic of being pushed back in a flexible manner according to the force applied to the actuator. In Fig.2.3, back drivability is able to be defined as the characteristics from external torque $\tau_l^{ext}$ to the motor-side acceleration $a_m$. Thus, the back drivability $G_b(s) = a_m/\tau_l^{ext}$ is derived as

$$G_b(s) = \frac{a_m}{\tau_l^{ext}} = -C_t L_{dm}(s) - \frac{1}{J_m}(1 - L_{dm}(s)) = -\frac{1}{J_m}\frac{s + J_m C_t g_{dm}}{s + g_{dm}} \tag{2.5}$$

From (2.5), torque gain $C_t$ is set to $C_t = 1/J_m$. Then, (2.5) is rewritten as

$$G_b(s)\Big|_{C_t = 1/J_m} = \frac{a_m}{\tau_l^{ext}}\Big|_{C_t = 1/J_m} = -\frac{1}{J_m}\frac{s + J_m C_t g_{dm}}{s + g_{dm}} = -\frac{1}{J_m}. \tag{2.6}$$

Therefore, back drivability is equivalent to single-inertia system without friction. This means human feels the resistive force of only single inertia and human is easy to manipulate the actuator. Therefore, the realization of ideal back drivability is to normalize single inertia without friction.

Meanwhile, actual manipulator is modeled as two-inertia system. Ideal drivability is considered in two-inertia system.

## 2.3 Force Control Based on Acceleration Control in Two-Inertia System for Human Interaction

### 2.3.1 Definition of Ideal Drivability

From previous section, ideal back drivability is assumed under Newton's law of $F = ma$, not including the friction and spring, and back drivability is defined as the characteristics from external torque $\tau_l^{ext}$ to the motor-side acceleration $a_m$. This is because the characteristics from the external side to the actuator side are evaluated.

Here, this section considers back drivability in two-inertia system shown in Fig.2.4.

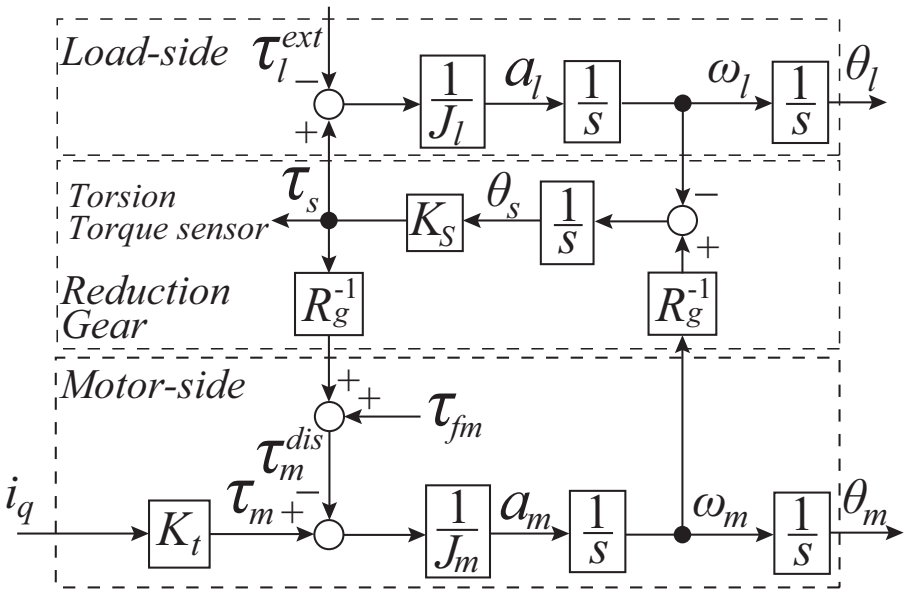


Figure2.4: Block diagram of two-inertia system.

In Fig.2.4, two-inertia system has two inputs and two outputs. Input signals are motor torque $\tau_m$ and the external torque $\tau_l^{ext}$. Output signals are motor-side acceleration $a_m$ and load-side acceleration $a_l$. However, the back drivability is defined as the external torque $\tau_l^{ext}$ to the motor-side acceleration $a_m$, i.e., $G_b(s) = a_m/\tau_l^{ext}$. When evaluating the human-interaction performance, the motion of the robot is easy to understand by evaluating the load-side output, intuitively. Therefore, human-robot

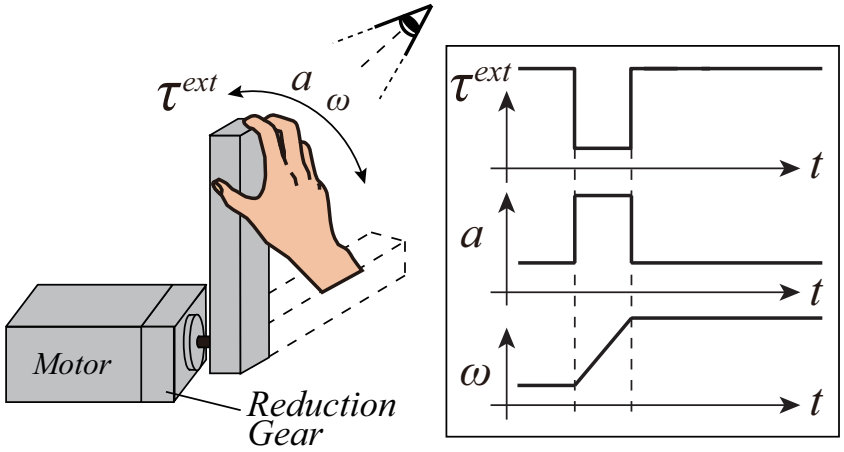


Figure2.5: Concept of back-forward drivable motion.

interaction performance in the two-inertia system is not able to be evaluated by the back drivability. Thus, the controlled system for two-inertia system is evaluated using the bidirectional drivability matrix (BDM) [84], as shown in (2.7).

$$\begin{bmatrix} a_l \\ a_m \end{bmatrix} = \begin{bmatrix} G_{bf}(s) & G_f(s) \\ G_b(s) & G_{fb}(s) \end{bmatrix} \begin{bmatrix} \tau_l^{ext} \\ \tau_m \end{bmatrix} \tag{2.7}$$

where $a_m$, $a_l$, $\tau_m$, and $\tau_l^{ext}$ denote the motor-side acceleration, load-side acceleration, motor-side torque, and external torque, respectively. The matrix elements are: $G_{bf}(s) = a_l/\tau_l^{ext}$: back-forward drivability, $G_b(s) = a_m/\tau_l^{ext}$: back drivability, $G_f(s) = a_l/\tau_m$: forward drivability, and $G_{fb}(s) = a_m/\tau_m$: forward-back drivability, respectively. In addition, $G_{fb}(s)$ and $G_f(s)$ are the transfer functions related to the command response, and $G_{bf}(s)$ and $G_b(s)$ are the transfer functions related to the human interaction. Here, ideal drivability is defined as the control goal following to:

$$\begin{bmatrix} a_l \\ a_m \end{bmatrix} = \begin{bmatrix} \frac{1}{J_{ln}} & \frac{1}{J_{mn}R_g} \\ \frac{1}{J_{ln}}R_g & \frac{1}{J_{mn}} \end{bmatrix} \begin{bmatrix} \tau_l^{ext} \\ \tau_m \end{bmatrix}, \tag{2.8}$$

where $R_g$, $J_{mn}$ and $J_{ln}$ denote the gear ratio and the nominal values of motor-side inertia and load-side inertia, respectively. In (2.8), $G_{fb}(s)$ and $G_f(s)$ are based on $1/J_{mn}$ because these are characteristics from the motor-side (actuator-side) input to the motor-side or load-side output. In addition, $G_{bf}(s)$ and $G_b(s)$ are based on $1/J_{ln}$ because these are characteristics from the load-side input to the motor-side or load-side output. This paper considers human interaction, as shown in Fig.2.5, and uses the

external force as an input. This concept assumes the direct teaching operation, cooperative operation with human, etc. When evaluating the human-interaction system modeled as two-inertia system, the motion of the robot is easy to understand by evaluating the load-side information, intuitively. This chapter focuses on improving the back-forward drivability for human interaction. For human interaction, it is desirable for the frequency characteristics of back-forward drivability to remain constant without a vibration effect within the entire frequency range. Therefore, the ideal back-forward drivability for human-robot interactions is defined as shown in $G_{bf}(s)$ of (2.8), i.e., $G_{bf}(s) = 1/J_{ln}$. This means that single inertialization of two-inertia system.

### 2.3.2 Disturbance Observer in Two-Inertia System

Actual external torque feedback control is generally used for improving the back-forward drivability. In particular, force control based on acceleration control is well known to be a general robust force control system, where a DOB is used [85–89]. This section analyzes the two-inertia system employing a DOB and back-forward drivable control based on load-side torque control.

First, Fig.2.6 shows a block diagram of the two-inertia system employing a DOB, where $J_l$, $K_s$, $R_g$ denote load-side inertia, torsion spring constant, gear ratio, respectively. The disturbance torque in two-inertia system is defined as

$$\tau_m^{dis} = \frac{\tau_s}{R_g} + \tau_{dm} = \frac{\tau_s}{R_g} + \tau_{fm} + \Delta J_m s\omega_m - \Delta K_t i_q, \tag{2.9}$$

where $\tau_s$ is the torsion torque. For simplicity, this study only considers the viscous friction. The back-forward drivability of Fig.2.6 is derived as

$$G_{bf}^{DOB}(s) = \frac{a_l}{\tau_l^{ext}} = -s\frac{1}{J_l}\frac{s^2 + \left(g_{dm} + \frac{D_m}{J_m}\right)s + \frac{K_s}{J_m R_g^2}}{D_{en}^{DOB}(s)} \tag{2.10}$$

$$D_{en}^{DOB}(s) = s^3 + \left(g_{dm} + \frac{D_m}{J_m}\right)s^2 + K_s\left(\frac{1}{J_m R_g^2} + \frac{1}{J_l}\right)s + \frac{K_s}{J_l}\left(g_{dm} + \frac{D_m}{J_m}\right). \tag{2.11}$$

Fig.2.7 shows the Bode diagram of two-inertia system-controlled DOB. As shown in (2.10) and Fig.2.7, $G_{bf}^{DOB}(s)$ does not have a steady-state term. The concept motion is not achieved in $G_{bf}^{DOB}(s)$

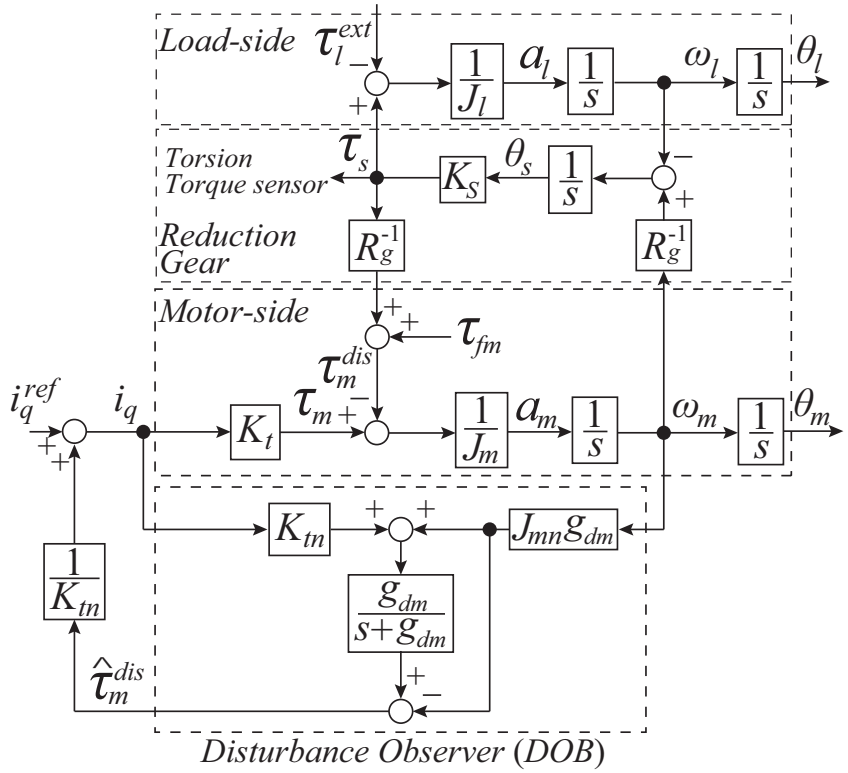


Figure2.6: Block diagram of two-inertia system applied DOB.

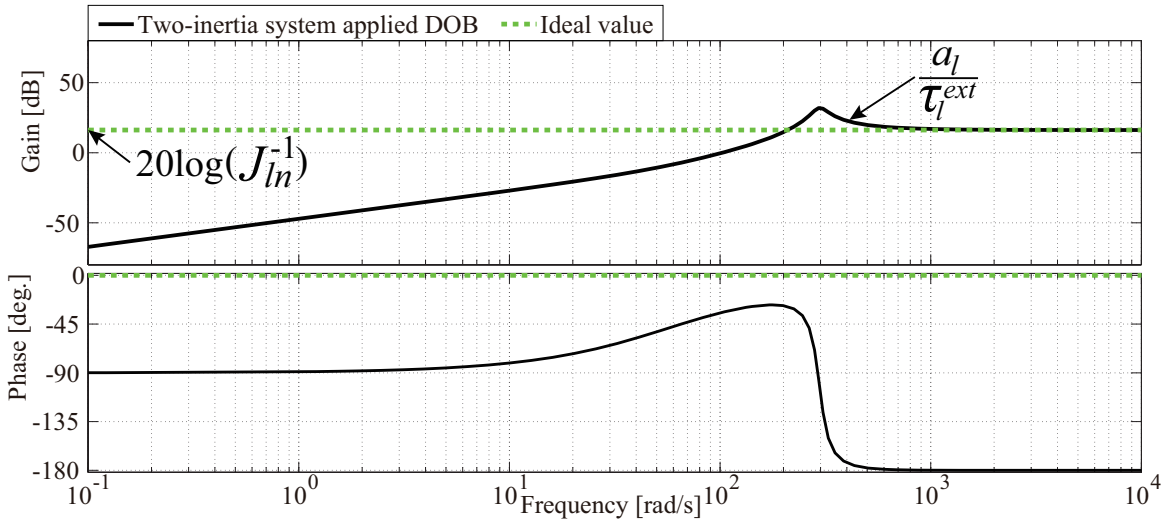


Figure2.7: Bode diagram of back-forward drivability in two-inertia system controlled DOB. Black and green lines are two-inertia system applied DOB and ideal value such as $20\log(1/J_{ln})$.

because the DOB compensates the disturbance, including the external torque. Therefore, the back-forward drivability is decreased when using the DOB-based control system for a two-inertia system. However, forward-back drivability is improved by DOB. Therefore, the back-forward drivable control based on load-side torque control (LTC) improves the back-forward drivability feeding back the external torque to the acceleration reference.

### 2.3.3 Load-side Torque Observer

This section explains a load-side torque observer (LTOB) for estimation of the external torque in conventional back-forward drivable control system. The state equations of the plant system is expressed as

$$\dot{x}_l = A_l x_l + B_l u_l \tag{2.12}$$

$$y_l = C_l x_l \tag{2.13}$$

$$x_l = \begin{bmatrix} \tau_s & \omega_l & \tau_l^{ext} \end{bmatrix}^T \tag{2.14}$$

$$u_l = \omega_m,\ y_l = \tau_s \tag{2.15}$$

$$A_l = \begin{bmatrix} 0 & -K_s & 0 \\ J_l^{-1} & 0 & -J_l^{-1} \\ 0 & 0 & 0 \end{bmatrix} \tag{2.16}$$

$$B_l = \begin{bmatrix} K_s R_g^{-1} & 0 & 0 \end{bmatrix}^T \tag{2.17}$$

$$C_l = \begin{bmatrix} 1 & 0 & 0 \end{bmatrix}. \tag{2.18}$$

In (2.12)–(2.18), the input vector and output vector are $u_l = \omega_m$ and $y_l = \tau_s$. From (2.12)–(2.18), the state equation of the external torque estimation is expressed as

$$\dot{\hat{x}}_l = A_{dl}\hat{x}_l + B_{dl}u_{dl} \tag{2.19}$$

$$y_{dl} = C_{dl}\hat{x}_l \tag{2.20}$$

$$\hat{x}_l = \begin{bmatrix} \hat{\tau}_s & \hat{\omega}_l & \hat{\tau}_l^{ext} \end{bmatrix}^T \tag{2.21}$$

$$u_{dl} = [\omega_m \ \tau_s]^T, \ y_{dl} = \hat{\tau}_l^{ext} \tag{2.22}$$

$$A_{dl} = \begin{bmatrix} -(l_1+l_2+l_3) & -K_{sn} & 0 \\ \frac{l_1l_2+l_2l_3+l_3l_1}{K_{sn}} & 0 & -J_{ln}^{-1} \\ -\frac{J_{ln}l_1l_2l_3}{K_{sn}} & 0 & 0 \end{bmatrix} \tag{2.23}$$

$$B_{dl} = \begin{bmatrix} K_{sn}R_g^{-1} & l_1+l_2+l_3 \\ 0 & \frac{1}{J_{ln}} - \frac{l_1l_2+l_2l_3+l_3l_1}{K_{sn}} \\ 0 & \frac{J_{ln}l_1l_2l_3}{K_{sn}} \end{bmatrix} \tag{2.24}$$

$$C_{dl} = \begin{bmatrix} 0 & 0 & 1 \end{bmatrix} \tag{2.25}$$

where $l_1$, $l_2$, and $l_3$ denote the observer poles. Observer poles are determined as $(s+l_1)(s+l_2)(s+l_3) = 0$. In this paper, observer poles are designed as $l_1 = l_2 = l_3 = g_{dl}$, where $g_{dl}$ denotes the bandwidth of the LTOB. The LTOB is able to estimate the external torque using (2.19)–(2.25).

### 2.3.4 Back-Forward Drivable Control Based on Load-side Torque Control using Motor-side Acceleration Control

Fig.2.8 shows a block diagram of back-forward drivable control based on an LTC using motor-side acceleration control. This system comprises a DOB-based motor-side acceleration control, load-side torque observer for detecting external torque, and a load-side torque controller. From Fig.2.8, the back-forward drivability is derived as

$$\begin{aligned} G_{bf}^{LTC}(s) = \frac{a_l}{\tau_l^{ext}} = -\frac{1}{(s+g_{dl})^3}\Big[\frac{K_s}{J_l}C_t g_{dl}^3(s+g_{dm}) \\ + \frac{1}{J_l}s\Big\{s^2 + \Big(g_{dm} + \frac{D_m}{J_m}\Big)s + \frac{K_s}{J_m R_g^2}\Big\}(s+g_{dl})^3\Big]\frac{1}{D_{en}^{DOB}(s)} \end{aligned} \tag{2.26}$$

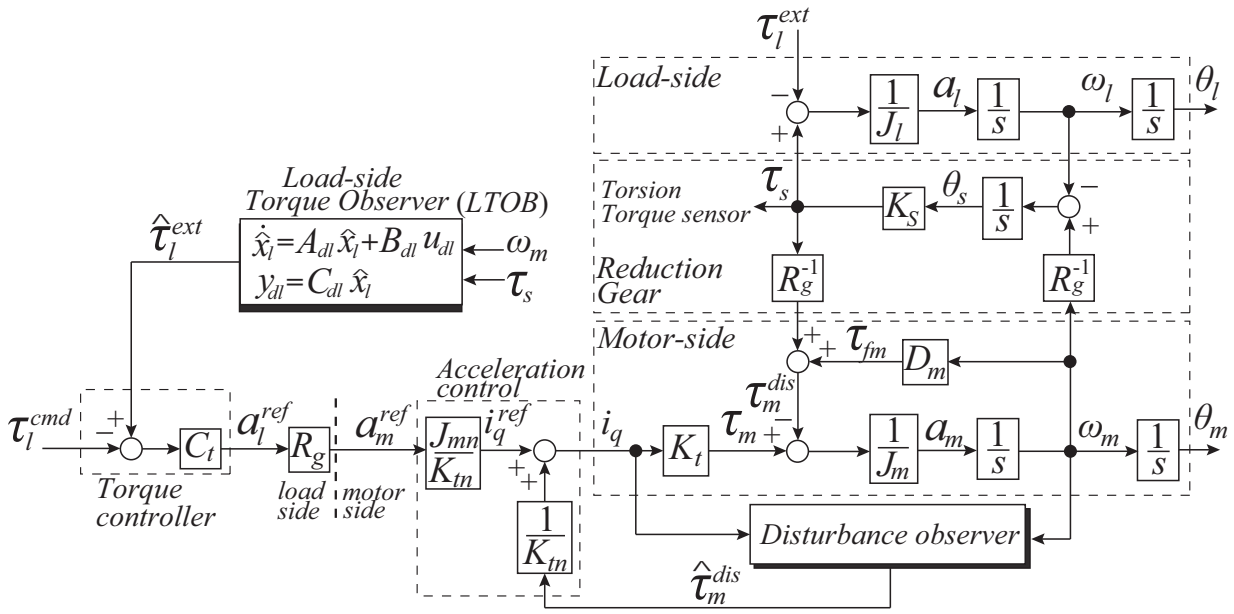


Figure2.8: Block diagram of back-forward drivable control based on load-side torque control.

in which, assuming $g_{dm}$ as ideal, (2.26) is able to be expressed as

$$\begin{aligned}\lim_{g_{dm}\to\infty} G_{bf}^{LTC}(s) &= \lim_{g_{dm}\to\infty} \frac{a_l}{\tau_l^{ext}} \\ &= -\frac{\frac{K_s}{J_l}C_t g_{dl}^3 + \frac{1}{J_l}s^2(s+g_{dl})^3}{(s^2+\frac{K_s}{J_l})(s+g_{dl})^3} \\ &= -\frac{1}{J_l}\Big[1 - \left\{\omega_a^2 s^3 + 3d_{dl}\omega_a^2 s^2 + 3g_{dl}^2\omega_a^2 s + g_{dl}^3(\omega_a^2 - K_s C_t)\right\}\frac{1}{\left(s^2+\frac{K_s}{J_l}\right)(s+g_{dl})^3}\Big]\end{aligned} \tag{2.27}$$

where, anti-resonant frequency and torque gain are assumed as $\omega_a = \sqrt{K_s/J_l}$, $C_t = 1/J_{ln}$, and $J_l = J_{ln}$. Thus, (2.27) is written as

$$\begin{aligned}\lim_{g_{dm}\to\infty} G_{bf}^{LTC}(s) &= \lim_{g_{dm}\to\infty} \frac{a_l}{\tau_l^{ext}} \\ &= -\frac{1}{J_l}\Big\{1 - \frac{\omega_a^2}{s^2+\omega_a^2}\frac{s(s^2+3g_{dl}s+3g_{dl}^2)}{(s+g_{dl})^3}\Big\} \\ &= -\frac{1}{J_l} + \frac{1}{J_l}\frac{\omega_a^2}{s^2+\omega_a^2}\frac{s(s^2+3g_{dl}s+3g_{dl}^2)}{(s+g_{dl})^3}.\end{aligned} \tag{2.28}$$

From (2.28), the back-forward drivability has a steady-state term in the first term and has a vibration term of a sinusoidal wave in the second term. Figs. 2.9 and 2.10 show the back-forward drivable

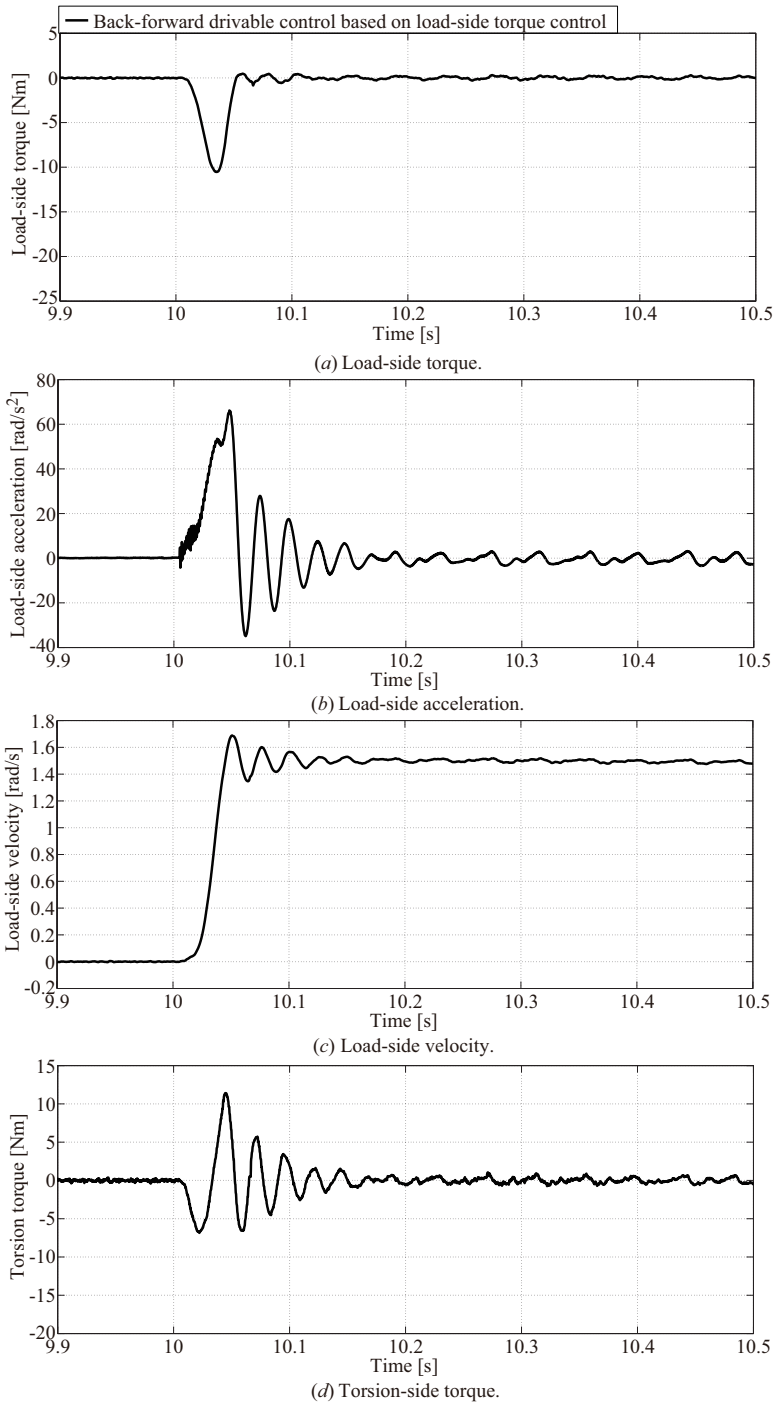


Figure2.9: Experimental results of back-forward drivable response in Fig.2.8. (a) Load-side torque. (b) Load-side acceleration. (c) Load-side velocity. (d) Torsion torque.

response and a Bode diagram of the back-forward drivable control based on a LTC. As shown in Fig.2.9, the back-forward drivability is improved by external torque feedback and the concept of

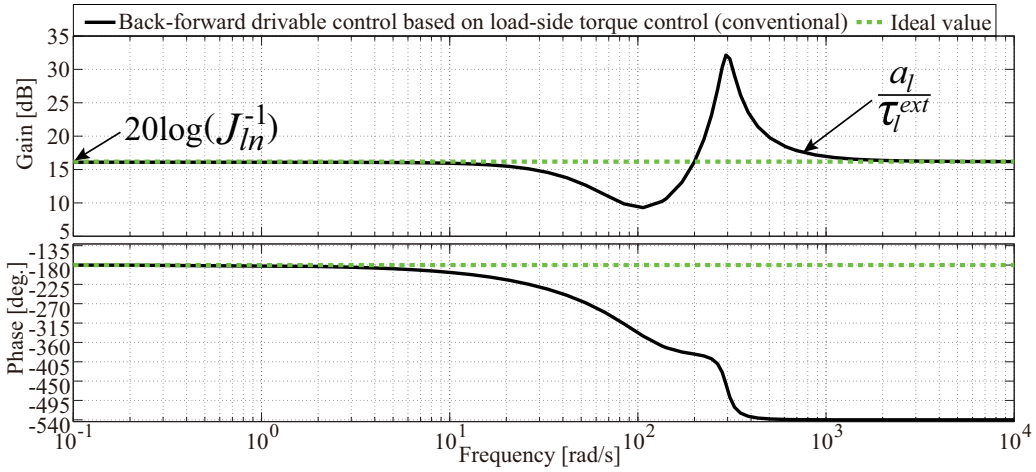


Figure2.10: Bode diagram of back-forward drivable control based on LTC. Black and green lines are conventional back-forward drivable control based on load-side torque control and ideal value such as $20\log(1/J_{ln})$.

Fig.2.5 is achieved. However, the vibration occurs due to influence of resonant frequency $\omega_a$ (see (2.28)). Moreover, when the bandwidth of the DOB is ideal, the acceleration with regard to the load-side acceleration is expressed as

$$\begin{aligned}\mathcal{L}^{-1}\Big\{a_l(s)\Big\} &= \mathcal{L}^{-1}\Big\{\frac{\frac{K_s}{J_l}}{s^2+\frac{K_s}{J_l}}a_l^{ref}(s)\Big\}\\ &= \omega_a\mathcal{L}^{-1}\Big\{\frac{\omega_a}{s^2+\omega_a^2}\Big\}a_l^{ref}(t)\\ &= \omega_a\sin\omega_a t\cdot a_l^{ref}(t),\end{aligned} \tag{2.29}$$

where $a_l^{ref}(t) = \delta(t)$. Here, (2.29) indicates that the DOB-based back-forward drivable control method has the effect of amplifying a load-side vibration because the DOB cancels out the passing from the load-side to the motor-side. Therefore, the back-forward drivable control based on the LTC is able to achieve the target value of back-forward drivability under a steady state, i.e., $G_{bf}(s) = 1/J_{ln}$. However, the target value of back-forward drivability is not achieved during a transient state. Influence of vibration is reduced using velocity feedback and virtual impedance controller [88], but back-forward drivability in the definition is not able to be realized. This is because the velocity feedback gain deteriorate the back derivability. Thus, it is necessary to achieve the vibration suppression

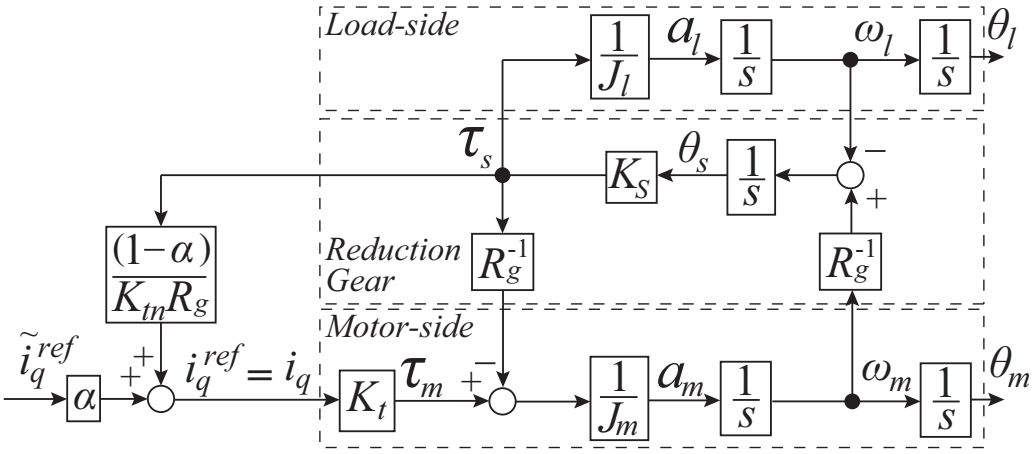


Figure2.11: Block diagram of RRC of two-inertia system (conventional).

while maintaining the back-forward drivability, i.e, $G_{bf}(s) = 1/J_{ln}$.

## 2.4 Force Control Considering Environmental Dynamics for Environment Interaction

To interact the environmental object, not only considering the environmental dynamics, but also enhancing force control performance are required. In general, manipulator is modeled as two-inertia system; thus, it is necessary to apply the vibration suppression control. For vibration suppression, full state feedback, resonance ratio control (RRC), two DoF control, etc, have been proposed. Especially, the RRC proposed by Yuki *et al.* [72] is well-known as simple and effective vibration suppression control [73, 74]. In this section, conventional force control based on RRC [40] is discussed.

### 2.4.1 RRC without Environment

This section initially describes the RRC that does not consider interaction with the environment, and discusses the conventional load-side torque control based on the RRC. The RRC shown in Fig.2.11 is mainly utilized for velocity and position controls. The transfer function of Fig.2.11 is expressed as

follows:

$$\frac{\omega_m}{\widetilde{i}_q^{ref}} = \frac{\frac{K_t}{J_m}\alpha\left(s^2 + \frac{K_s}{J_l}\right)}{s\left\{s^2 + K_s\left(\frac{\alpha}{J_m R_g^2} + \frac{1}{J_l}\right)\right\}} = \frac{\frac{K_t}{J_m}\alpha\left(s^2 + \omega_a^2\right)}{s(s^2 + (\omega_r^{RRC})^2)} \tag{2.30}$$

$$\omega_r^{RRC} = \sqrt{\frac{K_s\alpha}{J_m R_g^2} + \frac{K_s}{J_l}} = \sqrt{\frac{K_s}{J_m^{'} R_g^2} + \frac{K_s}{J_l}} \tag{2.31}$$

$$\omega_a = \sqrt{\frac{K_s}{J_l}}\ ,\ J_m^{'} = J_m/\alpha, \tag{2.32}$$

where $\omega_a$ and $\omega_r^{RRC}$ denote the anti-resonant and the resonant frequencies of RRC without environment, respectively; and $J_m^{'}$ is the controlled motor-side inertia by RRC without environment. The resonant frequency $\omega_r^{RRC}$ in (2.31) is regulated by the resonance ratio gain $\alpha$. Therefore, the resonance ratio $H_r$ is easily determined from $H_r = \omega_r^{RRC}/\omega_a$.

### 2.4.2 Load-side Torque Control Based on RRC (Conventional)

To achieve the force control, the two-inertia system including the environmental dynamics are first considered. The RRC with the environment is shown in Fig.2.12, wherein, the conventional load-side torque control is utilized, as shown in Fig.2.13, using the torsion torque and acceleration sensors. In this study, the load-side torque control is evaluated by measuring the torsion torque and load-side acceleration sensors. The external torque $\tau_l^{ext}$ is calculated using torsion torque and acceleration sensors, i.e., $\tau_l^{ext} = \tau_s - J_{ln}a_l$. Furthermore, as the bandwidth of acceleration and torsion torque sensors is 1.0 kHz, the sensor dynamics are neglected. The closed-loop transfer function $G_\tau^{cl,Conv.}(s)$

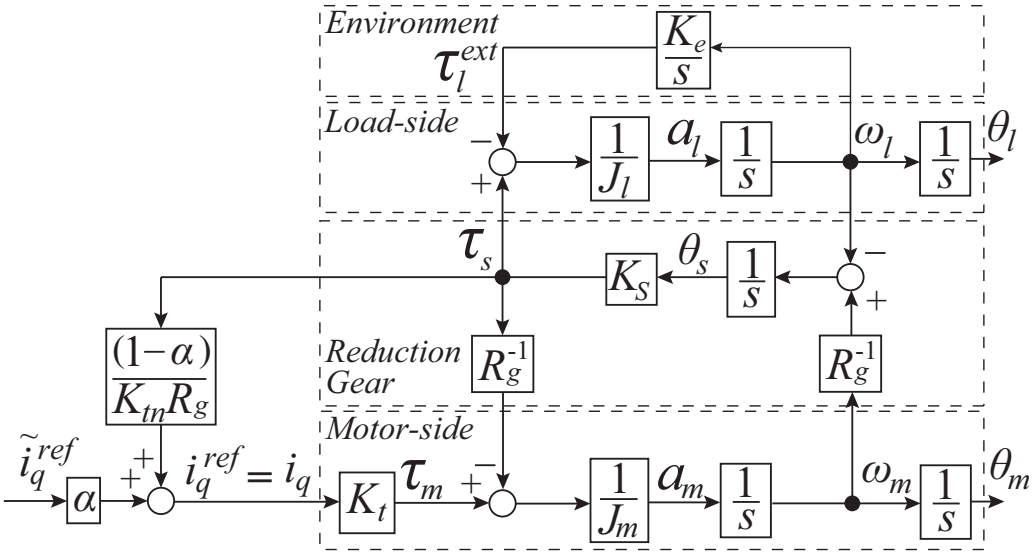


Figure2.12: Block diagram of RRC in two-inertia system with environment (conventional).

from the load-side torque command $\tau_l^{cmd}$ to the external torque $\tau_l^{ext}$ is derived as

$$G_\tau^{cl,Conv.}(s) = \frac{\tau_l^{ext}}{\tau_l^{cmd}} = \frac{\frac{\omega_{ae}^2 K_s K_t K_{if}\alpha}{J_m R_g}}{D_{en}^{cl,Conv.}(s)} \tag{2.33}$$

$$\begin{aligned} D_{en}^{cl,Conv.}(s) &= s^5 + \frac{K_t K_{vf}\alpha}{J_m}s^4 + \left(\omega_{ar}^2 + \frac{K_s\alpha}{J_m R_g^2}\right)s^3 \\ &\quad + \omega_{ar}^2\frac{K_t K_{vf}\alpha}{J_m}s^2 + \omega_{ae}^2\frac{K_s\alpha(K_t K_{pf} + R_g^{-1})}{J_m R_g}s + \omega_{ae}^2\frac{K_s K_t K_{if}\alpha}{J_m R_g} \end{aligned} \tag{2.34}$$

$$= s^5 + a_4^{cl,Conv.}s^4 + a_3^{cl,Conv.}s^3 + a_2^{cl,Conv.}s^2 + a_1^{cl,Conv.}s + a_0^{cl,Conv.} \tag{2.35}$$

$$\omega_{ar} = \sqrt{\frac{K_e + K_s}{J_l}} \tag{2.36}$$

$$\omega_{ae} = \sqrt{\frac{K_e}{J_l}}. \tag{2.37}$$

Here, the control gains are designed using the stability indices as utilized in [90, 91]. The stability indices $\gamma_i$ and an equivalent time constant $\tau_c$ are defined as $\gamma_i = (a_i^{cl,Conv.})^2/(a_{i-1}^{cl,Conv.}a_{i+1}^{cl,Conv.})$ and $\tau_c = a_1^{cl,Conv.}/a_0^{cl,Conv.}$, respectively. Compared with the stability indices, (2.34), and (2.35), the control gains in case of binomial design [91] are given by

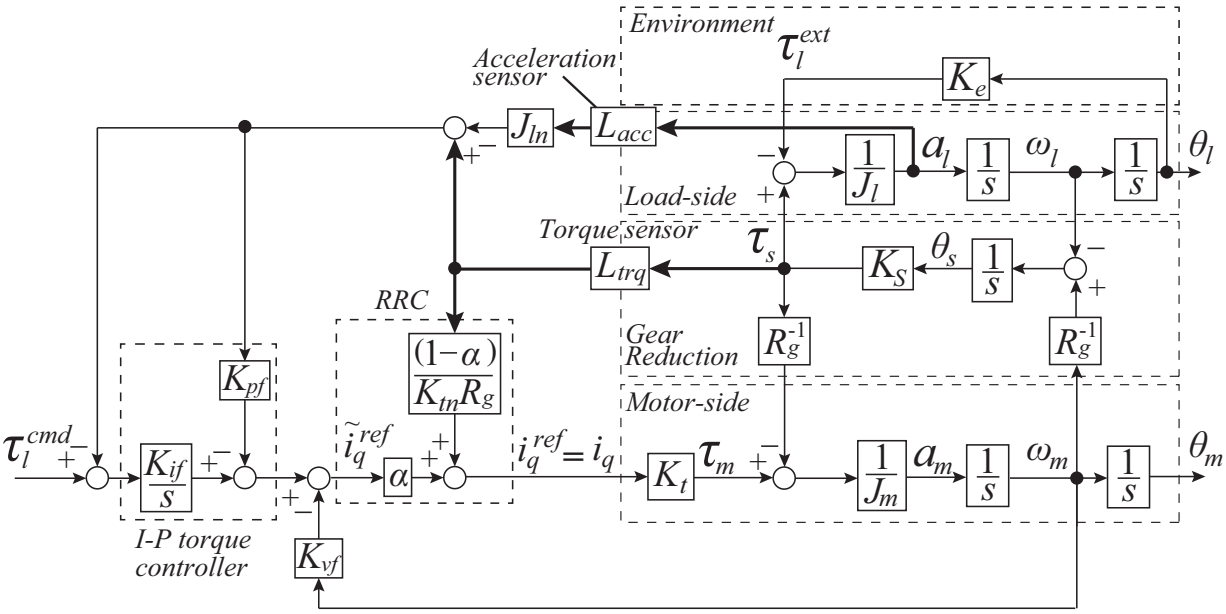


Figure2.13: Block diagram of load-side torque control based on RRC (conventional).

$$\alpha = \frac{J_{mn}R_g^2}{K_{sn}}(\gamma_3\gamma_4 - 1)\omega_{ar}^2 = \frac{4J_{mn}R_g^2}{K_{sn}}\omega_{ar}^2 \tag{2.38}$$

$$K_{vf} = \frac{J_{mn}}{\alpha K_{tn}}\sqrt{\gamma_3}\gamma_4\omega_{ar} = \frac{5}{2}\sqrt{2}\frac{J_{mn}}{\alpha K_{tn}}\omega_{ar} \tag{2.39}$$

$$\begin{aligned} K_{pf} &= \frac{1}{K_{tn}}\left(\frac{J_{mn}R_g}{K_{sn}}\frac{1}{\alpha}\frac{\gamma_4}{\gamma_2}\frac{\omega_{ar}^4}{\omega_{ae}^2} - \frac{1}{R_g}\right) \\ &= \frac{1}{K_{tn}}\left(\frac{5}{2}\frac{J_{mn}R_g}{K_{sn}}\frac{1}{\alpha}\frac{\omega_{ar}^4}{\omega_{ae}^2} - \frac{1}{R_g}\right) \end{aligned} \tag{2.40}$$

$$K_{if} = \frac{J_{mn}R_g}{K_{sn}K_{tn}}\frac{1}{\alpha}\frac{\gamma_4}{\gamma_1\gamma_2^2\sqrt{\gamma_3}}\frac{\omega_{ar}^5}{\omega_{ae}^2} = \frac{J_{mn}R_g}{K_{sn}K_{tn}}\frac{1}{4\sqrt{2}\alpha}\frac{\omega_{ar}^5}{\omega_{ae}^2}, \tag{2.41}$$

where, the stability indices are following values: $\gamma_1 = \gamma_4 = 2.5$ and $\gamma_2 = \gamma_3 = 2.0$. These stability indices are determined based on binomial design indicated in [91]. Then, the equivalent time constant is calculated as

$$\tau_c = \gamma_1\gamma_2\sqrt{\gamma_3}\frac{1}{\omega_{ar}} = \frac{5\sqrt{2}}{\omega_{ar}}. \tag{2.42}$$

### 2.4.3 Problem Formulation in RRC with Environment

This section evaluates the resonance ratio in the RRC with the environment. In the RRC with environment, the transfer function from the motor current $\widetilde{i}_q^{ref}$ to motor-side velocity $\omega_m$ is derived from Fig.2.12 as follows:

$$\begin{aligned}\frac{\omega_m}{\widetilde{i}_q^{ref}} &= \frac{\frac{K_t}{J_m'}s\Big(s^2+\omega_{ar}^2\Big)}{s^4+d_2s^2+d_0} \\ &= \frac{\frac{K_t}{J_m'}s\Big(s^2+\omega_{ar}^2\Big)}{(s^2+(\omega_{r1}^{RRC})^2)(s^2+(\omega_{r2}^{RRC})^2)} \qquad (2.43)\\ d_2 &= \frac{K_e+K_s}{J_l}+\frac{K_s}{J_m'R_g^2}\ ,\ d_0=\frac{K_sK_e}{J_m'J_lR_g^2} \qquad (2.44)\\ \omega_{r1}^{RRC} &= \sqrt{\frac{1}{2}\Big(d_2-\sqrt{d_2^2-4d_0}\Big)} \qquad (2.45)\\ \omega_{r2}^{RRC} &= \sqrt{\frac{1}{2}\Big(d_2+\sqrt{d_2^2-4d_0}\Big)} \qquad (2.46)\\ J_m^{'} &= J_m/\alpha. \qquad (2.47)\end{aligned}$$

In (2.43)–(2.47), the motor-side inertia is able to be controlled by the resonance ratio gain $\alpha$, but the two-inertia system with the environment has two resonant frequencies $\omega_{r1}^{RRC}$ and $\omega_{r2}^{RRC}$; therefore, it is necessary to consider the two resonant frequencies (2.45) and (2.46) for force control design. In addition, it is difficult to determine the optimal resonance ratio $H_r$ considering two resonant frequencies. This study considers the method suggested in [40] to evaluate the resonance ratio between $\omega_{r2}^{RRC}$ and $\omega_{ar}$ for the conventional method. Thus, the resonance ratio is calculated by inserting (2.38) to (2.46), as follows:

$$\begin{aligned}H_r &= \frac{\omega_{r2}^{RRC}}{\omega_{ar}} = \sqrt{\frac{1}{2}\Big(d_2+\sqrt{d_2^2-4d_0}\Big)}\Big/\omega_{ar} \\ &= \sqrt{\frac{\gamma_3\gamma_4}{2}+\sqrt{\Big(\frac{\gamma_3\gamma_4}{2}\Big)^2-\frac{K_e(\gamma_3\gamma_4-1)}{K_e+K_s}}}. \qquad (2.48)\end{aligned}$$

(2.48) show that the resonance ratio considering the environment depends on the torsion stiffness $K_s$ and environmental stiffness $K_e$. Therefore, the load-side torque control based on the RRC considering the environment cannot uniquely determine the optimal resonance ratio.

To realize the stable force control, it is necessary to evaluate their robustness against the environmental stiffness variation (i.e., $K_e$ variation). This section evaluates the gain and phase margins for the conventional load-side torque control based on RRC under the $K_e$ variation. Moreover, robust stability analysis is conducted.

### 2.4.4 Back-Forward Drivability of Conventional Load-side Torque Control Based on RRC

To confirm the high-performance force control or not, back-forward drivability is evaluated. If there is back-forward drivability on acceleration dimension, the load-side torque control system is high-performance. According to Section 2.3.1, back-forward drivability on acceleration dimension should be satisfied. Back-forward drivability of Fig.2.13 is derived as

$$G_{bf}^{Conv.}(s) = \frac{a_l}{\tau_l^{ext}} = -\frac{1}{J_l}\frac{s^3 + \frac{K_tK_{vf}\alpha}{J_m}s^2 + \left(\frac{K_s\alpha}{J_mR_g^2} + \frac{K_sK_tK_{pf}\alpha}{J_mR_g}\right)s + \frac{K_sK_tK_{if}\alpha}{J_mR_g}}{s^3 + \frac{K_tK_{vf}}{J_m}s^2 + \left(\frac{K_s}{J_l} + \frac{K_s\alpha}{J_mR_g^2}\right)s + \frac{K_sK_tK_{vf}\alpha}{J_mJ_l}} \tag{2.49}$$

$$= -\frac{1}{J_l}\left\{1 - \frac{\frac{K_tK_{vf}(1-\alpha)}{J_m}s^2 + (\frac{K_s}{J_l} - \frac{K_sK_tK_{pf}\alpha}{J_mR_g})s + \frac{K_sK_t\alpha}{J_m}(\frac{K_{vf}}{J_l} - \frac{K_{if}}{R_g})}{s^3 + \frac{K_tK_{vf}}{J_m}s^2 + \left(\frac{K_s}{J_l} + \frac{K_s\alpha}{J_mR_g^2}\right)s + \frac{K_sK_tK_{vf}\alpha}{J_mJ_l}}\right\}. \tag{2.50}$$

Here, back-forward drivability in steady state is calculated as

$$\lim_{s\to 0} sG_{bf}^{Conv.}(s)\frac{1}{s} = -\frac{1}{J_l}\frac{1}{\gamma_1\gamma_2^2\gamma_3}\frac{(K_e+K_s)^2}{K_eK_s}. \tag{2.51}$$

From (2.51), back-forward drivability of conventional load-side torque control based on RRC depends on $K_e$ and $K_s$. Therefore, in the case of the conventional load-side torque control based on RRC, it is necessary to adjust the back-forward drivability according to environmental dynamics. From (2.50), bode diagram of back-forward drivability in conventional load-side torque control is shown in Fig.2.14.

In Fig.2.14, back-forward drivability has constant value at low-frequency region and back-forward drivability on acceleration dimension is realized. Therefore, Fig.2.14 show that conventional load-side torque control based on RRC is high-performance force control system. However, the $K_e$ variations

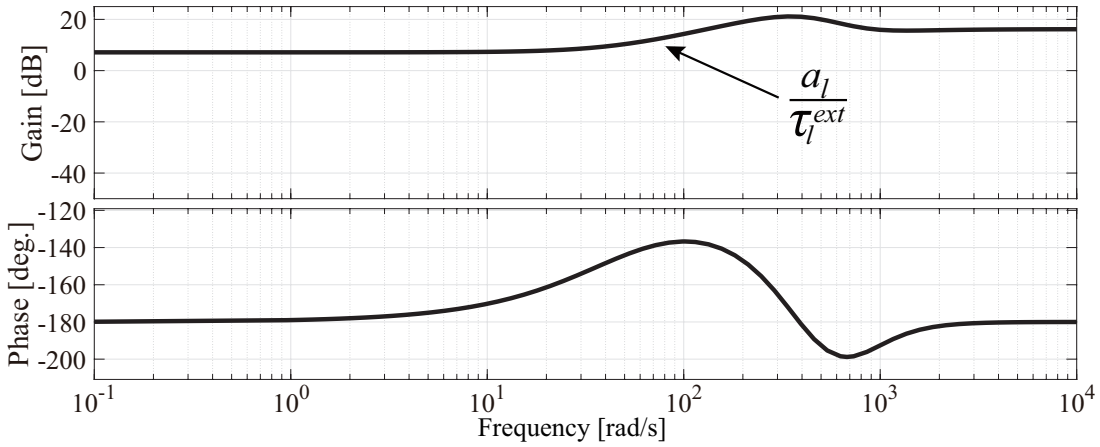


Figure2.14: Bode diagram of back-forward drivability $a_l/\tau_l^{ext}$ in conventional load-side torque control based on RRC.

have not verified in this system. For environment interaction, it is necessary to satisfy the robustness against the $K_e$ variation. Next, the robust stability against the environmental stiffness variation is considered.

### 2.4.5 Gain and Phase Margins for Conventional Load-side Torque Control Based on RRC

Gain and phase margins [92] are evaluated against the open-loop characteristics of the whole system shown in Fig.2.13. In the conventional method shown in Fig.2.13, the open-loop transfer function $G_\tau^{op,Conv.}(s) = \tau_l^{ext}/\tau_l^{cmd}$ from the load-side torque command $\tau_l^{cmd}$ to the external torque $\tau_l^{ext}$ is derived as

$$G_\tau^{op,Conv.}(s) = \frac{\tau_l^{ext}}{\tau_l^{cmd}} = n_0^{op,Conv.} \Big/ \Big( s^5 + \sum_{i=1}^{4} d_i^{op,Conv.} s^i \Big) \tag{2.52}$$

$$d_1^{op,Conv.} = \omega_{ae}^2 \Big( \frac{\alpha K_s}{J_m R_g^2} + \frac{\alpha K_s K_t K_{pf}}{J_m R_g} \Big) \tag{2.53}$$

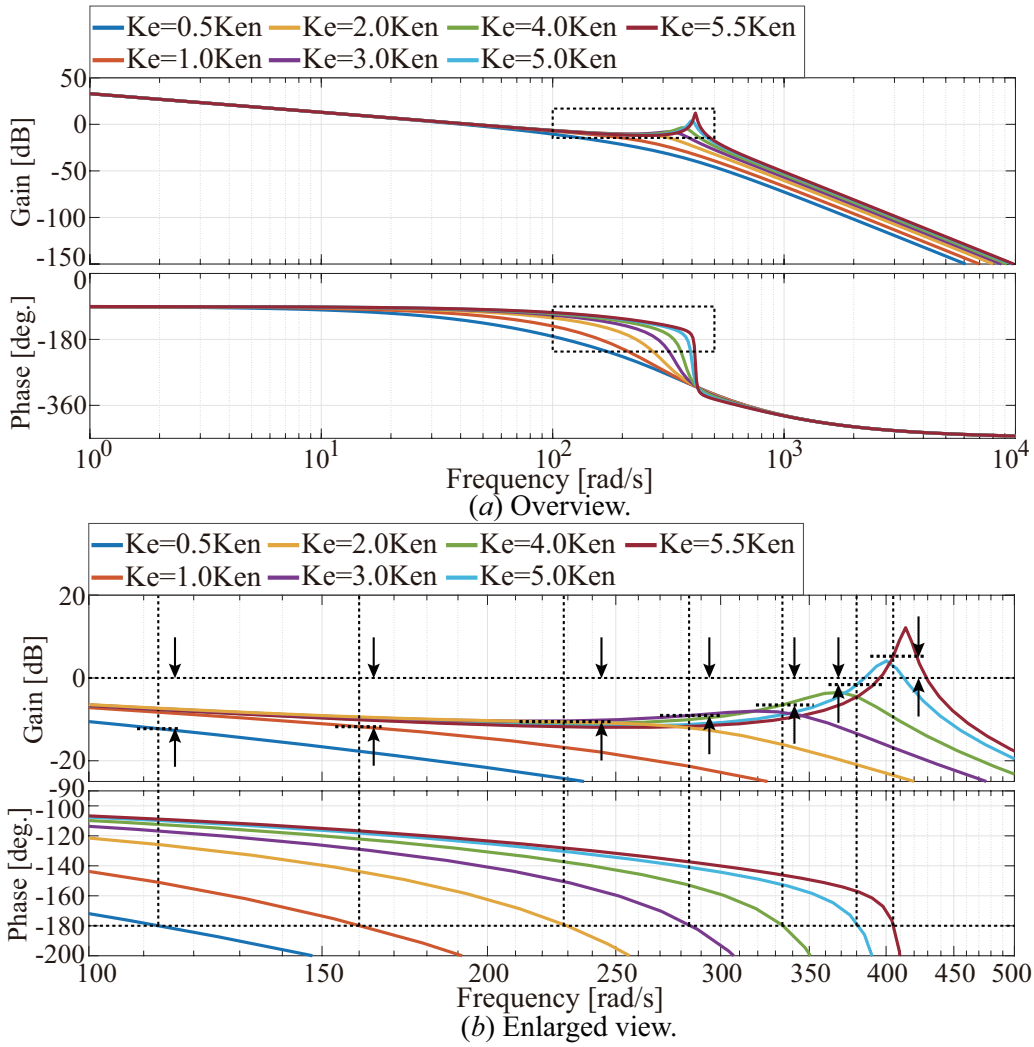


Figure2.15: Bode diagram of open-loop transfer function in conventional method. (a) Overview. (b) Enlarged view.

$$d_2^{op,Conv.} = \omega_{ar}^2 \frac{\alpha K_t K_{vf}}{J_m} \tag{2.54}$$

$$d_3^{op,Conv.} = \omega_{ar}^2 + \frac{\alpha K_s}{J_m R_g^2} \tag{2.55}$$

$$d_4^{op,Conv.} = \frac{\alpha K_t K_{vf}}{J_m} \tag{2.56}$$

$$n_0^{op,Conv.} = \omega_{ae}^2 \frac{\alpha K_s K_t K_{if}}{J_m R_g}. \tag{2.57}$$

The Bode diagram of (2.52) is shown in Fig.2.15 and Table2.1 lists the gain and phase margins of the conventional method. This section observes that the gain margin decreases when $K_e$ increases

Table2.1: Gain and phase margins of conventional load-side torque control based on RRC.

| $K_e$ | Gain margin, dB | Phase margin, deg. |
|---|---|---|
| $0.5K_{en}$ | 12.249 | 52.796 |
| $1.0K_{en}$ | 11.789 | 66.937 |
| $2.0K_{en}$ | 10.647 | 76.301 |
| $3.0K_{en}$ | 9.032 | 79.585 |
| $4.0K_{en}$ | 6.469 | 81.227 |
| $5.0K_{en}$ | 1.217 | 82.209 |
| $5.5K_{en}$ | $-5.508$ | 82.565 |

beyond $K_{en}$, until it finally becomes negative at $K_e = 5.5K_{en}$, indicating that there is no gain margin. Therefore, the stability in the conventional method is restricted by the variations in $K_e$.

### 2.4.6 Robust Stability Analysis using Small Gain Theorem in Load-side Torque Control Based on RRC

In addition, to evaluate the system uncertainty [93], the small gain theorem is considered. System uncertainty is considered as $K_e$ variation.

First, Fig.2.16 shows the block diagram of general plant for evaluation of small gain theorem.

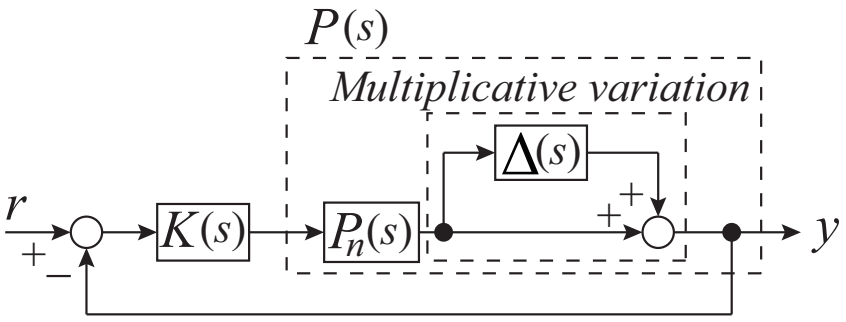


Figure2.16: Block diagram of general plant for evaluation of small gain theorem.

Model error is defined as multiplicative variation $\Delta(s)$. From Fig.2.16, block diagram of small gain theorem is shown in Fig.2.17.

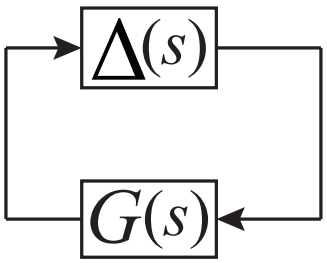


Figure2.17: Block diagram of small gain theorem.

Here, $\Delta(s)$ is defined as

$$\Delta(s) = \frac{P(s) - P_n(s)}{P_n(s)}. \tag{2.58}$$

Moreover, in Fig.2.17, $G(s)$ is expressed as

$$G(s) = \frac{K(s)P_n(s)}{1 + K(s)P_n(s)}. \tag{2.59}$$

(2.59) means the complementary sensitivity function. Here, $G(s)$ is redefined as $T(s)$. Small gain theorem need to satisfy the following equation to:

$$\|\Delta(s)T(s)\|_\infty = \left\|\Delta(s)\frac{K(s)P_n(s)}{1 + K(s)P_n(s)}\right\|_\infty < 1. \tag{2.60}$$

$$|T(s)| < |\Delta(s)^{-1}|. \tag{2.61}$$

Therefore, the robust stability is achieved by satisfying (2.61) in the control system. In this study, to evaluate the robustness against the $K_e$ variation, $T(s)$ and $\Delta(s)^{-1}$ in (2.61) are compared in the control system. In this analysis, general system $G_{\tau n}^{op,Conv.}(s) = \tau_l^{ext}/\tau_l^{cmd}$ of conventional load-side torque control based on RRC is defined, as follows:

$$G_{\tau n}^{op,Conv.}(s) = \frac{\tau_l^{ext}}{\tau_l^{cmd}} = n_{0n}^{op,Conv.} \Big/ \left(s^5 + \sum_{i=1}^{4} d_{in}^{op,Conv.} s^i\right). \tag{2.62}$$

(2.62) is expressed at all nominal values. Therefore, the multiplicative variation $\Delta^{conv.}(s)$ and complementary sensitivity function $T^{conv.}(s)$ in conventional method are calculated as

$$\Delta^{Conv.}(s) = \frac{G_{\tau}^{op,Conv.}(s) - G_{\tau n}^{op,Conv.}(s)}{G_{\tau n}^{op,Conv.}(s)} \tag{2.63}$$

$$T^{Conv.}(s) = \frac{G_{\tau n}^{op,Conv.}(s)}{1 + G_{\tau n}^{op,Conv.}(s)}, \tag{2.64}$$

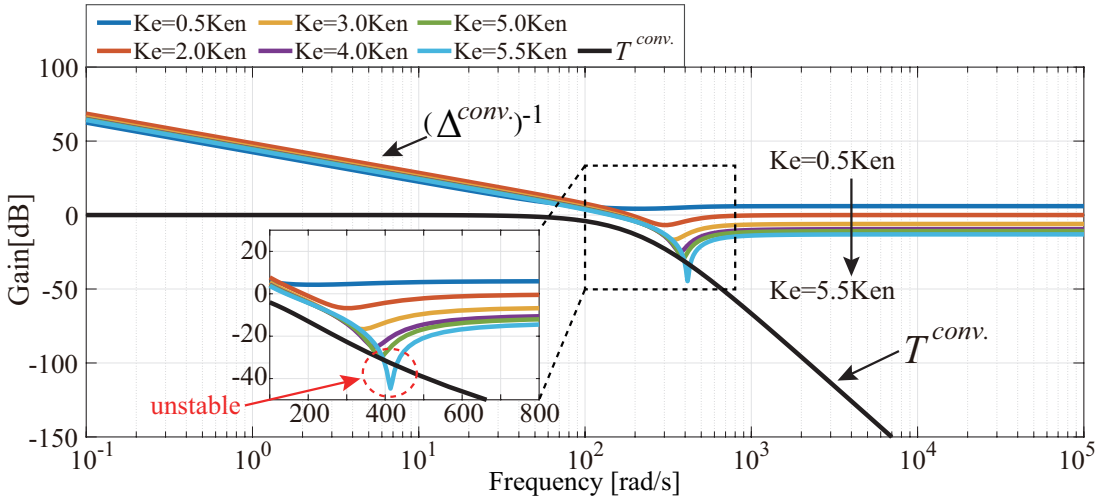


Figure2.18: Bode diagram in terms of $T^{Conv.}(s)$ and $(\Delta^{Conv.}(s))^{-1}$ in conventional method on $K_e$ variation.

where $G_\tau^{op,Conv.}(s)$ is open-loop transfer function of conventional load-side torque control in case of $K_e \neq K_{en}$. From (2.64), Fig.2.18 shows bode diagram in terms of $T^{Conv.}(s)$ and $(\Delta^{Conv.}(s))^{-1}$ in conventional method on $K_e$ variation. As shown in Fig.2.18, $T^{conv.} > (\Delta^{conv.})^{-1}$ when $K_e = 5.5K_{en}$. Namely, conventional load-side torque control based on RRC in case of $K_e = 5.5K_{en}$ is unstable.

### 2.4.7 Numerical Simulation and Experimental Validations in Case of Nominal Design

Next, this section indicates the numerical simulation and experimental results in terms of conventional load-side torque control based on RRC in case of nominal design. Numerical simulation and experimental parameters are listed in Table2.2. Fig.2.19 shows the numerical simulation and experimental results in terms of conventional load-side torque control based on RRC in case of nominal design. These results are observed to verify that the control system is realized as designed. Compared with Fig.2.19 (a) and Fig.2.19 (b), numerical simulation and experimental results are same response. Moreover, smooth and fast force control responses are realized. This is because back-forward drivability is ensured on acceleration dimension. Thus, this section verified that the conventional load-side torque controls have been achieved as designed.

Table2.2: Numerical simulation and experimental parameters in conventional load-side torque control based on RRC.

| Nominal environmental stiffness | $K_{en}$ | 2592 Nm/rad |
|---|---|---|
| $\mathrm{Anti}-\mathrm{resonant\ frequency}$ | $\omega_{ar}$ | 312.62 rad/s |
| First resonant frequency | $\omega_{r1}$ | 67.50 rad/s |
| Second resonant frequency | $\omega_{r2}$ | 357.96 rad/s |
| Bandwidth of MNC | $g_{dm}$ | 628 rad/s |
| Equivalent time constant of Binomial | $\tau_c$ | $5\sqrt{2}/\omega_{ar}$ |
| Resonance ratio gain of Binomial | $\alpha$ | 11.18 |
| Velocity feedbackgain of Binomial | $K_{vf}$ | 0.029 |
| Torque proportional gain of Binomial | $K_{vf}$ | 0.034 |
| Torque integral gain of Binomial | $K_{if}$ | 3.30 |
| Resonance ratio of Binomial (Eq.(2.48)) | $H_r$ | 2.20 |

Next, numerical simulation against $K_e$ variation is confirmed.

### 2.4.8 Numerical Simulation Validation on $K_e$ Variation.

Fig.2.20 shows the simulation results of stability analysis in conventional load-side torque control based on RRC.

From Fig.2.20 (a), the conventional load-side torque control is observed to be stable at $K_e = 5.0K_{en}$; however, vibration is a bit observed. In contrast, load-side torque control becomes unstable at $K_e = 5.5K_{en}$. Therefore, it is necessary to consider the more stable force control for $K_e$ variation.

## 2.5 Force Control Based on Back-Forward Drivable Torsion Torque Control

From above, external torque feedback is able to improve the back-forward drivabililty and force control performance. However, acceleration-based load-side torque control has vibration and load-

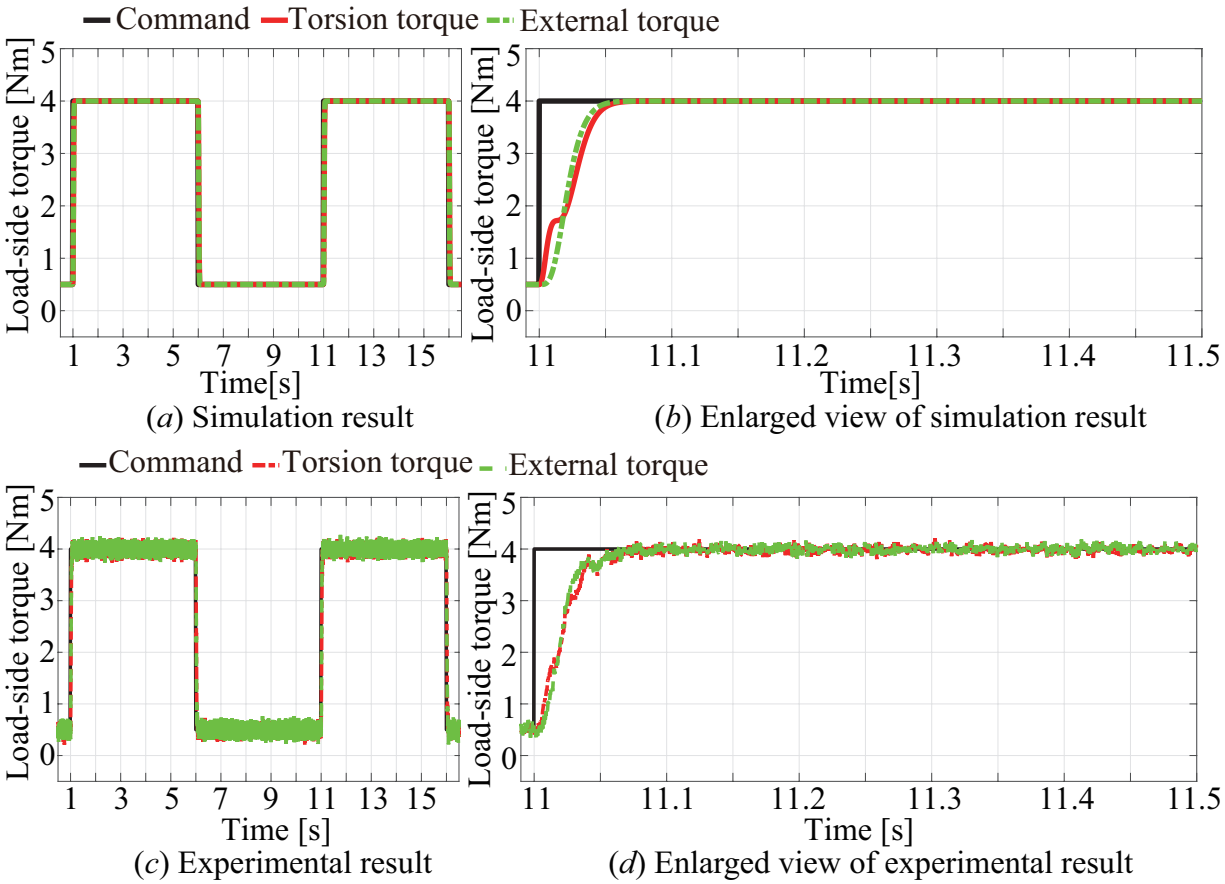


Figure2.19: Numerical simulation and experimental results of load-side torque control based on RRC (conventional). (a) simulation result. (b) Enlarged view of simulation result. (c) Experimental result. (d) Enlarged view of experimental result. Black, red, and green lines are load-side torque command, torsion torque, and external torque, respectively.

side torque control based on RRC has unstable condition on $K_e$ variation. For this, it is necessary to realize vibration suppression while maintaining back-forward drivability. In addition, it is necessary to improve the robustness against the $K_e$ variation in load-side torque control. To overcome these problems, this study focuses on torsion torque control. Torque feedback is able to enhance the back-forward drivability and torsion torque feedback is effective for vibration suppression; thus, back-forward drivable torsion torque control is proposed in this study. Fig.2.21 shows block diagram of two-inertia system using back-forward drivable torsion torque control.

In Fig.2.21, $G_\tau(s)$ and $G_D(s)$ are the transfer functions of command response and disturbance re-

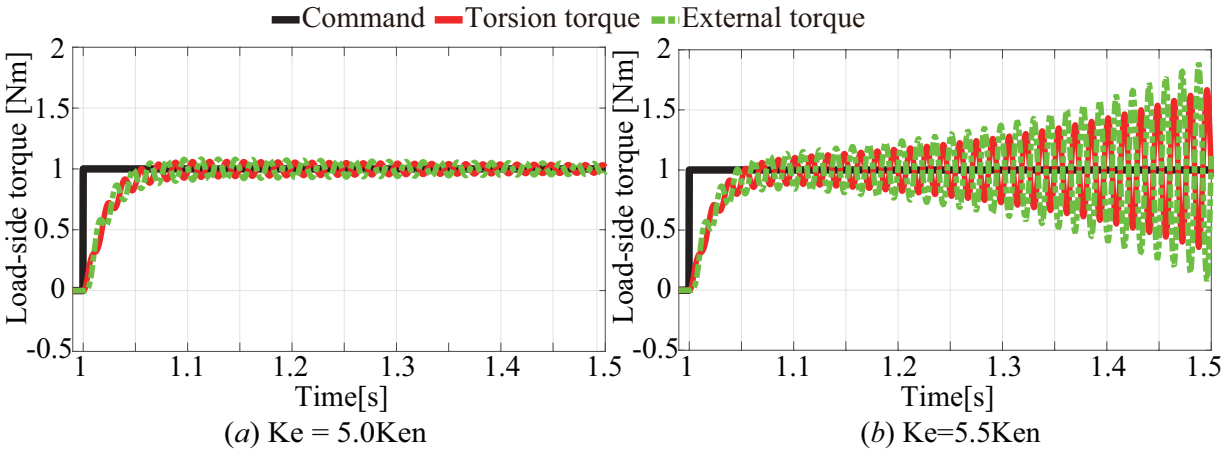


Figure2.20: Simulation results of stability analysis in conventional load-side torque control based on RRC. (a) $K_e = 5.0K_{en}$. (b) $K_e = 5.5K_{en}$. Black, red, and green lines are load-side torque command, torsion torque, and external torque, respectively.

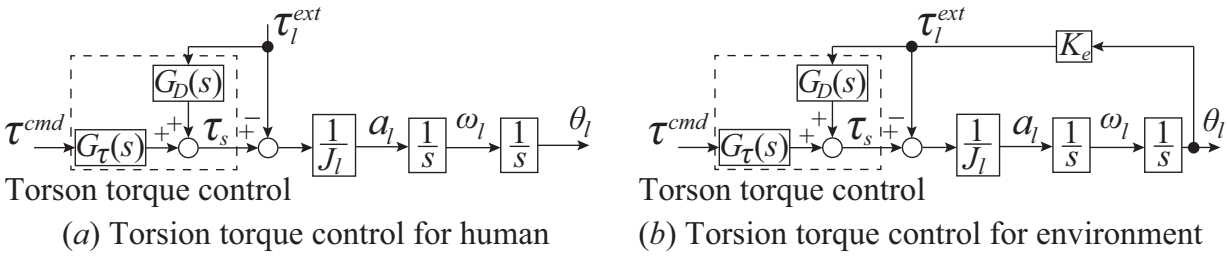


Figure2.21: Block diagram of plant system using back-forward drivable torsion torque control.

sponse in back-forward drivable torsion torque control. $G_\tau(s)$ and $G_D(s)$ are the transfer function that do not include the environmental dynamics, i.e., $K_e = 0$. To enhance human interaction performance, human force should be directly transmitted to the robot actuator. By this, the human operator is able to be easy to manipulate the robot actuator by human hands.

In Fig.2.21, load-side dynamics are expressed as

$$\begin{aligned} J_l a_l &= \tau_s - \tau_l^{ext} \\ &= (G_\tau(s)\tau^{cmd} + G_D(s)\tau_l^{ext}) - \tau_l^{ext}. \end{aligned} \tag{2.65}$$

From Fig.2.21 (a), $G_\tau(s)$ and $G_D(s)$ should be $\lim_{s\to 0} G_\tau(s) = 1.0$ and $\lim_{s\to 0} G_D(s) = 0.0$. If $G_\tau(s) = 1.0$, $\lim_{s\to 0} G_D(s) = 0.0$, and $\tau^{cmd} = 0.0$, the external torque $\tau_l^{ext}$ is directly transmitted

to load-side acceleration $a_l$; therefore, target back-forward drivability in (2.8) is achieved by using torsion back-forward drivable torque control. Moreover, torsion torque detects torsional vibration. Torsion torque control is capable of vibration suppression. Regulating the torsion torque means that back-forward drivability is able to be regulated. For human interaction, (2.65) is expressed as

$$\begin{aligned} J_l a_l &= (G_\tau(s)\tau^{cmd} + G_D(s)\tau_l^{ext}) - \tau_l^{ext} \\ &= \tau^{cmd} - \tau_l^{ext}. \end{aligned} \tag{2.66}$$

Thus, the target back-forward drivability is achieved by controlling torsion torque to zero, i.e., $G_{bf}(s) = a_l/\tau_l^{ext} = 1/J_l$.

On the other hands, for environmental interaction, force gain is determined according to resonance between motor dynamics and environmental dynamics. In general, force gain in acceleration-based force control is correspondence with the inverse of motor mass. To ensure the stability of the control system, control gain is set to small value because control bandwidth is very hard to exceed resonance. In the single-inertia system, it is reported that force gain of acceleration-based force control is able to set high gain that exceeds resonance by adjusting parameters in terms of DOB and Reaction Force Observer (RFOB) [85–87]. However, in a two-inertia system, high control gain may have unstable due to anti-resonant and resonant frequencies. The environmental dynamics and resonant modes of the two-inertia system should be considered for force control design in the case of environment interaction. Especially, the zero-stiffness force control system needs to regulate the back-forward drivability according to environmental dynamics because it has back-forward drivability on the acceleration dimension. As indicated in (2.51), back-forward drivability becomes small in the case of the force control system that is designed considering environmental dynamics. From Fig.2.21 (b), $\lim_{s\to 0} G_\tau(s) = \alpha_1$ and $\lim_{s\to 0} G_D(s) = \alpha_2$. Thus,

$$\begin{aligned} J_l a_l &= \tau_s - \tau_l^{ext} \\ &= (G_\tau(s)\tau^{cmd} + G_D(s)\tau_l^{ext}) - \tau_l^{ext} \\ &= (\alpha_1\tau^{cmd} + \alpha_2\tau_l^{ext}) - \tau_l^{ext} \\ &= \alpha_1\tau^{cmd} - (1-\alpha_2)\tau_l^{ext}. \end{aligned} \tag{2.67}$$

Thus, optimal back-forward drivability in case of environment interaction is determined by force control design considering environmental dynamics. In addition, command response of force control system has steady state error in non-contact phase. Back-forward drivable torsion torque control considering environmental dynamics are defined as

$$G_\tau(s) = \frac{\tau_s}{\tau^{cmd}} = \frac{K(s^2 + \frac{K_e}{J_l})}{(s+p)^n} = \frac{K(s^2 + \omega_{ae}^2)}{(s+p)^n}. \tag{2.68}$$

(2.68) is realized by using pole placement method. Finally, the transfer function from torque command to external torque is expressed as

$$G_{\tau e}(s) = \frac{\tau_l^{ext}}{\tau^{cmd}} = \frac{\tau_s}{\tau^{cmd}} \frac{\tau_l^{ext}}{\tau_s} = G_\tau(s) \frac{\frac{K_e}{J_l}}{s^2 + \frac{K_e}{J_l}} = \frac{K(s^2 + \omega_{ae}^2)}{(s+p)^n} \frac{\omega_{ae}^2}{s^2 + \omega_{ae}^2} = \frac{p^n}{(s+p)^n}, \tag{2.69}$$

where, $p^n = K\omega_{ae}^2$. Back-forward drivable torsion torque control achieves a force control system on the acceleration dimension. When step force command is added, load-side velocity becomes the lamped response. By this, the constant velocity response is not realized for stable contact realization. Therefore, high-performance force control is achieved, but it is difficult to realize stable contact motion from constant velocity motion including free motion at only a force control system that has back-forward drivability on the acceleration dimension. Here, the control target of a back-forward drivable torsion torque control in two-inertia system is defined as

$$\tau_l^{ext} = J_l a_l. \tag{2.70}$$

When regulating torque command to zero, a load-side acceleration is also closed to zero. However, even though an acceleration is close to zero, a velocity has any value, e.g, $\omega = 0$ or $\neq 0$. To realize the anti-bouncing motion during contact with the environment, it is necessary to maintain both acceleration and velocity close to zero after contact with an environmental object. Therefore, the force control based on acceleration control is not able to perfectly contact without bouncing phenomena. Thus, the stable contact motion has been realized by the force control system using velocity feedback and compliance. However, these approaches are not able to achieve the ideal back drivability on the acceleration dimension.

Therefore, to achieve stable contact and back drivable motion, it is necessary to a new control approach. For this, this study utilizes the force impulse based on back-forward drivable torsion torque control. To realize the constant velocity motion, back-forward drivable torsion torque control is transformed to force impulse controller. Then, stable contact motion based on force impulse controller is realized.

## 2.6 Summary of Chapter 2

In this chapter, ideal drivability is defined focusing on acceleration. General force control based on acceleration control is able to realize the ideal drivability for single- and two-inertia system. However, vibration has occurred in the two-inertia system. For two-inertia system, it is necessary to realize the target back-forward drivability as well as vibration suppression. Moreover, for stable force control, environmental dynamics should be considered. Force control considering vibration suppression for the two-inertia system with environment is evaluated on environmental stiffness variation ($K_e$ variation), and the stability analysis results have indicated that there is unstable condition on $K_e$ variation. For this, improvement of robustness on $K_e$ variation is required. In addition, the force control based on acceleration control is not able to perfectly contact without bouncing phenomena. Because even though an acceleration close to zero, a velocity has any value, e.g, $\omega = 0$ or $\neq 0$. The stable contact motion need to satisfy the acceleration and velocity are close to zero when contacting the environment. For these issues, this study proposes the back-forward drivable torsion torque control for environment interaction.

# Chapter3

# High Back-Forward Drivable Torsion Torque Control

## 3.1 Introduction

In the previous chapter, to improve the back drivability, feeding back the actual external torque has been considered. In particular, force control based on acceleration control is generally well known to be a general robust force control system [75,76]. However, force control based on acceleration control incurs vibrations at the load-side in a two-inertia system. Thus, it is necessary to apply vibration suppression control, such as resonance ratio control and state feedback for robot manipulators [64, 71, 72, 78]. Although force control using vibration suppression control has been proposed [64], back drivability is reduced because vibration suppression methods use velocity feedback. Thus, this chapter aims to realize the back drivable concept as shown in Fig.3.1. For the concept shown in Fig.3.1, this study employs a torsion torque control (TTC) to realize vibration suppression while maintaining the back-forward drivability defined in (2.8) of section 2.3.1. In addition, a motor-side normalization compensator (MNC) in a minor-loop is proposed to reduce the friction and normalize the motor parameter in this chapter. The effectiveness of the proposed method is verified through numerical simulations and experiments.

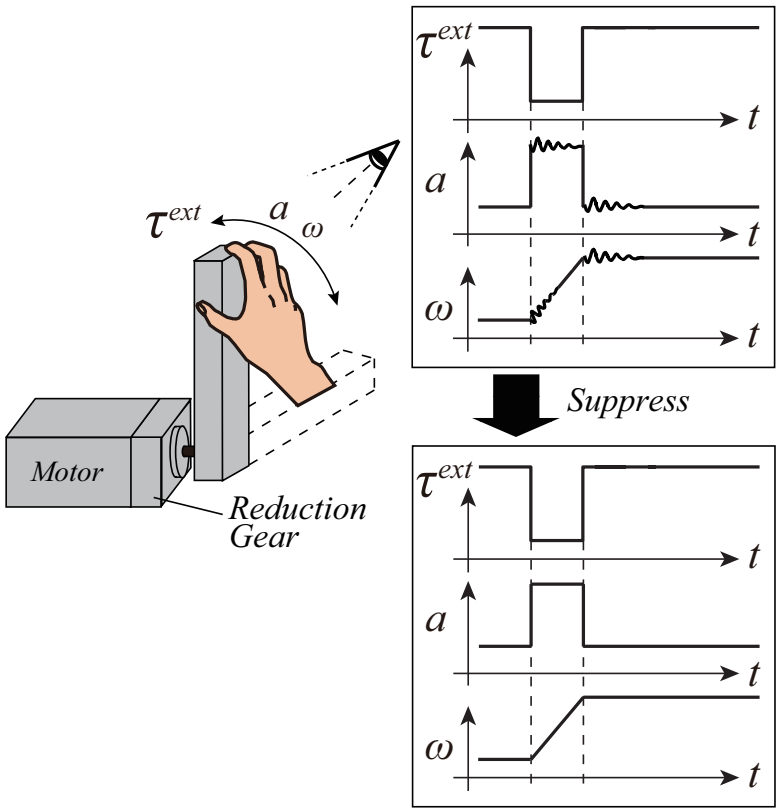


Figure3.1: Concept of back-forward drivable motion in proposed approach.

## 3.2 Interaction Control Based on Back-Forward Drivable Torsion Torque Control

### 3.2.1 Motor-side Normalization Compensator (MNC)

Fig.3.2 shows a block diagram of the MNC. The MNC is based on the DOB. The MNC uses a torsion torque sensor, motor-side current and motor-side encoder. In this paper, the torsion torque sensor has a high bandwidth of 1 kHz. Thus, the bandwidth of the torsion torque sensor is neglected,

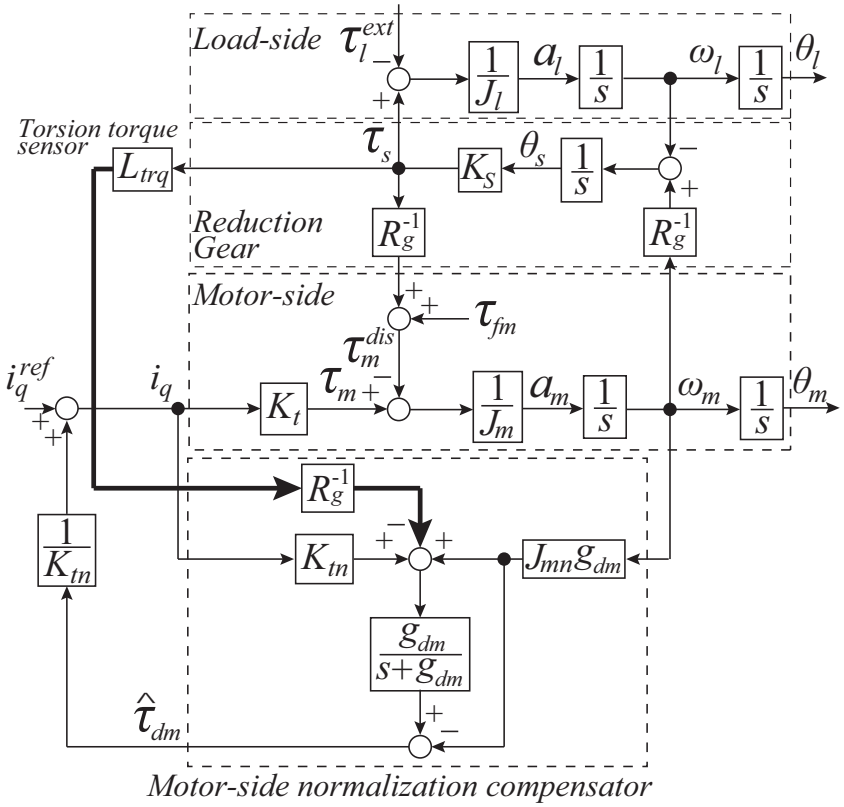


Figure3.2: Block diagram of plant system normalized using MNC (proposed).

i.e., $L_{trq} = 1$. According to Fig.3.2, the motor-side mismatching disturbance $\tau_{dm}$ is estimated as

$$\begin{aligned}\hat{\tau}_{dm} &= \frac{g_{dm}}{s+g_{dm}}\left(K_{tn}i_q - J_{mn}s\omega_m - \frac{\tau_s}{R_g}\right) \\ &= \frac{g_{dm}}{s+g_{dm}}\left(K_{tn}i_q + J_{mn}g_{dm}\omega_m - \frac{\tau_s}{R_g}\right) \\ &\quad -J_{mn}g_{dm}\omega_m. \end{aligned} \tag{3.1}$$

The MNC is able to compensate for the motor-side mismatching disturbance, including the parameter variations and friction. Thus, the MNC is able to improve the back-forward drivability of the two-

inertia system. The back-forward drivability of the plant system employing the MNC is derived as

$$G_{bf}^{MNC}(s) = \frac{a_l}{\tau_l^{ext}} = -\frac{1}{J_l}\Big\{s^3 + \Big(g_{dm} + \frac{D_m}{J_m}\Big)s^2 + \frac{K_s}{J_m R_g^2}s + \frac{K_s g_{dm}}{J_m R_g^2}\Big\}\frac{1}{D_{en}^{MNC}(s)} \tag{3.2}$$

$$D_{en}^{MNC}(s) = s^3 + \Big(g_{dm} + \frac{D_m}{J_m}\Big)s^2 + K_s\Big(\frac{1}{J_m R_g^2} + \frac{1}{J_l}\Big)s + K_s\Big(\frac{1}{J_m R_g^2} + \frac{1}{J_l}\Big)g_{dm} + \frac{K_s D_m}{J_m J_l}. \tag{3.3}$$

According to (3.2), the back-forward drivability has a steady-state term. The friction effect and motor-side parameter variations are compensated using the MNC. A bode diagram of the back-forward drivability is shown in Fig.3.3 to compare the DOB with the MNC. Moreover, the plant system with/without friction is compared. The gain characteristics of the two-inertia system with friction are decreased within the low-frequency range, which indicates that the friction degrades the back-forward drivability. Furthermore, the gain characteristics of the two-inertia system using the DOB are also decreased. Thus, the back-forward drivability is decreased owing to disturbance compensation using the DOB. By contrast, the gain characteristics of the two-inertia system normalized by the MNC are the same as those of the two-inertia system without friction. According to these results, the MNC is able to normalize with the plant system with the exception of friction.

### 3.2.2 Velocity Deviation Observer (VDO)

This paper uses the I-P torsion torque controller and velocity deviation feedback gain, $K_{pt}$, $K_{i1}$, and $f_s$. To feed back the velocity deviation, this paper estimates the velocity deviation $\omega_s$ using a velocity deviation observer (VDO). The state equation of the plant system in VDO is similar to LTOB as shown in (2.12)–(2.18). Using (2.12)–(2.18), the estimation equation of the velocity deviation is

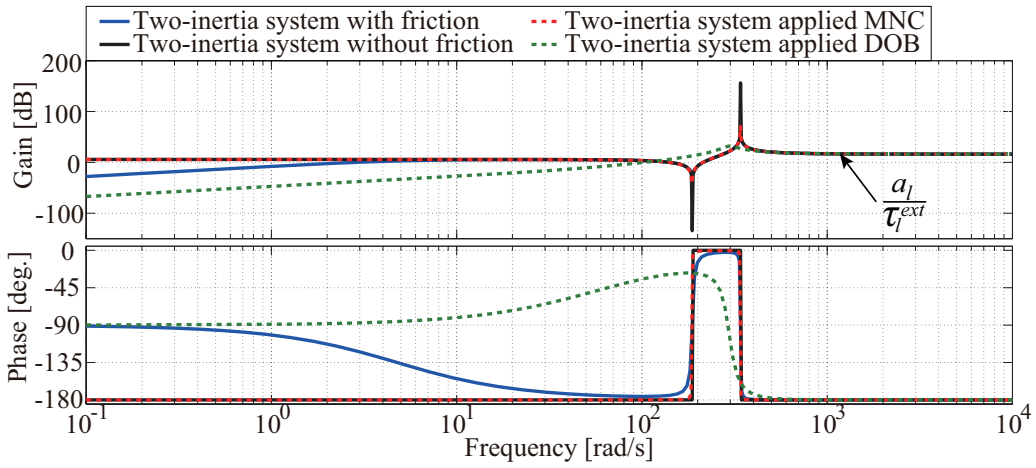


Figure3.3: Bode diagram of two-inertia system controlled by DOB/MNC. Black, blue, gree and red lines are two-inertia system without friction, two-inertia system with friction, two-inertia system applied DOB, and two-inertia system applied MNC, respectively.

obtained using the VDO as follows:

$$\dot{\hat{x}}_l = A_{dl}\hat{x}_l + B_{dl}u_{dl} \tag{3.4}$$

$$y_{dl} = C_{dl}\hat{x}_l + D_{dl}u_{dl} \tag{3.5}$$

$$\hat{x}_l = \begin{bmatrix} \hat{\tau}_s & \hat{\omega}_l & \hat{\tau}_l^{ext} \end{bmatrix}^T \tag{3.6}$$

$$u_{dl} = [\omega_m \ \tau_s]^T, \ y_{dl} = \hat{\omega}_s \tag{3.7}$$

$$A_{dl} = \begin{bmatrix} -(l_1+l_2+l_3) & -K_{sn} & 0 \\ \frac{l_1l_2+l_2l_3+l_3l_1}{K_{sn}} & 0 & -J_{ln}^{-1} \\ -\frac{J_{ln}l_1l_2l_3}{K_{sn}} & 0 & 0 \end{bmatrix} \tag{3.8}$$

$$B_{dl} = \begin{bmatrix} K_{sn}R_g^{-1} & l_1+l_2+l_3 \\ 0 & \frac{1}{J_{ln}} - \frac{l_1l_2+l_2l_3+l_3l_1}{K_{sn}} \\ 0 & \frac{J_{ln}l_1l_2l_3}{K_{sn}} \end{bmatrix} \tag{3.9}$$

$$C_{dl} = \begin{bmatrix} 0 & -1 & 0 \end{bmatrix} \tag{3.10}$$

$$D_{dl} = \begin{bmatrix} R_g^{-1} & 0 \end{bmatrix}, \tag{3.11}$$

where $l_1$, $l_2$, and $l_3$ denote the observer poles. Observer poles are determined as $(s+l_1)(s+l_2)(s+l_3) = 0$. In this paper, observer poles are designed as $l_1 = l_2 = l_3 = g_{dl}$, where $g_{dl}$ denotes the bandwidth of the VDO.

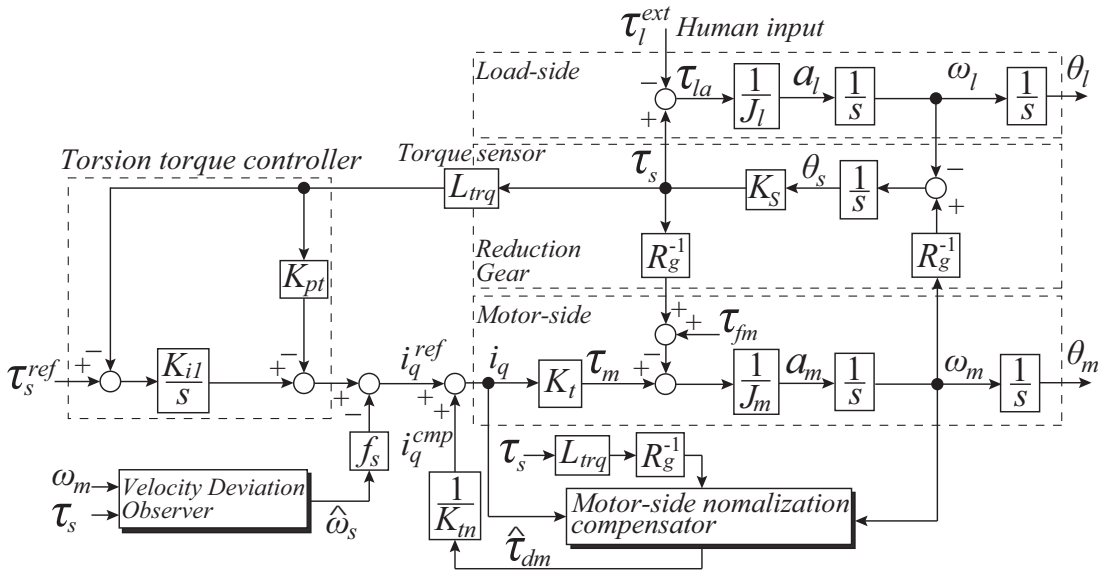


Figure3.4: Block diagram of back-forward drivable control based on TTC using MNC (proposed).

### 3.2.3 Torsion Torque Control (TTC) for Vibration Suppression

The TTC is used to suppress the vibration. In addition, the TTC is applied to realize the same back-forward drivability compared with back-forward drivable control based the load-side torque control at a low frequency. Two integrators are required to satisfy the internal model of torsion torque control which includes disturbances. Therefore, this paper applies the TTC using the MNC, as shown in Fig.3.4. The torsion torque controller comprises an integrator, proportional gain, and velocity deviation feedback. The MNC is used for compensating the motor-side mismatching disturbance, including friction, but also to satisfy the internal model of the TTC. The control gains are designed by assuming that the VDO is able to perfectly estimate the state variables and the plant system is

controlled by the MNC. The transfer function for the TTC system is derived as

$$G_\tau(s) = \frac{\tau_s}{\tau_s^{ref}} = \frac{n_0}{s^3 + d_2 s^2 + d_1 s + d_0} \tag{3.12}$$

$$G_D(s) = \frac{\tau_s}{\tau_l^{ext}} = \frac{s\omega_a^2}{s^3 + d_2 s^2 + d_1 s + d_0} \tag{3.13}$$

$$n_0 = \frac{K_s K_t K_{i1}}{J_m R_g} \tag{3.14}$$

$$d_2 = \frac{K_t f_s}{J_m R_g} \tag{3.15}$$

$$d_1 = \frac{K_s K_t K_{pt}}{J_m R_g} + \frac{K_s}{J_l} + \frac{K_s}{J_m R_g^2} \tag{3.16}$$

$$d_0 = \frac{K_s K_t K_{i1}}{J_m R_g}. \tag{3.17}$$

According to Fig.2.21 (a), back-forward drivable torsion torque control for human interaction needs to $G_\tau(s) \to 1.0$ and $G_D(s) \to 0$. From (3.12)–(3.17), $G_\tau(s) \to 1.0$ and $G_D(s) \to 0$ in steady state. The torsion torque response follows the torsion torque reference and the influence of the external torque in torsion torque response is suppressed. (3.12) and (3.13) show that back-forward drivable torsion torque control for human interaction is realized. Using the pole placement method, the gains of the TTC are designed as follows:

$$\begin{aligned} &(s + P_1)(s + P_2)(s + P_3) \\ &= s^3 + (P_1 + P_2 + P_3)s^2 \\ &+ (P_1 P_2 + P_2 P_3 + P_3 P_1)s + P_1 P_2 P_3 \\ &= s^3 + g_{t2} s^2 + g_{t1} s + g_{t0} \end{aligned} \tag{3.18}$$

$$K_{i1} = \frac{J_m R_g}{K_s K_t} g_{t0} \tag{3.19}$$

$$K_{pt} = \frac{J_m R_g}{K_s K_t} \left\{ g_{t1} - \left( \frac{K_s}{J_l} + \frac{K_s}{J_m R_g^2} \right) \right\} \tag{3.20}$$

$$f_s = \frac{J_m R_g}{K_t} g_{t2}. \tag{3.21}$$

### 3.2.4 Back-Forward Drivable Control Based on TTC and MNC

The back-forward drivability of the proposed back-forward drivable control system is derived as

$$G_{bf}^{Prop.}(s) = \frac{a_l}{\tau_l^{ext}} = -\frac{1}{J_l}\Big\{s^4 + \Big(g_{dm} + \frac{D_m}{J_m} + \frac{K_t f_s}{J_m R_g}\Big)s^3 + \Big(\frac{K_s K_t K_{pt}}{J_m R_g} + \frac{K_t f_s g_{dm}}{J_m R_g} + \frac{K_s}{J_m R_g^2}\Big)s^2 + \Big(\frac{K_s K_t K_{pt} g_{dm}}{J_m R_g} + \frac{K_s K_t K_{i1}}{J_m R_g} + \frac{g_{dm} K_s}{J_m R_g^2}\Big)s + \frac{K_s K_t K_{i1} g_{dm}}{J_m R_g}\Big\}\frac{1}{D_{en}^{Prop.}(s)} \tag{3.22}$$

$$D_{en}^{Prop.}(s) = s^4 + \Big(g_{dm} + \frac{D_m}{J_m} + \frac{K_t f_s}{J_m R_g}\Big)s^3 + \Big(\frac{K_s K_t K_{pt}}{J_m R_g} + \frac{K_t f_s g_{dm}}{J_m R_g} + \frac{K_s}{J_l} + \frac{K_s}{J_m R_g^2}\Big)s^2 + \Big\{\frac{K_s K_t K_{pt} g_{dm}}{J_m R_g} + \frac{K_s K_t K_{i1}}{J_m R_g} + g_{dm}\Big(\frac{K_s}{J_l} + \frac{K_s}{J_m R_g^2}\Big) + \frac{K_s D_m}{J_m J_l}\Big\}s + \frac{K_s K_t K_{i1} g_{dm}}{J_m R_g}, \tag{3.23}$$

in which, assuming that $g_{dm}$ is ideal, (3.22) is able to be expressed as

$$\lim_{g_{dm}\to\infty} G_{bf}^{Prop.}(s) = \lim_{g_{dm}\to\infty} \frac{a_l}{\tau_l^{ext}} = -\frac{1}{J_l}\frac{N_{um}^{Prop.}(s)}{D_{en}^{Prop.}(s)} \tag{3.24}$$

$$N_{um}^{Prop.}(s) = s^3 + \frac{K_t f_s}{J_m R_g}s^2 + \Big(\frac{K_s K_t K_{pt}}{J_m R_g} + \frac{K_s}{J_m R_g^2}\Big)s + \frac{K_s K_t K_{i1}}{J_m R_g} \tag{3.25}$$

$$D_{en}^{Prop.}(s) = s^3 + \frac{K_t f_s}{J_m R_g}s^2 + \Big(\frac{K_s K_t K_{pt}}{J_m R_g} + \frac{K_s}{J_l} + \frac{K_s}{J_m R_g^2}\Big)s + \frac{K_s K_t K_{i1}}{J_m R_g}, \tag{3.26}$$

where, assuming that TTC is designed as (3.18)–(3.21), (3.24) is able to be written as

$$\begin{aligned}\lim_{g_{dm}\to\infty} G_{bf}^{Prop.}(s) &= \lim_{g_{dm}\to\infty} \frac{a_l}{\tau_l^{ext}} \\ &= -\frac{1}{J_l}\Big\{1 - \frac{s\omega_a^2}{(s+P_1)(s+P_2)(s+P_3)}\Big\} \\ &= -\frac{1}{J_l} + \frac{1}{J_l}\frac{s\omega_a^2}{(s+P_1)(s+P_2)(s+P_3)}.\end{aligned} \tag{3.27}$$

From (3.27), the first term is the same as the back-forward drivability shown in (2.28). The second term does not include the vibration term. Therefore, the vibration is suppressed. According to (2.28) and (3.22), Bode diagrams of the back-forward drivability in Figs. 2.8 and 3.4 are shown in Fig.3.5. However, the actuator vibrates owing to the anti-resonant frequency of the plant system, and a smooth human interaction is not realized. In contrast, the proposed back-forward drivable control is able to suppress the vibration by controlling the torsion torque. Moreover, the load-side torque is directly

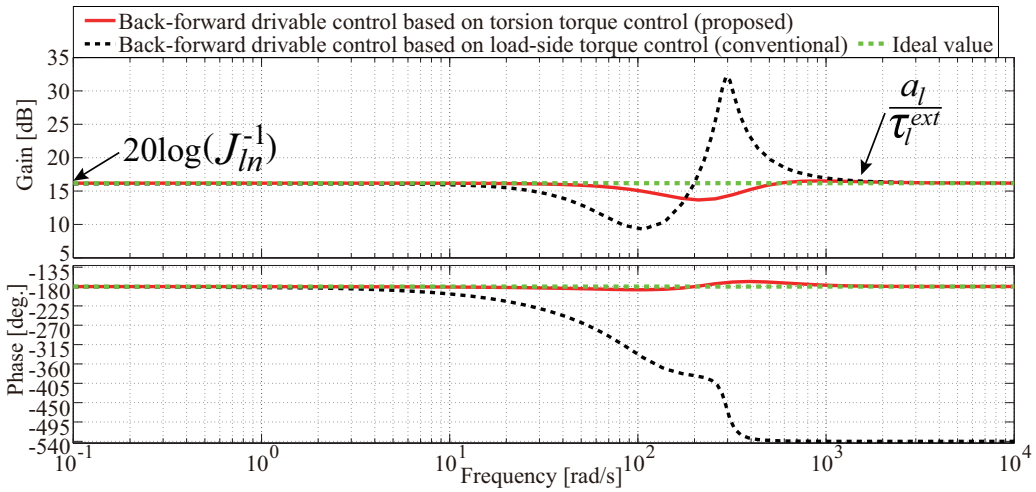


Figure3.5: Bode diagram of back-forward drivability in back-forward drivable control based on LTC or TTC using MNC. Black, red, and green lines are back-forward drivable control based on LTC and TTC using MNC (proposed), and ideal value such as $20\log(1/J_{ln})$, respectively.

transmitted to the load-side acceleration if the torsion torque is controlled at zero. Thus, the proposed back-forward drivable control is able to achieve the vibration suppression while keeping the back-forward drivability.

## 3.3 Numerical Simulation and Experiment

### 3.3.1 Numerical Simulation and Experimental Conditions

In this chapter, a geared motor with a torsion torque sensor is used to improve the back-forward drivability. In this section, two validation experiments are described. First, the TTC using the MNC is confirmed at the command response. In addition, the experimental results are compared with the simulation results. The command torque is set to $\pm 4$ Nm. The torsion torque is measured using a torsion torque sensor. Second, the back-forward drivable response is validated through the experimental results of the back-forward drivable control based on the LTC, the back-forward drivable control based on the TTC, and the plant system without control. The back-forward drivable responses are measured

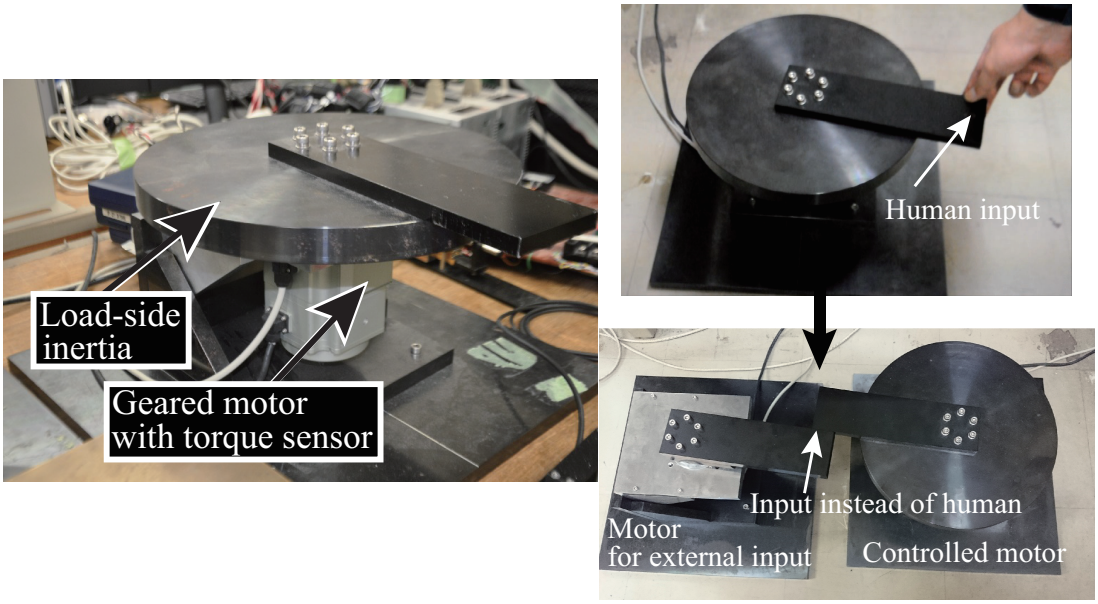


Figure3.6: Experimental equipment.

using an acceleration sensor, a torsion torque sensor, and a two-inertia observer. The experimental equipment is shown in Fig.3.6. In this study, to compare the back-forward drivability, the external torque of human input is added to the controlled motor by another actuator instead of the human input. The plant and control parameters are listed in Tables 3.1 and 3.2.

### 3.3.2 Numerical Simulation and Experimental Results

The command response for the TTC using the MNC in Fig.3.4 is shown in Figs. 3.7 and 3.8. According to Figs. 3.7 and 3.8, the simulation and experiment obtain the same response. Thus, the TTC is designed as expected. Fig.3.9 shows the experimental results obtained in terms of the back-forward drivable response in Figs. 2.8 and 3.4, and the plant system without control. According to these results, the impact torque of the two back-forward drivable controls is smaller than the plant system without control. The plant system without control reduces the back-forward drivability. However, two back-forward drivable controls improve the back-forward drivability. Back-forward drivable control based on the TTC is able to suppress the vibration while keeping the back-forward drivability as

Table3.1: Plant parameters.

| | | |
|---|---|---|
| Torque constant | $K_{tn}$ | 0.49 Nm/A |
| Motor − side inertia | $J_{mn}$ | $1.44 \times 10^{-4}$ kgm$^2$ |
| Motor viscosity coefficient | $D_{mn}$ | $9.80 \times 10^{-4}$ Nms/rad |
| Load − side inertia | $J_{ln}$ | 0.16 kgm$^2$ |
| Torsion spring constant | $K_{sn}$ | $1.26 \times 10^4$ Nm/rad |
| Gear ratio | $R_g$ | 50.0 |
| Resonance frequency | $\omega_r$ | 54.2 Hz(341rad/s) |
| Anti − resonance frequency | $\omega_a$ | 45.3 Hz(285rad/s) |

Table3.2: Control parameters.

| | | |
|---|---|---|
| Load − side torque gain | $C_t$ | $1/J_{ln}$ 1/kgm$^2$ |
| Bandwidth of torsion torque controller | $g_{ts}$ | 350 rad/s |
| Torque proportional gain | $K_{pt}$ | 0.030 |
| Torque integral gain | $K_{i1}$ | 50.06 |
| Velocity deviation feedback gain | $f_s$ | 15.42 |
| Bandwidth of VDO | $g_{dl}$ | 350 rad/s |
| Bandwidth of DOB and MNC | $g_{dm}$ | 628 rad/s |
| Bandwidth of torsion torque sensor | $g_{trq}$ | 6280 rad/s |

compared with back-forward drivable control based on the LTC. Thus, the conceptual motion in this chapter, as shown in Fig.2.5, is achieved.

### 3.3.3 Analysis of Load-side Parameter Variations: Load-side Inertia $J_l$ and Torsion Stiffness $K_s$

To analyze the effect of variations in parameters $J_l$ and $K_s$, this section examines the Bode diagrams in terms of back-forward drivability of proposed and conventional back-forward drivable control sys-

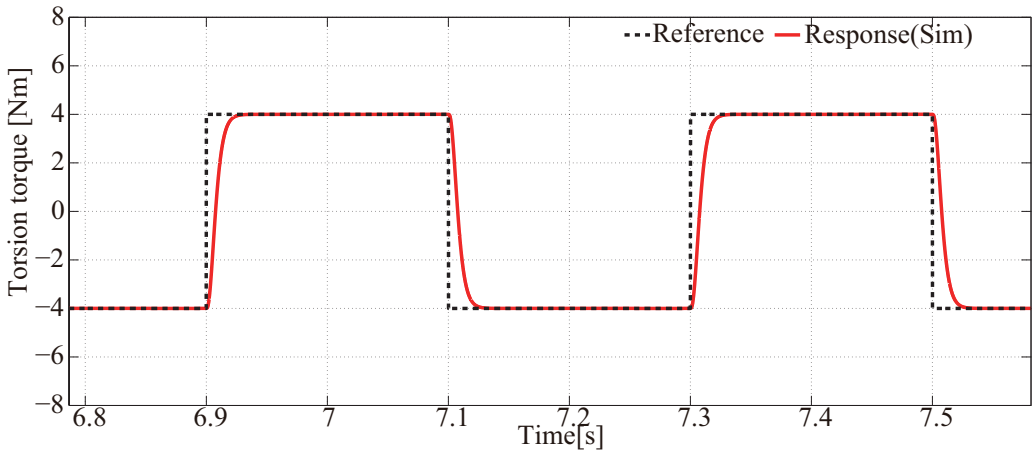


Figure3.7: Simulation results in terms of command response of TTC using MNC. Black and red lines are reference and response, respectively.

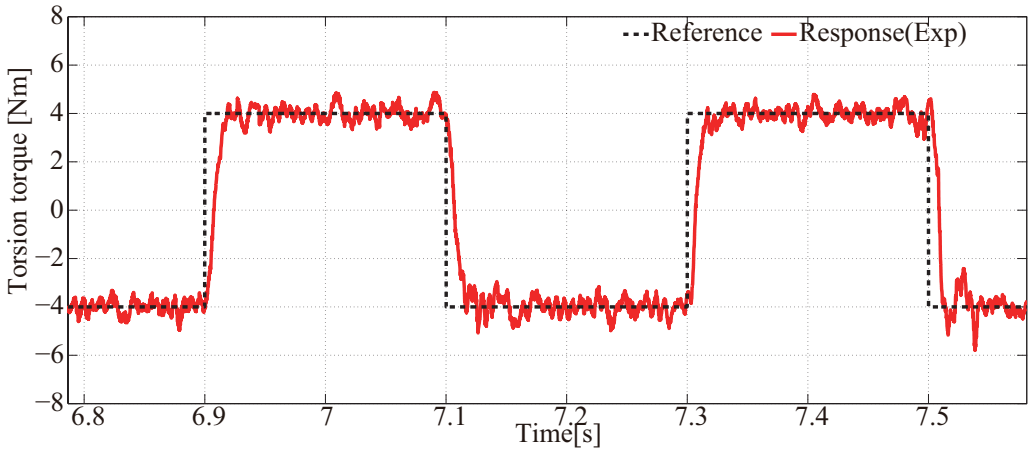


Figure3.8: Experimental results in terms of command response of TTC using MNC. Black and red lines are reference and response, respectively.

tems, as shown in Fig.3.10 and Fig.3.11, respectively. From Fig.3.10, the conventional method is not affected by $J_l$ variation in the low-frequency range, but vibration has not been suppressed. In contrast, the proposed method achieves vibration suppression and realizes almost the same flat gain characteristics. However, the proposed method is affected by $J_l$ variation. Although it is barely affected in this experimental system, it is necessary to consider the $J_l$ variation in case of the manipulator. Regulation of load-side inertia is achieved using torsion torque reference. This will be considered in future work. As shown in Fig.3.11, both the proposed and conventional methods are not affected by the influence of

$K_s$ variation in the low-frequency range. Moreover, as indicated in Fig.3.5, the conventional method involves vibrations at the anti-resonant frequency of the plant system, while the proposed method is able to suppress the vibration.

## 3.4 Summary of Chapter3

This chapter proposes a high back-forward drivable torsion torque control (TTC) using a motor-side normalization compensator (MNC) to facilitate human-robot interactions. Although the back-forward drivable control based on load-side torque control (LTC) (see Fig.2.8 and Fig.3.9) is able to enhance the back-forward drivability, the back-forward drivable response vibrates. The proposed back-forward drivable control (TTC using MNC) is able to achieve vibration suppression while maintaining the back-forward drivability. The back-forward drivable response is drastically improved, and the effectiveness of the proposed method is verified through numerical simulation result and experimental result.

In this chapter, human-robot interaction performance is improved and human is able to manipulate the robot actuator, easily.

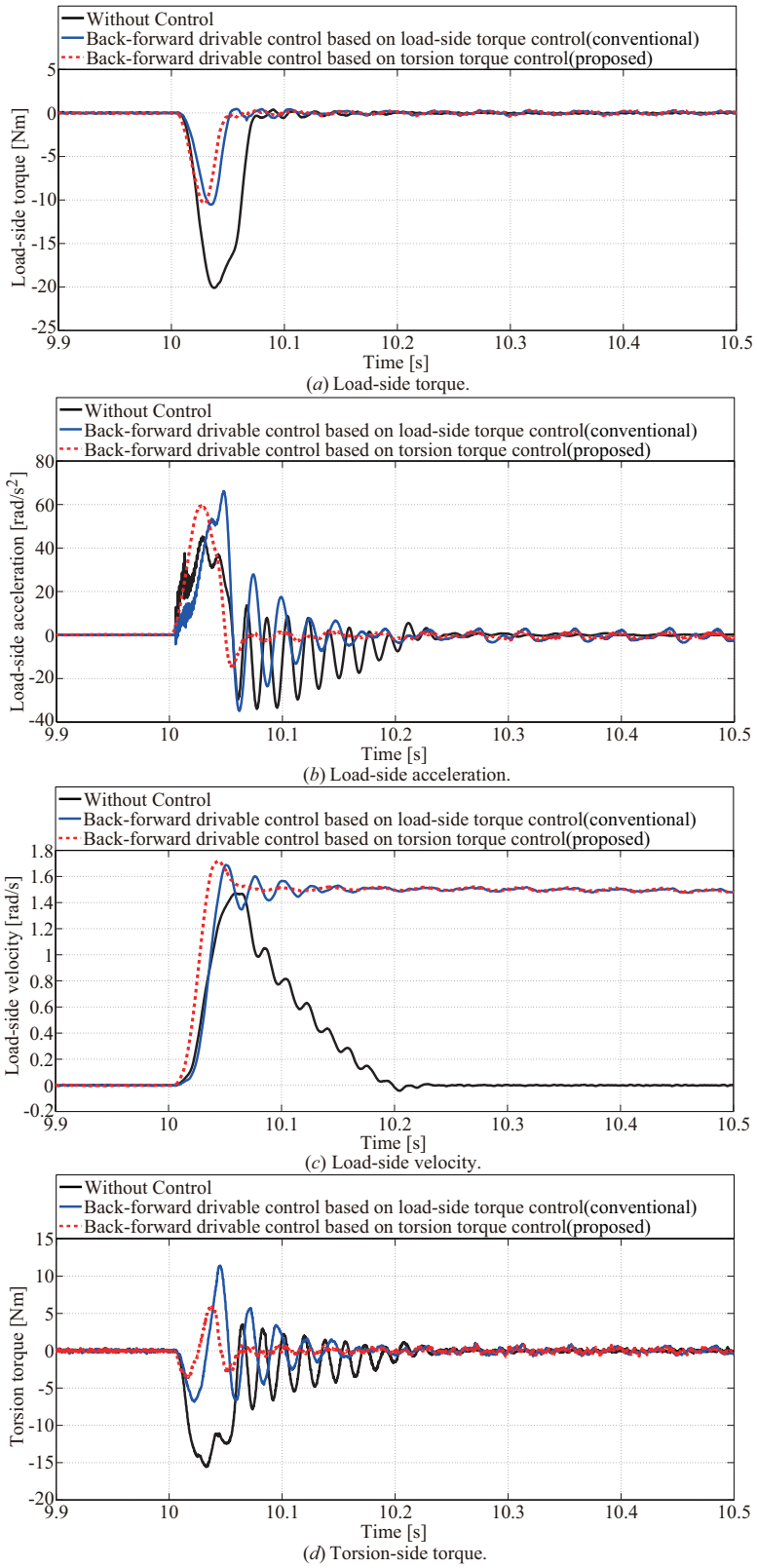


Figure3.9: Experimental results in terms of back-forward drivable response. Blue, red and blue lines are back-forward drivable control based on LTC, back-forward drivable control based on TTC, and without control system, respectively. (a) Load-side torque. (b) Load-side acceleration. (c) Load-side velocity. (d) Torsion torque.

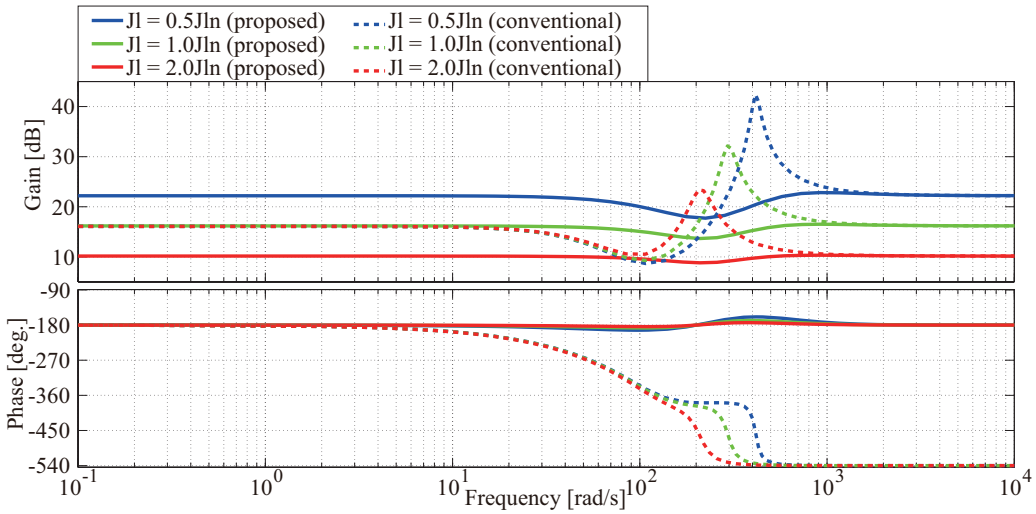


Figure3.10: Bode diagram in terms of back-forward drivability under $J_l$ variation. Solid and dashed lines are proposed and conventional back-forward drivable control system.

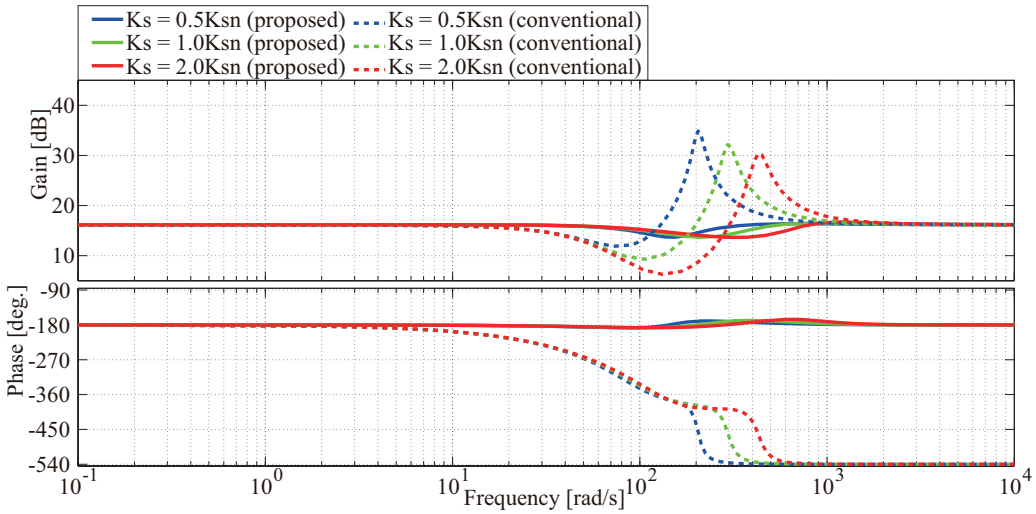


Figure3.11: Bode diagram in terms of back-forward drivability under $K_s$ variation. Solid and dashed lines are proposed and conventional back-forward drivable control system.

# Chapter4

# High-Robust Back-Forward Drivable Torsion Torque Control Against Environmental Stiffness Variation

## 4.1 Introduction

According to Chapter 2, conventional force control based on RRC is discussed for environmental interaction. However, conventional force control based on RRC indicated that there is unstable condition during $K_e$ variation, as unraveled in Sections 2.4.7 and 2.4.8. The purpose of this chapter is to realize the high-robust force control against the $K_e$ variation in a model-based approach. A geared SPMSM with a torsion torque sensor is used in this study [42]. Conventionally, a two-inertia system with the environment has two-resonant frequencies, so that the optimal resonance ratio is not able to be determined in the conventional force control system based on RRC in [40]. A torque-velocity duality is focused in this chapter and a two-spring system is constructed using the motor-side velocity control, which is the collocate side [95–100]. Motor-side velocity control is able to be designed at a higher bandwidth than the vibration modes of the plant system because of not including vibration modes. Therefore, an equivalent RRC (ERRC) is proposed based on the two-spring system using motor-side velocity control, as shown in Fig.4.1. The ERRC is an equivalent structure to the RRC

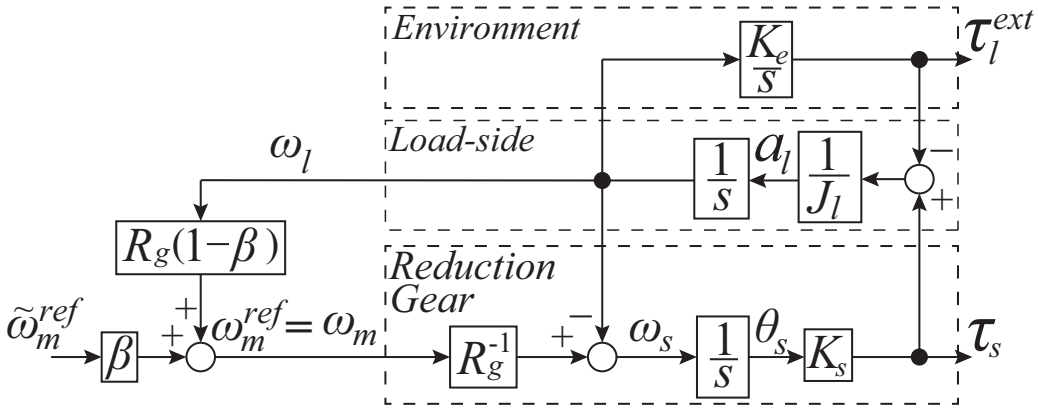


Figure4.1: Block diagram of ERRC of two-spring system (proposed).

applied for position/velocity controls [72, 74], and the ERRC provides optimal resonance ratio similar to [72]. The robustness against $K_e$ variation is achieved based on back-forward drivable torsion torque control using the ERRC. In this chapter, the robust stability of control system is evaluated from open-loop characteristics and small gain theorem. Two load-side sensors, namely the torsion torque and acceleration sensors are used to evaluate the force control in the experiment, and the effectiveness of the proposed method is demonstrated using numerical simulation and experimental results.

## 4.2 Two-Spring System Focusing on Duality

First of all, this section discusses how to construct the two-spring system for realizing the high-robust force control system. To achieve stable contact with the environment, it is necessary to suppress vibrations, because a robot actuator is modeled as a two-inertia system. The effect of the environment must be considered for stable contact realization in a two-inertia system. The conceptual figure for the equivalent transformation of a two-spring system from a two-inertia system with the environment is shown in Fig.4.2. Here, the plant parameters correspond to the motor inertia $J_m$, torsion stiffness $K_s$, load inertia $J_l$, and environmental stiffness $K_e$.

Generally, several vibration suppression methods have been proposed for the two-inertia system without environment, as shown on the left section of Fig.4.2. When an environment is considered,

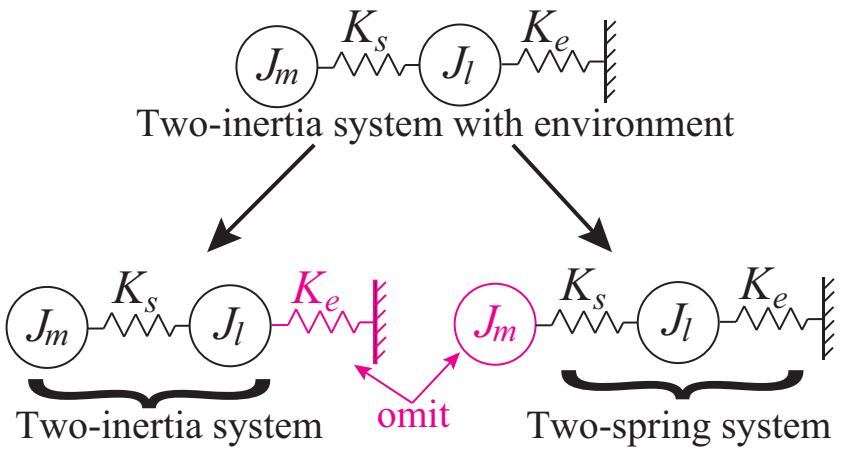


Figure4.2: Conceptual figure for equivalent transformation of two-spring system from two-inertia system with environment.

two resonant frequencies need to be considered for vibration suppression. However, this complicates the control design. Thus, if the two-inertia system is assumed to be a two-spring system as shown on the right section of Fig.4.2, the same control scheme as that of the two-inertia system without an environment is able to be used for the two-inertia system with an environment. The simple control design is able to be applied by this assumption. Fig.4.3 shows the Block diagram of a two-inertia system with the environment and correspondence of the physical model in this chapter. In Fig.4.3, black dot line is two-inertia system with environment. Red line is two-inertia system without environment. Blue line is two-spring system. Therefore, two-inertia system in red line is shown in Fig.4.4, and two-spring system in blue line is shown in Fig.4.5.

Here, two-spring system focused in this chapter uses the motor-side velocity reference as the input of actuator. However, actual experimental equipment generally uses the current reference as the input of actuator. For this, to realize the two-spring system, motor-side velocity control is applied for a two-inertia system with the environment. In addition, to improve the motor-side disturbance suppression performance, this study applies the disturbance observer using torsion torque sensor that is called as the force and position sensors integrated disturbance observer (FPIDO) [94]. The two-inertia system using the FPIDO is shown in Fig.4.6, where the motor-side disturbance $\tau_m^{dis}$ consists

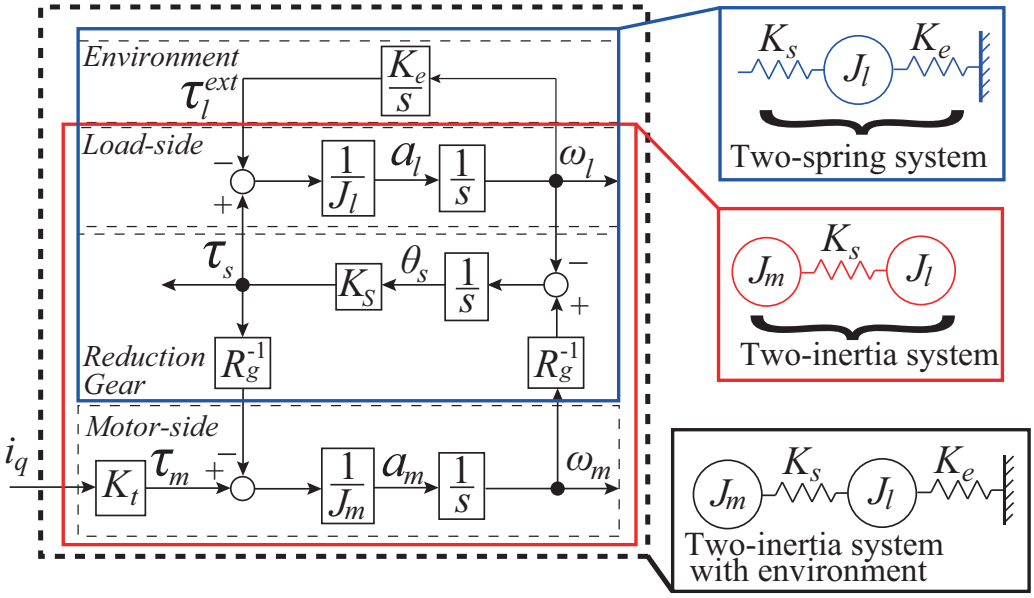


Figure4.3: Block diagram of two-inertia system with environment and correspondence of physical model in this paper.

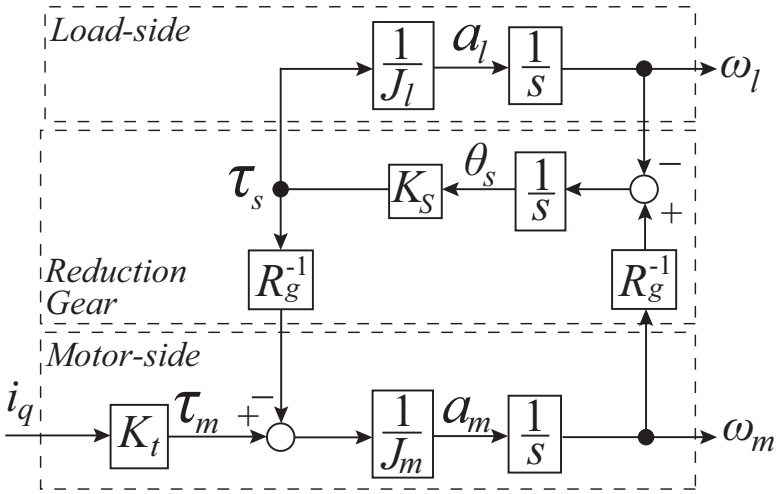


Figure4.4: Block diagram of two-inertia system.

of torsion torque and other disturbances, including friction and parameter variation. From this figure, equivalent block diagram of Fig.4.6 in terms of motor-side disturbance part is expressed as shown in Fig.4.7. In Fig.4.7, $g_{trq}$ and $g_{dm}$ are the bandwidth of torsion torque sensor and FPIDO. From Fig.4.7, the bandwidth of torsion torque sensor $g_{trq}$ is 1 kHz; thus, this study does not need to consider the

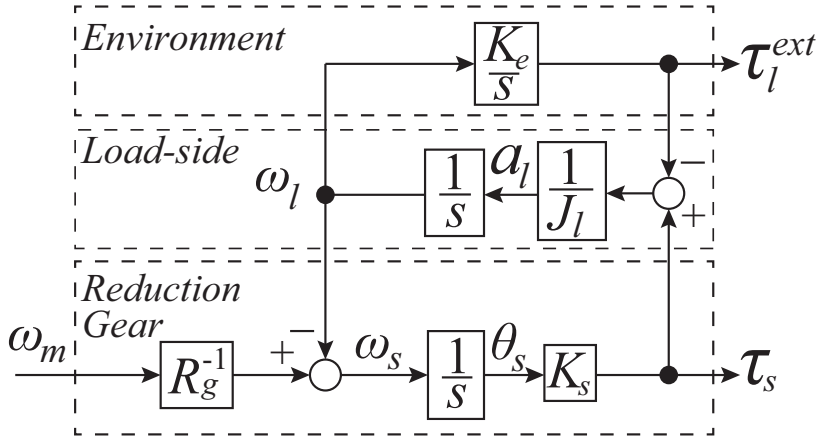


Figure4.5: Block diagram of two-spring system.

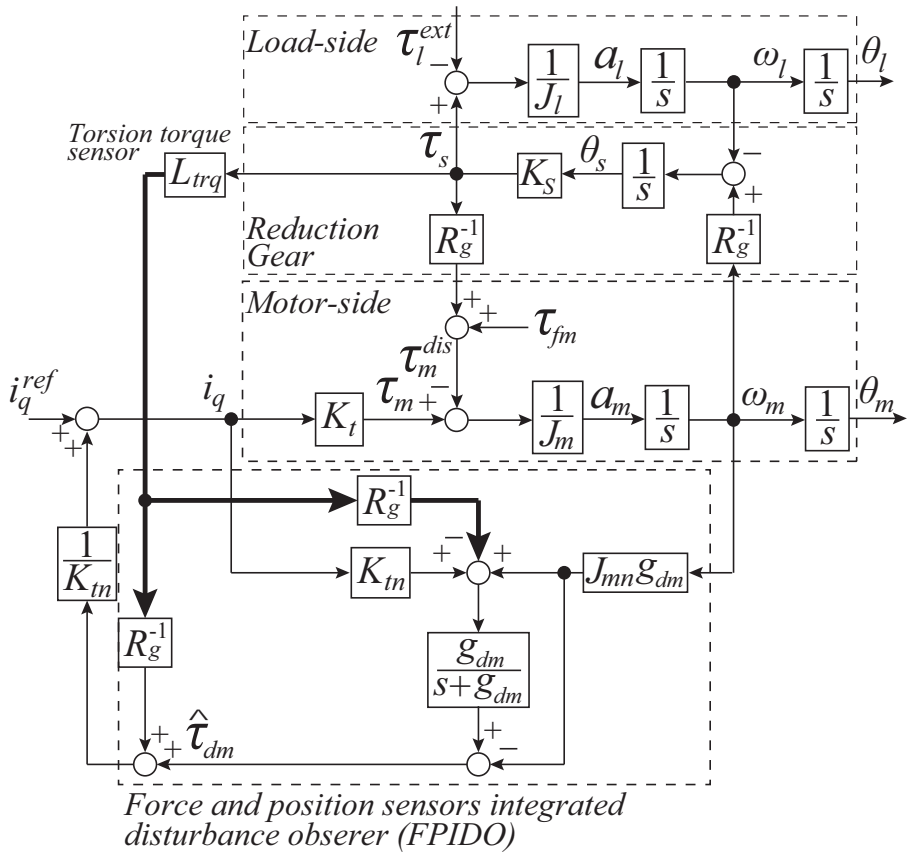


Figure4.6: Block diagram of two-inertia system using FPIDO.

motor-side disturbance from torsion torque. Therefore, Fig.4.8 shows the two-spring system based on the motor-side velocity control because of assuming that the motor-side disturbance is neglected.

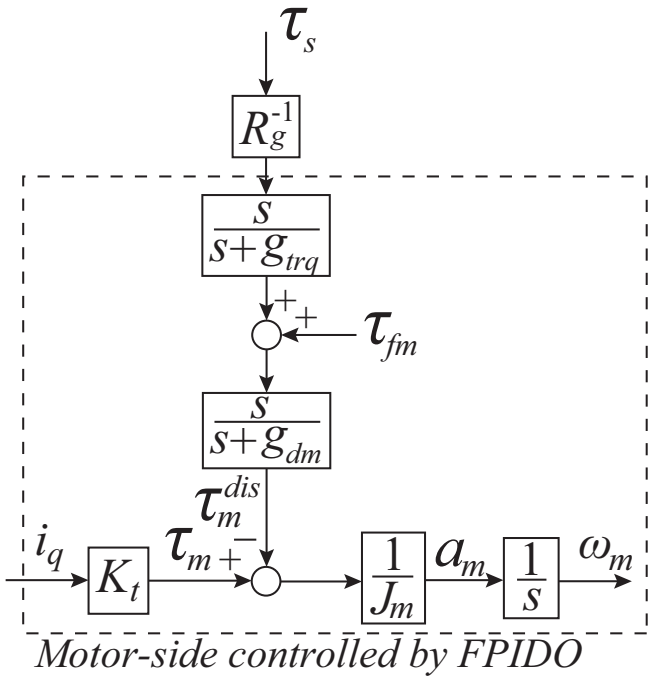


Figure4.7: Equivalent block diagram of Fig.4.6 in terms of motor-side disturbance part.

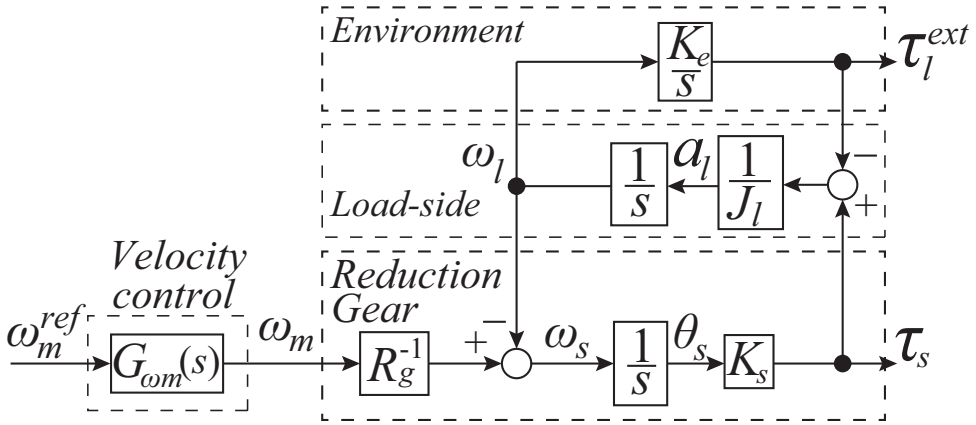


Figure4.8: Block diagram of two-spring system based on motor-side velocity control.

The transfer function $G_{\omega m}(s)$ of the motor-side velocity control is calculated as follows:

$$G_{\omega m}(s) = \frac{\omega_m}{\omega_m^{ref}} = \frac{\frac{K_t}{J_m}\left(K_{ps}s + K_{is}\right)}{s^2 + \frac{K_t K_{ps}}{J_m}s + \frac{K_t K_{is}}{J_m}}$$
$$= \frac{2\zeta_s\omega_n s + \omega_n^2}{s^2 + 2\zeta_s\omega_n s + \omega_n^2} \tag{4.1}$$
$$K_{ps} = \frac{2\zeta_s\omega_n J_{mn} - D_{mn}}{K_{tn}} \tag{4.2}$$
$$K_{is} = \frac{J_{mn}\omega_n^2}{K_{tn}}, \tag{4.3}$$

where $K_{ps}$ and $K_{is}$ are the velocity proportional and velocity integral gains, respectively. $K_t$, $J_m$, $K_{ps}$, $K_{is}$, $\omega_n$ and $\zeta$ denote torque constant, motor inertia, velocity proportional gain, velocity integral gain, bandwidth of motor-side velocity control and damping coefficient, respectively.

In (4.1), this study considers the ideal case of the motor-side velocity control. The motor-side inertia $J_m$ does not become zero in the actual plant system, but if the transfer function from the motor-side velocity reference $\omega_m^{ref}$ to the motor-side velocity $\omega_m$ is regarded as one, i.e., $G_{\omega m}(s) = 1$, the motor-side inertia is regarded as a very small value. In other words, when the bandwidth of motor-side velocity control is enough high compared with the control bandwidth of the outer loop, $J_m$ is able to be neglected from the design of outer control system. Therefore, this study designs the load-side torque control system neglecting the motor-side inertia.

## 4.3 Proposed Load-side Torque Control Based on Back-Forward Drivable Torsion Torque Control

### 4.3.1 Precondition

In this section, the precondition is defined as follows: 1) a geared SPMSM with a torsion torque sensor is utilized, as shown in Fig.4.9. 2) the sensor dynamics are not considered due to the sensor bandwidth of 1 kHz, i.e., 6280 rad/s. 3) the dynamics of the electric circuit for motor are not considered. In this paper, two load-side sensors, i.e., torsion torque and load-side acceleration sensors, are used. The torsion torque sensor is mounted at the load-side of gear shaft and it has a high bandwidth

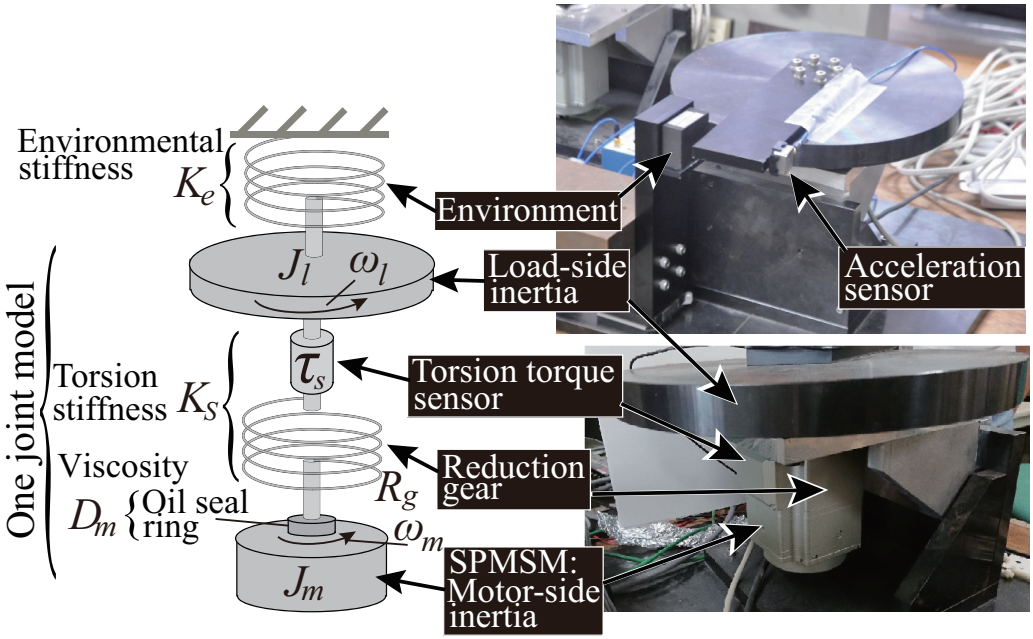


Figure4.9: Configuration figure of experimental equipment and experimental setup.

of 1 kHz. To evaluate the external torque, the external torque is directly detected using both torsion torque and load-side acceleration sensors. The load-side acceleration sensor also has high bandwidth of 1 kHz and it is attached at the tip of the actuator arm. Therefore, the dynamics of the torsion torque and load-side acceleration sensors are not considered. In the electric circuit, the motor is actuated at current control of 1 kHz. The dynamics of the electric circuit are not considered.

### 4.3.2 Equivalent RRC Based on Motor-side Velocity Control and First-order Load-side Velocity Observer (LVOB)

As mentioned in Section 2.4.3, it is difficult to determine the resonance ratio $H_r$ of the two-inertia system with the environment unlike for the system without the environment in (2.30) because it has two resonant frequencies, i.e., $\omega_{r1}^{RRC}$ and $\omega_{r2}^{RRC}$. Therefore, to simplify the resonance ratio, this study constructs the two-spring system based on the torque-velocity duality, and realizes an equivalent RRC (ERRC) as shown in Fig.4.1. Furthermore, the motor-side velocity control and first-order LVOB are applied to realize the ERRC; moreover, because the semi-closed loop of the motor-side velocity

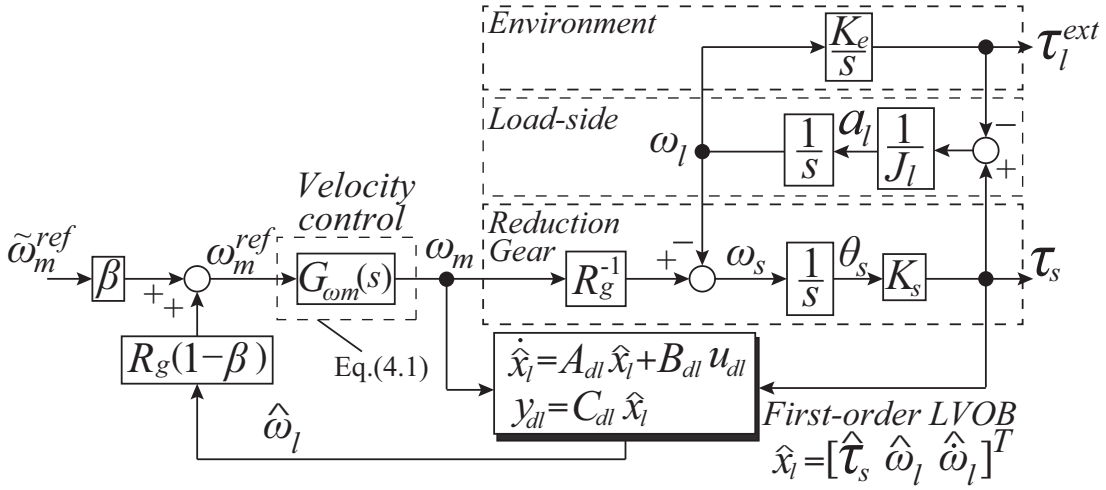


Figure4.10: Block diagram of ERRC based on motor-side velocity control system with first-order LVOB.

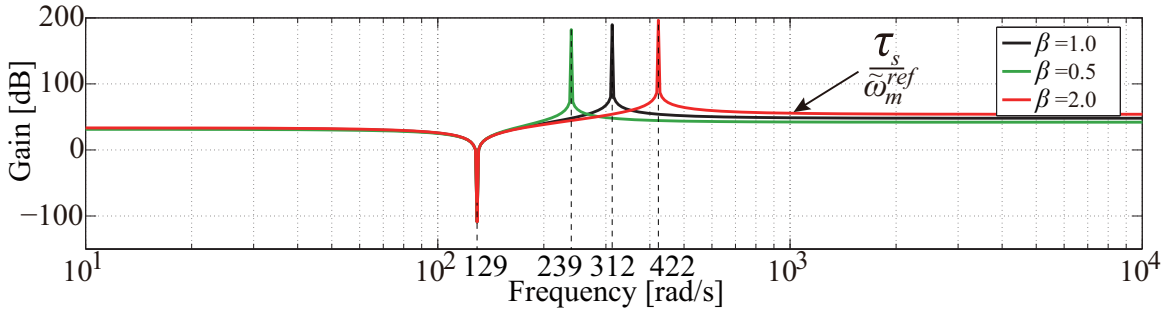


Figure4.11: Frequency characteristics of Fig.4.1 in case that $G_{\omega m}(s) = 1$ and $\hat{\omega}_l = \omega_l$. Black, red and green lines are $\beta = 1.0$, $0.5$ and $2.0$, respectively.

control, which uses a basic PI controller, is constructed at the collocated side, the stability of the force control system is improved [95–101]. In addition, this section applies the first-order LVOB, which estimates the load-side velocity using the motor-side velocity $\omega_m$ and torsion torque $\tau_s$. Fig.4.10 shows the block diagram of the ERRC for the two-spring system. This system employs a motor-side velocity control and the first-order LVOB. Here, it is assumed that the motor-side velocity control system and first-order LVOB are ideal, i.e., $G_{\omega m}(s) = 1$ and $\hat{\omega}_l = \omega_l$. This study observes that

Fig.4.10 is equivalent to Fig.4.1, and the transfer function from $\widetilde{\omega}_m^{ref}$ to $\tau_s$ is derived as

$$\frac{\tau_s}{\widetilde{\omega}_m^{ref}} = \frac{K_s R_g^{-1}\beta\left(s^2 + \frac{K_e}{J_l}\right)}{s\left(s^2 + \frac{K_e+\beta K_s}{J_l}\right)} = \frac{K_s R_g^{-1}\beta\left(s^2 + \omega_{ae}^2\right)}{s\left(s^2 + (\omega_{re}^{ERRC})^2\right)} \tag{4.4}$$

$$\omega_{re}^{ERRC} = \sqrt{\frac{K_e + K_s\beta}{J_l}} = \sqrt{\frac{K_e + K_s^{'}}{J_l}} \tag{4.5}$$

$$K_s^{'} = K_s\beta, \tag{4.6}$$

where, $\omega_{re}^{ERRC}$ is the resonant frequency of two-spring system controlled by ERRC, as shown in Fig.4.1. Here, (4.4)–(4.6) have similar structure of equation compared with equations of RRC without environment indicated in (2.30)–(2.32). The difference of these equations is whether the plant system is the two-inertia system without the environment or the two-spring system. Therefore, RRC uses a torsion torque, but the ERRC uses a load-side velocity. In addition, the two-spring system is able to apply not only ERRC that is similar structure to RRC, but also other control approaches, e.g., full state feedback, etc. By focusing on a torque-velocity duality, these controllers are able to be designed at the same control order and the same approach compared with position/velocity control for the two-inertia system. From (4.4)–(4.6), the ERRC is able to regulate not only the torsion stiffness but also the resonant frequency through the resonance ratio gain $\beta$. The frequency characteristics of (4.4) are shown in Fig.4.11: the variations in the resonant frequency $\omega_{re}^{ERRC}$ for different values of $\beta$, specifically $\beta$ =1.0, 0.5, and 2.0, are shown in the figure.

### 4.3.3 Torque-Velocity Duality in Figs. 2.11 and 4.1

To validate the torque-velocity duality, the relationship in terms of Figs. 2.11 and 4.1 is organized in Table4.1. A two-inertia system is composed of the motor-side inertia $J_m$, the torsion stiffness $K_s$, and the load-side inertia $J_l$. Meanwhile, the two-spring system shown in Fig.4.1 is expressed using $K_s$, $J_l$, and $K_e$. This study observes that the state variables of the two-inertia system have correspondence with those of the two-spring system: for example, $\omega_m$ of the two-inertia system corresponds to $\tau_s$ of the two-spring system. Therefore, the two-spring and two-inertia systems exhibit that there is a

Table4.1: Duality in plant parameters of Figs. 2.11 and 4.1.

| Plant parameter of Fig.2.11 | Plant parameter of Fig.4.1 |
|---|---|
| $\frac{1}{J_{mn}}$ | $K_{sn}$ |
| $K_{sn}$ | $\frac{1}{J_{ln}}$ |
| $\frac{1}{J_{ln}}$ | $K_{en}$ |
| $\omega_m$ | $\tau_s$ |
| $\tau_s$ | $\omega_l$ |
| $\omega_l$ | $\tau_l^{ext}$ |

relationship of duality between the torque and velocity. Moreover, Fig.4.1 utilizes the same control approach as the control design approach proposed for position and velocity controls, as reported in [72], for applying torque control to the two-inertia system considering the environment.

### 4.3.4 Load-side Torque Control Based on Back-Forward Drivable Torsion Torque Control using ERRC (Proposed)

This section evaluates the proposed load-side torque control system. An overview of the proposed load-side torque control system is illustrated in Fig.4.12, which is composed of a motor-side velocity control, a FPIDO, a first-order LVOB, and an I-P torque controller. The FPIDO is applied to eliminate the motor-side disturbance $\hat{\tau}_m^{dis}$. For control design, motor-side dynamics are neglected and the first-order LVOB is considered to be able to be accurately estimated without delay. Thus, Fig.4.10 is expressed as Fig.4.1. Therefore, the high-robust load-side torque control system is constructed, as illustrated in Fig.4.13, using a semi-closed torsion torque control and has a structure similar to the RRC for the velocity or position controls. Finally, equivalent block diagram of proposed method for control design is expressed as shown in Fig.4.14. The closed-loop transfer function $G_{\tau}^{cl,Prop.}(s)$ from

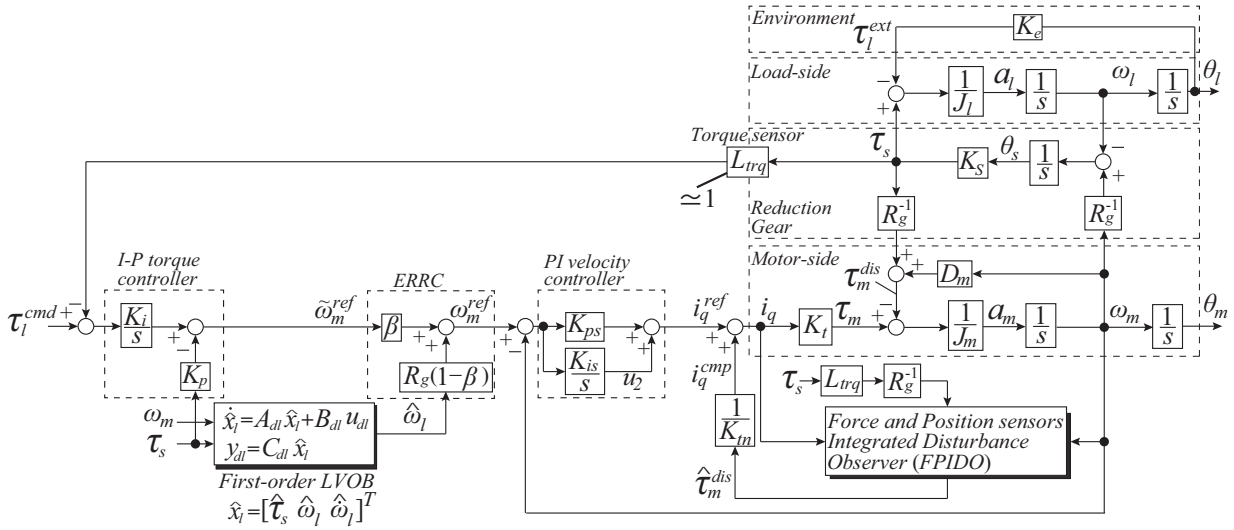


Figure4.12: Overview of load-side torque control (proposed).

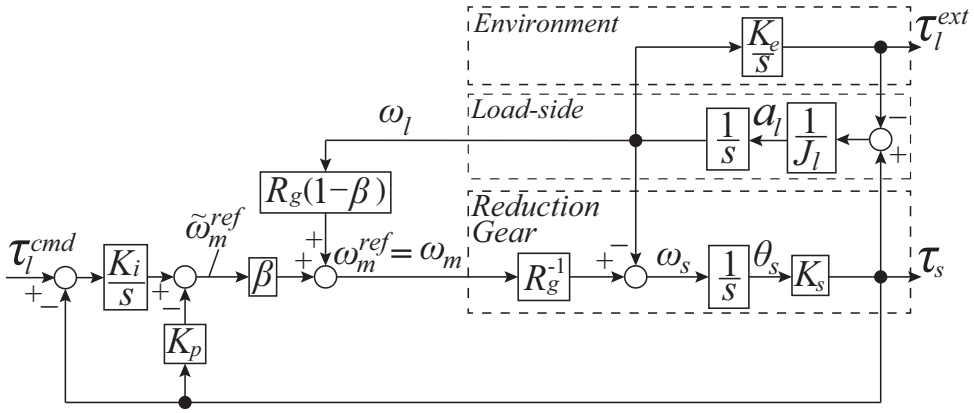


Figure4.13: Block diagram of proposed load-side torque control in case of $G_{\omega m}(s) = 1$ and $\hat{\omega}_l = \omega_l$.

load-side torque command $\tau_l^{cmd}$ to torsion torque $\tau_s$ (see Fig.4.14) is derived as follows:

$$
\begin{aligned}
G_{\tau}^{cl,Prop.}(s) &= \frac{\tau_s}{\tau_l^{cmd}} = \frac{K_s R_g^{-1} \beta K_i (s^2 + \omega_{ae}^2)}{D_{en}^{prop.}(s)} \\
D_{en}^{prop.}(s) &= s^4 + \frac{K_s \beta}{R_g} K_p s^3 + ((\omega_{re}^{ERRC})^2 + \frac{K_s \beta}{R_g} K_i) s^2 \\
&\quad + \frac{K_s \beta}{R_g} K_p \omega_{ae}^2 s + \frac{K_s \beta}{R_g} K_i \omega_{ae}^2 \qquad (4.7) \\
&= s^4 + a_3^{cl,Prop.} s^3 + a_2^{cl,Prop.} s^2 + a_1^{cl,Prop.} s + a_0^{cl,Prop.}. \qquad (4.8)
\end{aligned}
$$

The control gains are achieved by the binomial design using the stability indices $\gamma_i$ and the resonance

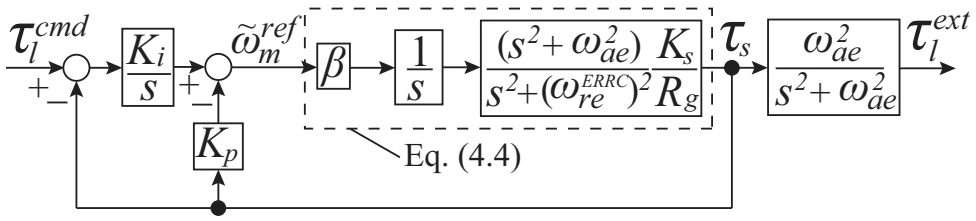


Figure4.14: Equivalent block diagram of Fig.4.13 in proposed load-side torque control for control design.

ratio $H_r$ are calculated using (4.7) and (4.8), as follows:

$$\beta = \frac{K_{en}}{K_{sn}} \frac{\gamma_1\gamma_2\gamma_3 - \gamma_3 - \gamma_1}{\gamma_1}. \tag{4.9}$$

$$K_i = \frac{R_g}{K_{sn}} \frac{\gamma_3}{\gamma_1} \frac{\omega_{ae}^2}{\beta} \tag{4.10}$$

$$K_p = \frac{R_g}{K_{sn}} \sqrt{\gamma_2}\gamma_3 \frac{\omega_{ae}}{\beta} \tag{4.11}$$

$$H_r = \frac{\omega_{re}^{ERRC}}{\omega_{ae}} = \sqrt{(\gamma_1\gamma_2 - 1)\frac{\gamma_3}{\gamma_1}}, \tag{4.12}$$

where (4.9)– (4.12) are determined so as to satisfy $\gamma_1$, $\gamma_2$, and $\gamma_3$. Furthermore, the control gains in case of the binomial design, i.e., at $\gamma_i = [2.667\ 2.25\ 2.667]^T$ are calculated as

$$\beta = \frac{4K_{en}}{K_{sn}} \tag{4.13}$$

$$K_i = \frac{\omega_{ae}^2}{\beta} \frac{R_g}{K_{sn}} = \frac{R_g}{4J_{ln}} \tag{4.14}$$

$$K_p = \frac{4\omega_{ae}}{\beta} \frac{R_g}{K_{sn}} = \sqrt{\frac{K_{en}}{J_{ln}}} \frac{R_g}{K_{en}}. \tag{4.15}$$

There are three control gains in the proposed method and the number of the proposed control gain is less than the number of the conventional one. Here, (4.13)–(4.15) to (4.7), the transfer function $G_{\tau e}^{cl,Prop.}(s) = \tau_l^{ext}/\tau_l^{cmd}$ from the load-side torque command $\tau_l^{cmd}$ to the external torque $\tau_l^{ext}$ is calculated as

$$\begin{aligned} G_{\tau e}^{cl,Prop.}(s) &= \frac{\tau_l^{ext}}{\tau_l^{cmd}} = \frac{\tau_l^{ext}}{\tau_s} \frac{\tau_s}{\tau_l^{cmd}} \\ &= \frac{\omega_{ae}^2}{s^2+\omega_{ae}^2} \frac{\omega_{ae}^2(s^2+\omega_{ae}^2)}{(s+\omega_{ae})^4} = \frac{\omega_{ae}^4}{(s+\omega_{ae})^4}. \end{aligned} \tag{4.16}$$

From (4.16), the proposed load-side torque control is designed as 4th-order transfer function. Therefore, the smooth load-side torque response is realized by semi-closed loop control using just torsion

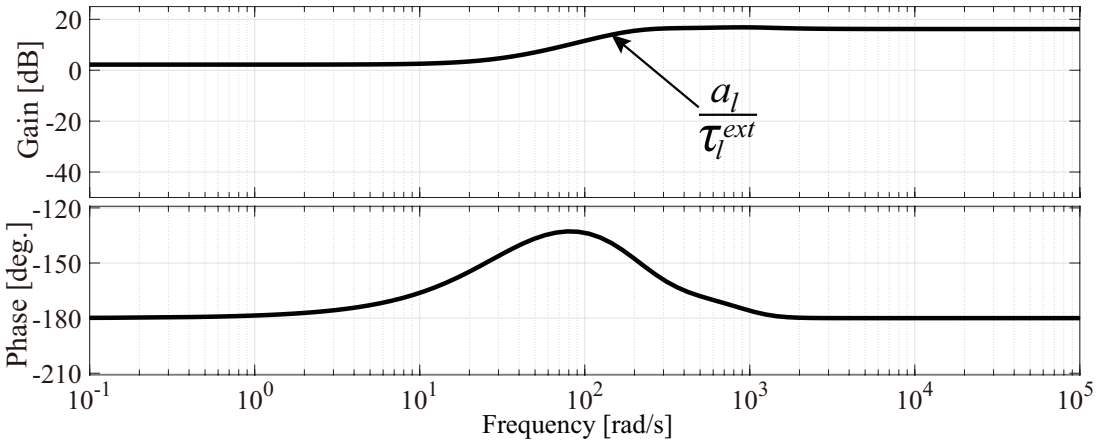


Figure4.15: Bode diagram of back-forward drivability in terms of proposed load-side torque control in non-contact phase.

torque feedback. The equivalent time constant $\tau_c$ is calculated as

$$\tau_c = \frac{1}{\omega_{ae}}\gamma_1\sqrt{\gamma_2} = \frac{4}{\omega_{ae}}. \tag{4.17}$$

Finally, the resonance ratio $H_r$ when $\gamma_i = [2.667\ 2.25\ 2.667]^T$ is calculated from (4.12) as follows:

$$H_r = \frac{\omega_{re}^{ERRC}}{\omega_{ae}} = \sqrt{(\gamma_1\gamma_2 - 1)\frac{\gamma_3}{\gamma_1}} = \sqrt{5}. \tag{4.18}$$

Therefore, the optimal resonance ratio is uniquely obtained in this paper and it is the same as that proposed in [72].

### 4.3.5 Back-Forward Drivability of Proposed Load-side Torque Control

From Fig.4.12, back-forward drivability of proposed load-side torque control is shown in Fig.4.15, where Fig.4.15 includes all dynamics.

The back-forward drivability has constant value at low-frequency region. Therefore, back-forward drivability on acceleration dimension is realized. Here, to simplify the discussion, this section considers ideal condition as shown in Fig.4.13. In the ideal condition, minor-loop dynamics are neglected, i.e., $\omega_l = \omega_l$, $G_{\omega m}(s) = 1$, and $L_{trq}(s) = 1$. In Fig.4.13, command and load-side input responses in

terms of back-forward drivable torsion torque control system are expressed as

$$G_{\tau}^{Prop.Chap4}(s)\Big|_{K_e=0} = \frac{\tau_s}{\tau_l^{cmd}}\Big|_{K_e=0} = \frac{\frac{K_s\beta K_i}{R_g}}{s^2 + \frac{K_s\beta K_p}{R_g}s + \frac{K_s\beta K_i}{R_g} + \frac{K_s\beta}{J_l}} \tag{4.19}$$

$$G_{D}^{Prop.Chap4}(s)\Big|_{K_e=0} = \frac{\tau_s}{\tau_l^{ext}}\Big|_{K_e=0} = \frac{\frac{K_s\beta}{J_l}}{s^2 + \frac{K_s\beta K_p}{R_g}s + \frac{K_s\beta K_i}{R_g} + \frac{K_s\beta}{J_l}}. \tag{4.20}$$

From (4.19) and (4.20), final state values are calculated as

$$\lim_{s\to 0} sG_{\tau}^{Prop.Chap4}(s)\frac{1}{s} = \frac{\frac{K_s\beta K_i}{R_g}}{\frac{K_s\beta K_i}{R_g} + \frac{K_s\beta}{J_l}} = \frac{J_l}{J_l + 4J_{ln}} \tag{4.21}$$

$$\lim_{s\to 0} sG_{D}^{Prop.Chap4}(s)\frac{1}{s} = \frac{\frac{K_s\beta}{J_l}}{\frac{K_s\beta K_i}{R_g} + \frac{K_s\beta}{J_l}} = \frac{4J_{ln}}{J_l + 4J_{ln}}. \tag{4.22}$$

Here, from Fig.2.21 (b), $G_{\tau}(s)$ and $G_D(s)$ are determined by considering environmental dynamics as follows: $\lim_{s\to 0} G_{\tau}(s) = \alpha_1$ and $\lim_{s\to 0} G_D(s) = \alpha_2$. Namely, (4.21) and (4.22) are calculated as $\lim_{s\to 0} G_{\tau}(s)^{Prop.Chap4} = 1/5$ and $\lim_{s\to 0} G_D^{Prop.Chap4}(s) = 4/5$. Finally, the back-forward drivability of proposed load-side torque control is derived as

$$G_{bf}^{Prop.Chap4}(s) = \frac{a_l}{\tau_l^{ext}} = -\frac{1}{J_l}\frac{s^2 + \frac{K_s\beta K_p}{R_g}s + \frac{K_s\beta K_i}{R_g}}{s^2 + \frac{K_s\beta K_p}{R_g}s + \frac{K_s\beta K_i}{R_g} + \frac{K_s\beta}{J_l}}. \tag{4.23}$$

Then, the final state value is calculated as

$$\lim_{s\to 0} sG_{bf}^{Prop.Chap4}(s)\frac{1}{s} = -\frac{1}{J_l}\frac{\frac{K_s\beta K_i}{R_g}}{\frac{K_s\beta K_i}{R_g} + \frac{K_s\beta}{J_l}} = -\frac{1}{5J_l}, \tag{4.24}$$

where, $J_{ln} = J_l$. In (4.24), the back-forward drivability in steady state is smaller value than the back-forward drivability of back-forward drivable torsion torque control in Chapter 3. This means the load-side inertia becomes large from the view of load-side input. Therefore, the back-forward drivability is adjusted to a small value according to control design in case of considering environmental dynamics.

## 4.4 Robust Stability Analysis

To examine the stability of the proposed methods for realizing a high-robust force control, it is necessary to evaluate their robustness against the $K_e$ variation. This section evaluates the gain and

phase margins for the proposed methods, under the $K_e$ variation. In addition, the system uncertainty is analyzed using the small gain theorem similar to Section 2.4.6.

### 4.4.1 Gain and Phase Margins for Proposed Method.

In the proposed method of Fig.4.12, the open-loop transfer function $G_\tau^{op,Prop.}(s) = \tau_s/\tau_l^{cmd}$ from the load-side torque command $\tau_l^{cmd}$ to torsion torque $\tau_s$ is derived as

$$G_\tau^{op,Prop.}(s) = \frac{\tau_s}{\tau_l^{cmd}} = \sum_{i=0}^{7} n_i^{op,Prop.} s^i \Big/ \Big( s^{10} + \sum_{i=1}^{9} d_i^{op,Prop.} s^i \Big), \tag{4.25}$$

where,

$$d_9^{op,Prop.} = g_{dm} + \frac{D_m}{J_m} + k_1 + \frac{K_{ps}K_t}{J_m} \tag{4.26}$$

$$\begin{aligned} d_8^{op,Prop.} &= \Big(g_{dm} + \frac{D_m}{J_m}\Big)k_1 + \frac{\beta K_p K_{ps} K_s K_t}{J_m R_g} + \omega_{ar}^2 \\ &+ \frac{K_t}{J_m} d_A - k_2 K_s \end{aligned} \tag{4.27}$$

$$\begin{aligned} d_7^{op,Prop.} &= \Big(g_{dm} + \frac{D_m}{J_m}\Big)(\omega_{ar}^2 - k_2 K_s) + k_1 \omega_{ar}^2 - k_3 K_s \\ &+ \frac{K_t}{J_m} d_B + \frac{K_{ps}K_t}{J_m}\omega_{ar}^2 - \frac{k_2 K_{ps} K_s K_t}{J_m} \\ &+ \frac{\beta K_p K_s K_t}{J_m R_g} d_A \end{aligned} \tag{4.28}$$

$$\begin{aligned} d_6^{op,Prop.} &= (k_1\omega_{ar}^2 - k_3 K_s)\Big(g_{dm} + \frac{D_m}{J_m}\Big) - k_2 K_s \omega_{ar}^2 \\ &+ \omega_{ae}^2 \frac{K_t}{J_m} d_A + \frac{\beta K_p K_s K_t}{J_m R_g} d_B \\ &+ \frac{K_{is} K_s K_t}{J_m J_l} d_A + \frac{K_s K_t}{J_m} d_D + \frac{g_{dm} k_1 K_{is} K_t}{J_m} \\ &+ \omega_{ae}^2 \frac{\beta K_p K_{ps} K_s K_t}{J_m R_g} - \frac{\beta k_2 K_p K_{ps} K_s^2 K_t}{J_m R_g} \end{aligned} \tag{4.29}$$

$$\begin{aligned} d_5^{op,Prop.} &= -K_s \omega_{ar}^2 \Big\{ k_2 \Big(g_{dm} + \frac{D_m}{J_m}\Big) + k_3 \Big\} \\ &+ \frac{K_t}{J_m}\omega_{ar}^2 d_B - \frac{K_s K_t}{J_m} d_C - \frac{k_2 K_{ps} K_s K_t}{J_m} (\omega_{re}^{ERRC})^2 \\ &+ \frac{\beta K_p K_s K_t}{J_m R_g} (g_{dm} k_1 K_{is} + \omega_{ae}^2 d_A - K_s d_D) \end{aligned} \tag{4.30}$$

$$
\begin{aligned}
d_4^{op,Prop.} &= -k_3K_s\Big(g_{dm}+\frac{D_m}{J_m}\Big)\omega_{ar}^2+\frac{g_{dm}k_1K_{is}K_t}{J_m}\omega_{ar}^2 \\
&- \frac{g_{dm}k_3K_{is}K_sK_t}{J_m}-\frac{K_sK_t}{J_m}d_D(\omega_{re}^{ERRC})^2 \\
&- \frac{\beta K_sK_tK_p}{J_mR_g}(\omega_{ae}^2k_2K_{ps}K_s-d_B\omega_{ae}^2+K_sd_C) && (4.31)\\
d_3^{op,Prop.} &= \omega_{ae}^2\frac{\beta g_{dm}k_1K_{is}K_pK_sK_t}{J_mR_g}-\frac{\beta g_{dm}k_3K_{is}K_pK_s^2K_t}{J_mR_g} \\
&- (\omega_{re}^{ERRC})^2\frac{K_sK_t}{J_m}d_C-\omega_{ae}^2\frac{\beta K_s^2K_tK_p}{J_mR_g}d_D && (4.32)\\
d_2^{op,Prop.} &= -\omega_{ae}^2\frac{\beta K_s^2K_tK_p}{J_mR_g}d_C-(\omega_{re}^{ERRC})^2\frac{g_{dm}k_3K_{is}K_sK_t}{J_m} && (4.33)\\
d_1^{op,Prop.} &= -\omega_{ae}^2\frac{\beta g_{dm}k_3K_{is}K_pK_s^2K_t}{J_mR_g} && (4.34)\\
n_7^{op,Prop.} &= \frac{\beta K_iK_{ps}K_sK_t}{J_mR_g} && (4.35)\\
n_6^{op,Prop.} &= \frac{\beta K_iK_sK_t}{J_mR_g}d_A && (4.36)\\
n_5^{op,Prop.} &= \frac{\beta K_iK_sK_t}{J_mR_g}(d_B+\omega_{ae}^2K_{ps}-k_2K_{ps}K_s) && (4.37)\\
n_4^{op,Prop.} &= \frac{\beta K_iK_sK_t}{J_mR_g}(g_{dm}k_1K_{is}+\omega_{ae}^2d_A-K_sd_D) && (4.38)\\
n_3^{op,Prop.} &= \frac{\beta K_sK_tK_i}{J_mR_g}(\omega_{ae}^2d_B-K_sd_C-\omega_{ae}^2k_2K_{ps}K_s) && (4.39)\\
n_2^{op,Prop.} &= \omega_{ae}^2\frac{\beta g_{dm}k_1K_iK_{is}K_sK_t}{J_mR_g}-\frac{\beta g_{dm}k_3K_iK_{is}K_s^2K_t}{J_mR_g} \\
&- \omega_{ae}^2\frac{\beta K_iK_s^2K_t}{J_mR_g}d_D && (4.40)\\
n_1^{op,Prop.} &= -\omega_{ae}^2\frac{\beta K_s^2K_tK_i}{J_mR_g}d_C && (4.41)\\
n_0^{op,Prop.} &= -\omega_{ae}^2\frac{\beta g_{dm}k_3K_iK_{is}K_s^2K_t}{J_mR_g} && (4.42)\\
d_A &= K_{is}+g_{dm}K_{ps}+k_1K_{ps} && (4.43)\\
d_B &= g_{dm}K_{is}+k_1K_{is}+g_{dm}k_1K_{ps} && (4.44)\\
d_C &= g_{dm}k_2K_{is}+k_3K_{is}+g_{dm}k_3K_{ps} && (4.45)\\
d_D &= k_2K_{is}+g_{dm}k_2K_{ps}+k_3K_{ps}, && (4.46)
\end{aligned}
$$

where, $g_{dm}$ denotes the bandwidth of the FPIDO and $k_1$, $k_2$ and $k_3$ are the observer gains of the first-order LVOB. Fig.4.16 and Table4.2 present the Bode diagram of (4.25) and the gain and phase

Table4.2: Gain and phase margins of proposed methods.

| $K_e$ | Gain margin, dB | Phase margin, deg. |
|---|---|---|
| $0.5K_{en}$ | 52.339 | 61.594 |
| $1.0K_{en}$ | 46.700 | 72.670 |
| $2.0K_{en}$ | 41.465 | 79.369 |
| $3.0K_{en}$ | 38.748 | 81.708 |
| $4.0K_{en}$ | 37.063 | 82.888 |
| $5.0K_{en}$ | 35.937 | 83.597 |
| $5.5K_{en}$ | 35.511 | 83.856 |

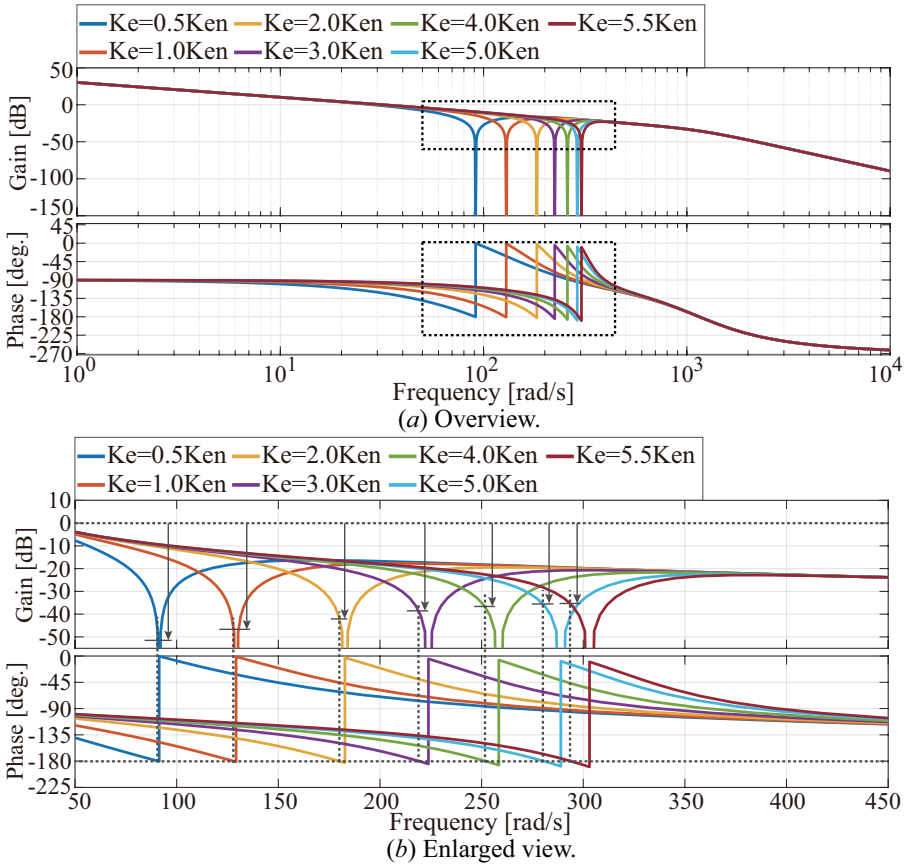


Figure4.16: Bode diagram of open-loop transfer function in proposed method. (a) Overview. (b) Enlarged view.

margins of the proposed method, respectively. As shown in Table4.2, the proposed method indicates that there are sufficiently high gain and phase margins. Moreover, the gain margins of the proposed method are ensured compared with those of the conventional method when the actual environmental stiffness $K_e$ becomes higher than the nominal environmental stiffness $K_{en}$, i.e., $K_e > K_{en}$. Therefore, the proposed method has robustness against $K_e$ variation.

### 4.4.2 Robust Stability Analysis using Small Gain Theorem for Proposed Method

Similar to section 2.4.5, general system $G_{\tau n}^{op,Prop.}(s) = \tau_s/\tau_l^{cmd}$ in proposed method is defined as

$$G_{\tau n}^{op,Prop.}(s) = \frac{\tau_s}{\tau_l^{cmd}} = \sum_{i=0}^{7} n_{in}^{op,Prop.} s^i \Big/ \left( s^{10} + \sum_{i=1}^{9} d_{in}^{op,Prop.} s^i \right). \tag{4.47}$$

Therefore, the multiplicative variation $\Delta^{Prop.}(s)$ and complementary sensitivity function $T^{Prop.}(s)$ in proposed method are calculated as

$$\Delta^{Prop.}(s) = \frac{G_{\tau}^{op,Prop.}(s) - G_{\tau n}^{op,Prop.}(s)}{G_{\tau n}^{op,Prop.}(s)} \tag{4.48}$$

$$T^{Prop.}(s) = \frac{G_{\tau n}^{op,Prop.}(s)}{1 + G_{\tau n}^{op,Prop.}(s)}. \tag{4.49}$$

Finally, Fig.4.17 shows bode diagram in terms of $T^{Prop.}(s)$ and $(\Delta^{Prop.}(s))^{-1}$ in proposed method on $K_e$ variation. As shown in Fig.4.17, the proposed method satisfies $T^{Prop.}(s) < (\Delta^{Prop.}(s))^{-1}$ on $K_e$ variation. Therefore, the robustness of proposed method is higher than that of conventional method against $K_e$ variation.

## 4.5 Simulation and Experiment

### 4.5.1 Numerical Simulation and Experimental Conditions

In the simulation and experiments, this section confirms the step response of proposed method on $K_e$ variations. $K_e$ variations are set to $K_e = 5.0K_{en}$ and $K_e = 5.5K_{en}$ to verify the stable step

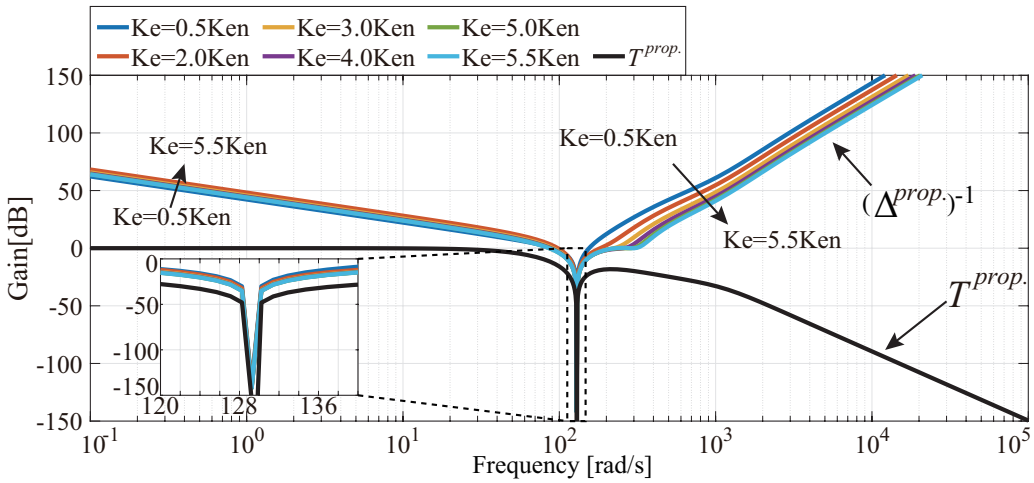


Figure4.17: Bode diagram in terms of $T^{Prop.}(s)$ and $(\Delta^{Prop.}(s))^{-1}$ in proposed method on $K_e$ variation.

Table4.3: Numerical simulation and experimental parameters in proposed load-side torque control.

| | | |
|---|---|---|
| Nominal environmental stiffness | $K_{en}$ | 2592 Nm/rad |
| Measured environmental stiffness | $K_e$ | 186, 2592, 7896 Nm/rad |
| Anti − resonant frequency | $\omega_{ae}$ | 129.23 rad/s |
| Resonant frequency | $\omega_{re}$ | 312.62 rad/s |
| Bandwidth of first − order LVOB | $g_{\omega l}$ | 628 rad/s |
| Bandwidth of FPIDO | $g_{dm}$ | 628 rad/s |
| Bandwidth of PI velocity control | $\omega_n$ | 1000 rad/s |
| Equivalent time constant of Binomial | $\tau_c$ | $4/\omega_{ae}$ |
| Resonance ratio gain of Binomial | $\beta$ | 0.824 |
| Torque proportional gain of Binomial | $K_p$ | 2.493 |
| Torque integral gain of Binomial | $K_i$ | 80.541 |
| Resonance ratio of Binomial (Eq.(4.18)) | $H_r$ | $\sqrt{5}$ |

responses in the proposed load-side torque control. Torque command $\tau_l^{cmd}$ is set to 4.0 Nm. Moreover, another simulation is considered to compare the actual experimental results. In the simulation and experiment, torque command is added at square wave which is maximum and minimum values are 4 Nm and 0.5 Nm. All simulation and experimental parameters in the proposed method are listed in Table4.3.

In the simulation and experiment, control gains are determined in the frequency domain, by binomial design using a stability index $\gamma_i$. Proposed control system is implemented by discretization using zero-order hold at a sampling time of 125 $\mu s$. As discussed previous section, the proposed method is stable even though the environmental stiffness is a higher value, e.g., $K_e = 5.5K_{en}$. Thus, the nominal environmental stiffness is a better setting to $K_e \geq K_{en}$. Environmental stiffness is measured about three environmental blocks, e.g., sponge(AskerC8): $K_{en} = 186$, hard rubber(A65): $K_{en} = 2592$, and aluminum(A5052): $K_{en} = 7896$ Nm/rad. In the first simulation and experiment about $K_e$ variations, actual environmental stiffness are set to 7896 Nm/rad of the aluminum block. In this case, $K_{en}$ is set to $K_{en} = 7896/5.0 = 1579$ and $K_{en} = 7896/5.5 = 1435$. Moreover, extra experiments are confirmed to robustness against $K_e$ variations. In these experiments, relationship of actual and nominal environmental stiffness is assumed to $K_e = 0.014K_{en}$, $K_e = 39.48K_{en}$, and $K_e = 394.8K_{en}$. Nominal environmental stiffness in the case of $K_e = 0.014K_{en}$, $K_e = 39.48K_{en}$, and $K_e = 394.8K_{en}$ is set to $K_{en}$ =13000, 200, 20 Nm/rad, respectively. In second simulation and experiment of all nominal case, to verify the load-side torque response as designed, nominal environmental stiffness is set to $K_{en}$=2592 Nm/rad that measured in advance.

### 4.5.2 Numerical Simulation and Experimental Results

Figs. 4.18 and 4.19 show the numerical simulation and experimental results obtained by the robust stability analysis of the proposed method for different value of $K_e$. In Section 2.4.8, the conventional method is observed to be stable at $K_e = 5.0K_{en}$; however, vibration is observed. Moreover, the conventional method is unstable at $K_e = 5.5K_{en}$ because there is no gain margin, as shown in Section 2.4.5. On the other hand, the proposed method is observed to be stable at both values of $K_e$. In addition, Fig.4.20 shows the experimental results of proposed method in the case of other $K_e$ variations. From these results, even though environmental stiffness variation becomes the variation range from $K_e = 0.014K_{en}$ to $K_e = 394.8K_{en}$, these results show that the proposed method is stable. Therefore, the robustness of the proposed method against $K_e$ variation is higher than that of the conventional

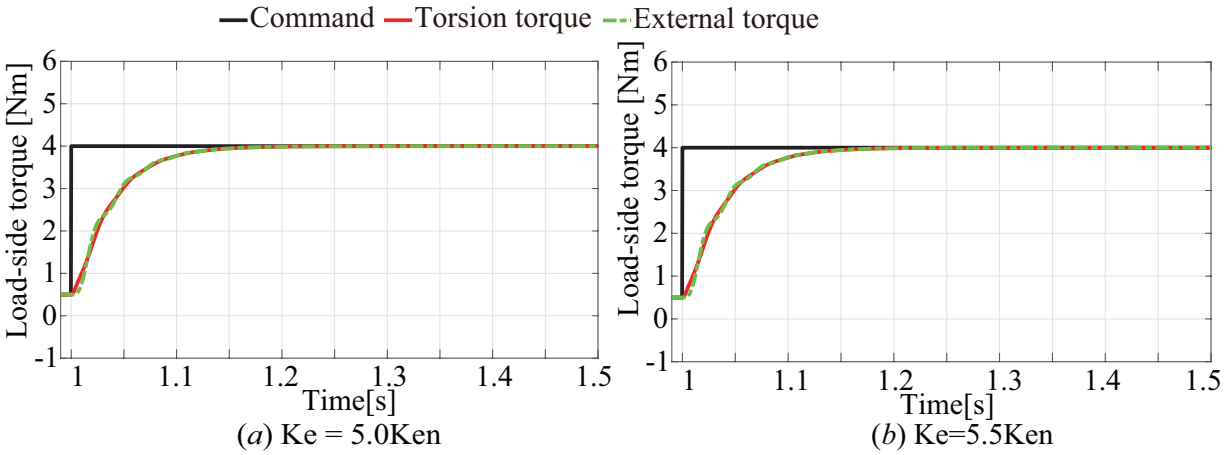


Figure4.18: Simulation results of stability analysis in proposed method. (a) $K_e = 5.0K_{en}$. (b) $K_e = 5.5K_{en}$. Black, red, and green lines are load-side torque command, torsion torque, and external torque, respectively.

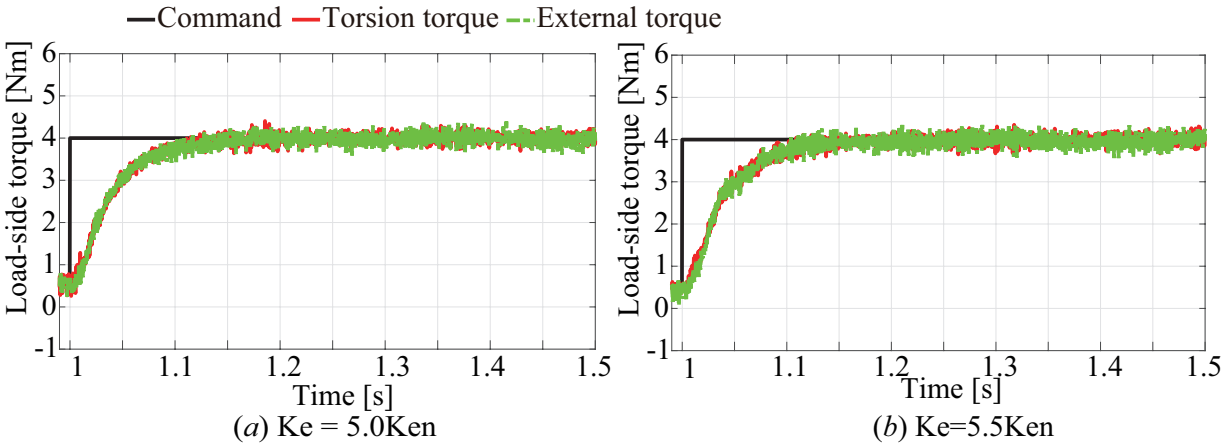


Figure4.19: Experimental results of stability analysis in proposed method. (a) $K_e = 5.0K_{en}$. (b) $K_e = 5.5K_{en}$. Black, red, and green lines are load-side torque command, torsion torque, and external torque, respectively.

method as shown in Table2.1 and Fig.2.18. Furthermore, Figs. 2.19 and 4.21, which respectively present the numerical simulation and experimental results of the conventional and proposed load-side torque controls in case of the binomial design, indicate that smooth load-side torque responses are realized. In addition, the experimental results are the same as the numerical simulation results, as observed in Figs. 4.21 (b) and 4.21 (d) for the proposed method. Thus, this section indicated that the

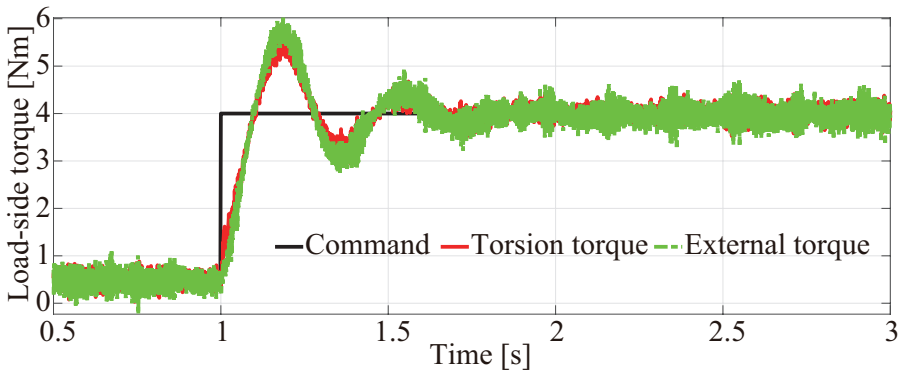


(*a*) Ke=186 (=0.014Ken), Ken=13000

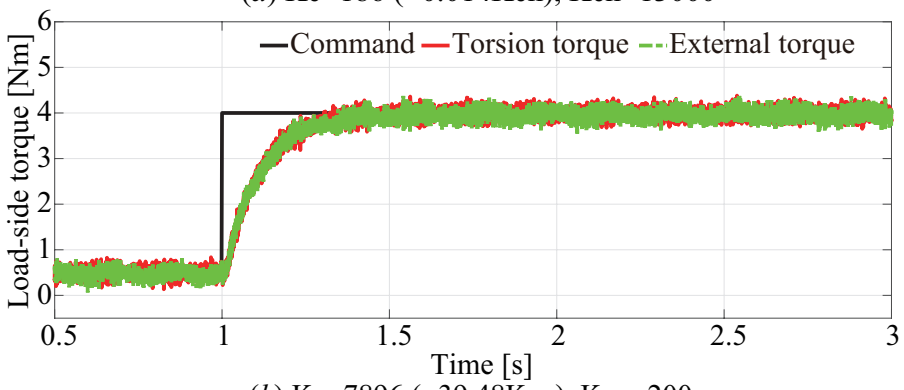


(*b*) Ke=7896 (=39.48Ken), Ken=200

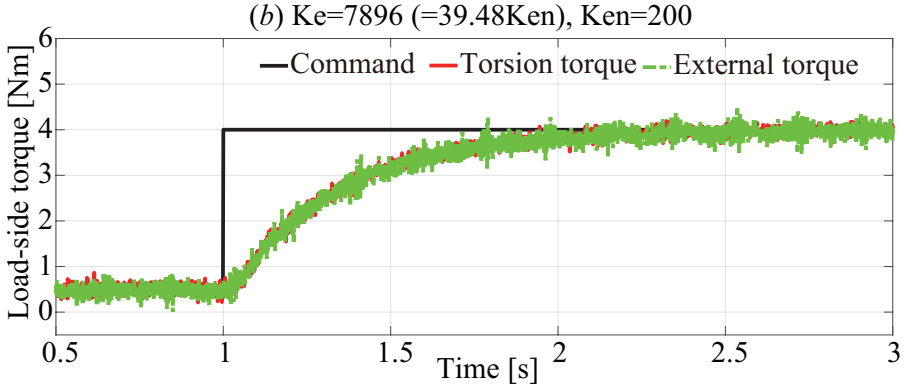


(*c*) Ke=7896(=394.8Ken), Ken=20

Figure4.20: Experimental results of proposed method in case of other $K_e$ variations. (a) $K_e = 0.014K_{en}$. (b) $K_e = 39.48K_{en}$. (c) $K_e = 394.8K_{en}$. Black, red, and green lines are load-side torque command, torsion torque, and external torque, respectively.

proposed load-side torque control have been achieved as designed.

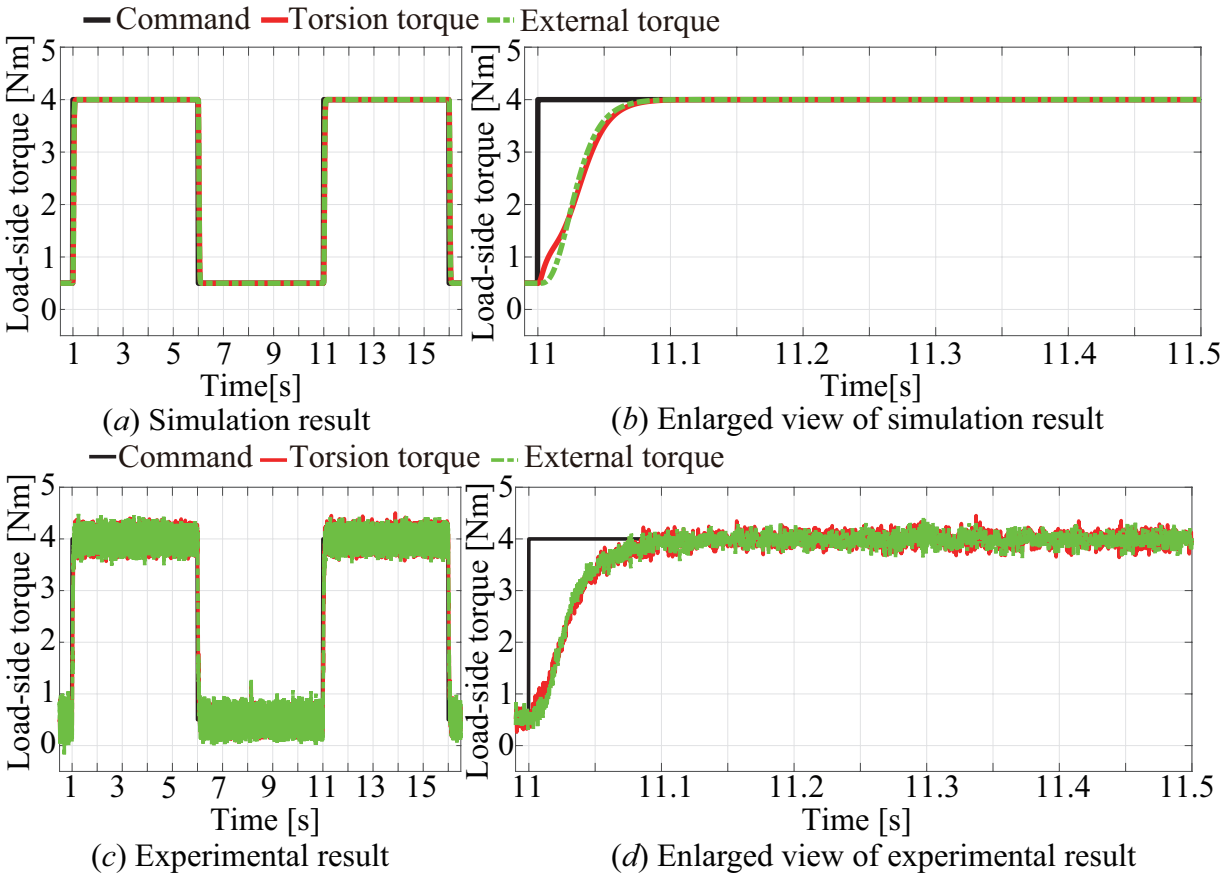


Figure4.21: Numerical simulation and experimental results of load-side torque control based on ERRC (proposed). (a) simulation result. (b) Enlarged view of simulation result. (c) Experimental result. (d) Enlarged view of experimental result. Black, red, and green lines are load-side torque command, torsion torque, and external torque, respectively.

## 4.6 Summary of Chapter4

This chapter proposes the high-robust back-forward drivable torsion torque control based on the ERRC to realize a high-robustness for an environmental stiffness variation ($K_e$ variation). The optimal resonance ratio of the two-inertia system considering the environment in the application of RRC is difficult to determine because it has two resonant frequencies. In addition, the conventional load-side torque control method has an unstable condition in the environmental stiffness variation, e.g., $K_e = 5.5K_{en}$. On the other hand, this chapter focuses on the torque-velocity duality, and a two-

spring system is realized based on a motor-side velocity control. Moreover, an ERRC is proposed using on the motor-side velocity control and first-order LVOB. The results of the analysis performed in the study have demonstrated the toque-velocity duality from the comparison of the two-inertia and two-spring systems, in addition to realizing the high-robust load-side torque control based on an ERRC. Furthermore, this chapter validates that the robustness of the proposed method against $K_e$ variation is higher than that of the conventional method. Thus, the effectiveness of the proposed control method is validated through numerical simulation and experiment.

# Chapter5

# Stable Contact Realization using Force Impulse Based on Back-Forward Drivable Torsion Torque Control

## 5.1 Introduction

In Chapter 3, back-forward drivability is improved by back-forward drivable torsion torque control. In Chapter 4, robust force control against $K_e$ variation is achieved by back-forward drivable torsion torque control based on the ERRC, which is constructed from the two-spring system. However, two control systems are not able to determine the contact velocity for the contacting environment because back-forward drivable torsion torque control has back-forward drivability on the acceleration dimension. Namely, velocity response becomes lamped signal when step torque command is added. To realize the constant velocity motion for contact with the environment, velocity feedback or switching control between velocity and force control systems are normally applied. However, those approaches deteriorate the back-forward drivability on acceleration dimension.

This chapter utilizes the force impulse based on back-forward drivable torsion torque control. The force impulse is related to momentum. Namely, force impulse depends on velocity. Therefore, walking motion stabilization in humanoid and haptic rendering with impact force are realized [102, 103].

Moreover, force control based on momentum is effective to avoid the decoupling and singularity problems [104–106]. To realize stable contact without bouncing, the velocity and acceleration need to be brought to zero after contact with the environment. Thus, the force impulse controller is used instead of force controller. If force impulse is constant, velocity is also constant. Therefore, a stable contact motion at a constant velocity is able to be realized by the force impulse controller. The force impulse controller is constructed based on back-forward drivable torsion torque control and the ERRC. The ERRC is capable of achieving the same resonance ratio i.e., $\sqrt{5}$, similar to the one proposed in position control [72], for a two-inertia system with an environment. Therefore, a force impulse controller based on back-forward drivable torsion torque control using ERRC achieves stable contact motion that suppresses bouncing when in contact with the environment.

This chapter demonstrates three numerical simulations and experiments. In the simulations and experiments, the results of the command response and contact motion are validated in terms of the proposed force impulse regulator based on back-forward drivable torsion torque control. In addition, the result of the load-side torque control, including contact with the environment is verified as an example of application.

## 5.2 Stable Contact Motion using Force Impulse Based on Back-Forward Drivable Torsion Torque Control

### 5.2.1 Control Strategy

This study applies an the ERRC for stable contact realization. A force impulse controller is constructed based on back-forward drivable torsion torque control and ERRC. Back-forward drivable torsion torque controller uses I-P torque controller; thus, I-P torque controller is transformed to force impulse controller by separating integrator. The ERRC is applied in minor loop to improve the robustness against the $K_e$ variation. The force impulse control based on back-forward drivable torsion torque control and the ERRC is designed using the same design approach as the reference [72]. Using

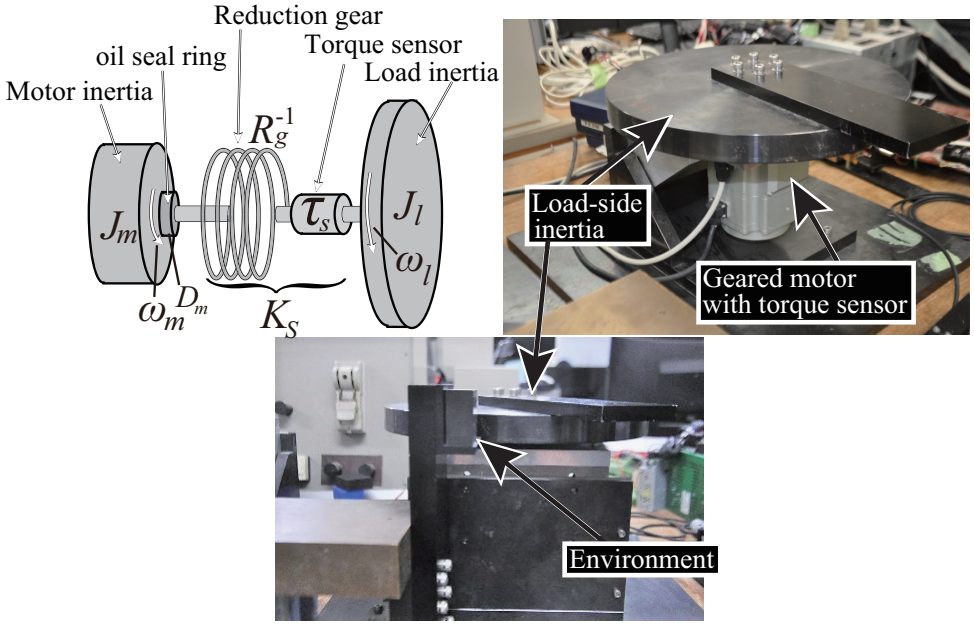


Figure5.1: Experimental equipment.

the force impulse control, a stable contact motion is realized without using a switching controller. In the force impulse control, motor-side velocity control is used to operate the actuator based on the output of the force impulse controller that is outer loop in non-contact phase. By using this, direct teaching operation and approach control are realized. For example, the output of velocity control becomes a constant value when the output of the force impulse controller is of constant value. The force control is used for the realization of stable contact against the environment. The force control is indirectly realized by using force impulse control.

### 5.2.2 Experimental Setup

A strain wave geared motor with a torque sensor [83] that is regarded as one joint of the industrial robot is used. The experimental equipment is shown in Fig.5.1, and it consists of motor inertia, a reduction gear, a torque sensor, and load inertia. The torsion torque sensor has a high bandwidth, and its detection bandwidth is 1 kHz. The bandwidth of the torque sensor is ignored. For the contact motion experiment from free motion, an environmental block is set, as shown on the bottom panel of

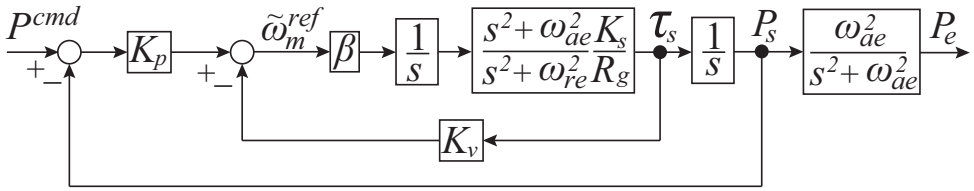


Figure5.2: Block diagram of proposed force impulse control for control design.

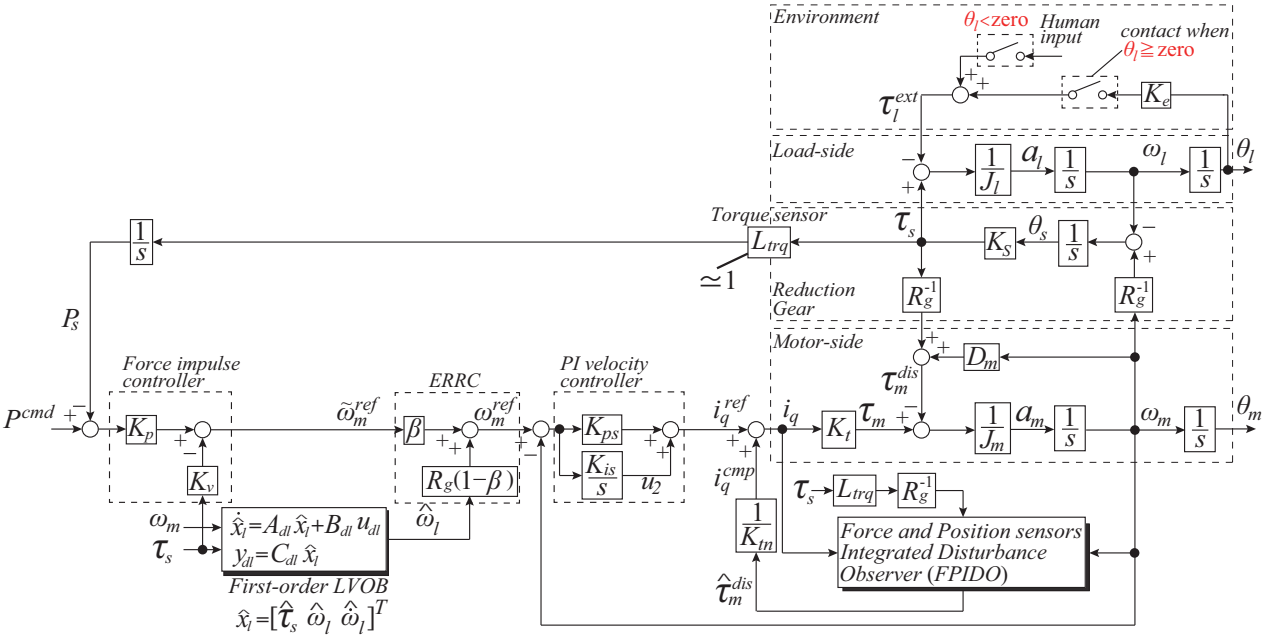


Figure5.3: Overview of proposed force impulse control.

Fig.5.1.

### 5.2.3 ERRC Based on Motor-side Velocity Control and First-order LVOB (proposed)

In this study, the motor-side velocity control and the first-order LVOB are applied for constructing the ERRC. The ERRC is constructed as shown in Fig.4.10 of Chapter 4.

### 5.2.4 Force Impulse Control Based on Back-Forward Drivable Torsion Torque Control (proposed)

This section describes the design of the force impulse control based on back-forward drivable torsion torque control. Proposed force impulse control is constructed using the ERRC and torsion torque feedback. The force impulse control is used to realize the stable contact and direct teaching for polishing motion. Force impulse control realizes approach motion for the environment or direct teaching operation in case of non-contact with environment. Force impulse control is capable of stable contact motion for the environment when contacting with the environment. Pushing motion that needs force control is indirectly realized by using force impulse control. To design the control gains, the force impulse control system for control design is shown in Fig.5.2. The transfer function from the force impulse command $P^{cmd}$ to torsion force impulse response $P_s$ is derived as

$$G_{ps}(s) = \frac{P_s}{P^{cmd}} = \frac{N_{um}^{prop.}(s)}{D_{en}^{prop.}(s)} \tag{5.1}$$

$$N_{um}^{prop.}(s) = (s^2 + \omega_{ae}^2)\beta\frac{K_s}{R_g}K_p \tag{5.2}$$

$$\begin{aligned} D_{en}^{prop.}(s) &= s^4 + \beta\frac{K_s}{R_g}K_v s^3 + (\omega_{re}^2 + \beta\frac{K_s}{R_g}K_p)s^2 \\ &\quad + \beta\frac{K_s}{R_g}K_v\omega_{ae}^2 s + \beta\frac{K_s}{R_g}K_p\omega_{ae}^2 \\ &= (s^2 + 2\zeta_1\omega_1 s + \omega_1^2)(s^2 + 2\zeta_2\omega_2 s + \omega_2^2) \\ &= s^4 + 2(\zeta_1\omega_1 + \zeta_2\omega_2)s^3 \\ &\quad + (\omega_1^2 + \omega_2^2 + 4\zeta_1\zeta_2\omega_1\omega_2)s^2 \\ &\quad + 2\omega_1\omega_2(\zeta_1\omega_2 + \zeta_2\omega_1)s + \omega_1^2\omega_2^2. \end{aligned} \tag{5.3, 5.4}$$

Compared with (5.3) and (5.4), the control gains are designed by the pole placement method as follows:

$$\beta = \frac{4K_{en}}{K_{sn}} \tag{5.5}$$

$$K_p = \frac{\omega_{ae}^2}{\beta}\frac{R_g}{K_{sn}} = \frac{R_g}{4K_{en}}\omega_{ae}^2 = \frac{R_g}{4J_{ln}} \tag{5.6}$$

$$K_v = \frac{4\omega_{ae}}{\beta}\frac{R_g}{K_{sn}} = \frac{R_g}{K_{en}}\omega_{ae} = \frac{R_g}{K_{en}}\sqrt{\frac{K_{en}}{J_{ln}}}, \tag{5.7}$$

where, the control bandwidths $\omega_1$, $\omega_2$ and the damping coefficients $\zeta_1$, $\zeta_2$ are set to $\omega_1 = \omega_2 = \omega_{ae}$ and $\zeta_1 = \zeta_2 = 1.0$. This control design is a quadruple-root design. Finally, the transfer function from the force impulse command $P^{cmd}$ to the external force impulse $P_e$ is given inserting (5.5)–(5.7) to (5.1), as follows:

$$G_{pe}(s) = \frac{P_e}{P^{cmd}} = \frac{(s^2 + \omega_{ae}^2)\omega_{ae}^2}{(s + \omega_{ae})^4} \frac{\omega_{ae}^2}{s^2 + \omega_{ae}^2} = \frac{\omega_{ae}^4}{(s + \omega_{ae})^4}. \tag{5.8}$$

In (5.8), the transfer function is expressed as the fourth-order low pass filter. Therefore, the smooth external force impulse response is realized. The resonance ratio $H$ is calculated from (5.5) as follows:

$$H = \frac{\omega_{re}}{\omega_{ae}} = \frac{\sqrt{\frac{K_e + \beta K_s}{J_l}}}{\sqrt{\frac{K_e}{J_l}}} = \frac{\sqrt{\frac{K_e + \frac{4K_e}{K_s} K_s}{J_l}}}{\sqrt{\frac{K_e}{J_l}}} = \sqrt{5}. \tag{5.9}$$

From (5.9), the resonance ratio is determined as $\sqrt{5}$. Therefore, the resonance ratio in the two-spring system is the same as that given in reference [72]. An overview of the force impulse control system is shown in Fig.5.3. In Fig.5.3, the FPIDO is used to improve the disturbance suppression performance against the motor-side disturbance. The first-order LVOB estimates the load-side velocity for constructing the ERRC.

## 5.3 Simulation and Experiment

### 5.3.1 Numerical Simulation and Experimental Conditions

Herein, this section reports on simulations and experiments in terms of the force impulse control. Fig.5.4 shows the concept figure of three scenarios in numerical simulation and experiments. In the first scenario of Fig.5.4 (a), the command response of the force impulse control based on the ERRC is confirmed. The force impulse command is set to 0.2 Nms to compare it with the experimental results. The torsion torque is measured using the torsion torque sensor. The external torque is estimated by a LTOB (see Section 2.3.3). The torsion force impulse and the external force impulse are calculated using the integrator from the torsion torque and the estimated external torque.

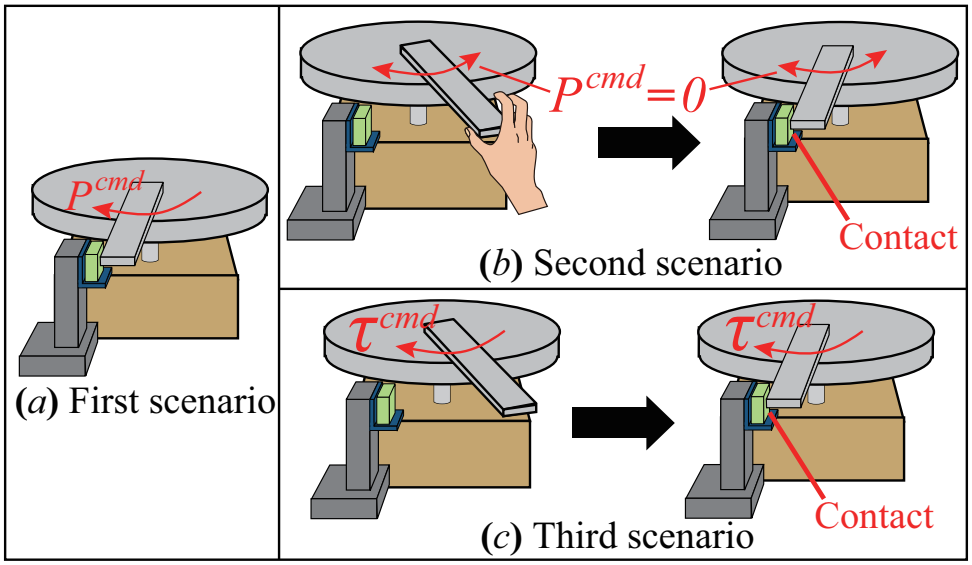


Figure5.4: Concept figure of numerical simulation and experimental scenarios.

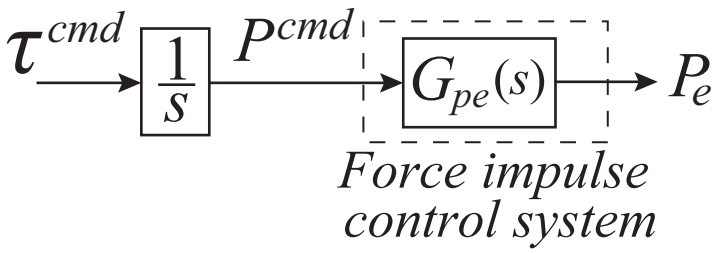


Figure5.5: Block diagram of load-side torque control using force impulse control of Fig.5.3.

In the second scenario of Fig.5.4 (b), this paper confirms the contact motion from free motion. This paper assumes contact with the environment during free motion, e.g., a contact motion with the environment in the direct teaching motion. The external torque is added and the free motion continues until contact is made with the environment. Then, the force impulse command $P^{cmd}$ is set to zero in the force impulse control as shown in Fig.5.3.

As an example of the application, this paper finally considers load-side torque control including contact for the environment using the force impulse control, as shown in Fig.5.4 (c). Then, the force impulse command is calculated as the ramp command $P^{cmd} = \tau^{cmd}/s$, as shown in Fig.5.5. The torque command $\tau^{cmd}$ is set to 1 Nm until contact is established with the environment. After that, the

Table5.1: Numerical simulation and experimental parameters for proposed force impulse control.

| | | |
|---|---|---|
| Torque constant | $K_{tn}$ | 0.49 Nm/A |
| Motor − side inertia | $J_{mn}$ | $1.44 \times 10^{-4}$ kgm$^2$ |
| Motor viscosity coefficient | $D_{mn}$ | $9.80 \times 10^{-4}$ Nms/rad |
| Load − side inertia | $J_{ln}$ | 0.16 kgm$^2$ |
| Torsion spring constant | $K_{sn}$ | $1.26 \times 10^4$ Nm/rad |
| Gear ratio | $R_g$ | 50.0 |
| Nominal environmental stiffness | $K_{en}$ | 2592 Nm/rad |
| Anti − resonant frequency | $\omega_{ae}$ | 129.23 rad/s |
| Resonant frequency of plant | $\omega_{re}^{Plant}$ | 312.62 rad/s |
| Resonant frequency with ERRC | $\omega_{re}^{ERRC}$ | 288.97 rad/s |
| Bandwidth of first − order LVOB | $g_{\omega l}$ | 628 rad/s |
| Bandwidth of FPIDO | $g_{dm}$ | 628 rad/s |
| Bandwidth of torque sensor | $g_{trq}$ | 6280 rad/s |
| Control bandwidth of force impulse control | $\omega_1 = \omega_2$ | $\omega_{ae}$ rad/s |
| Damping coefficient | $\zeta_1 = \zeta_2$ | 1.0 |
| Equivalent resonance ratio gain | $\beta$ | 0.824 |
| Force impulse differential gain | $K_v$ | 2.493 |
| Force impulse proportional gain | $K_p$ | 80.54 |
| Resonance ratio | $H$ | $\sqrt{5}$ |
| Bandwidth of PI velocity control | $\omega_n$ | 1000 rad/s |

torque command is set to 2 Nm. The numerical simulation and experimental parameters are listed in Table5.1.

### 5.3.2 Numerical Simulation Results of Force Impulse Control

Fig.5.6 shows the simulation results for the force impulse control based on ERRC. In Fig.5.6, the force impulse response follows the force impulse command smoothly. Moreover, the load-side torque is regulated to the pulse response according to the force impulse responses.

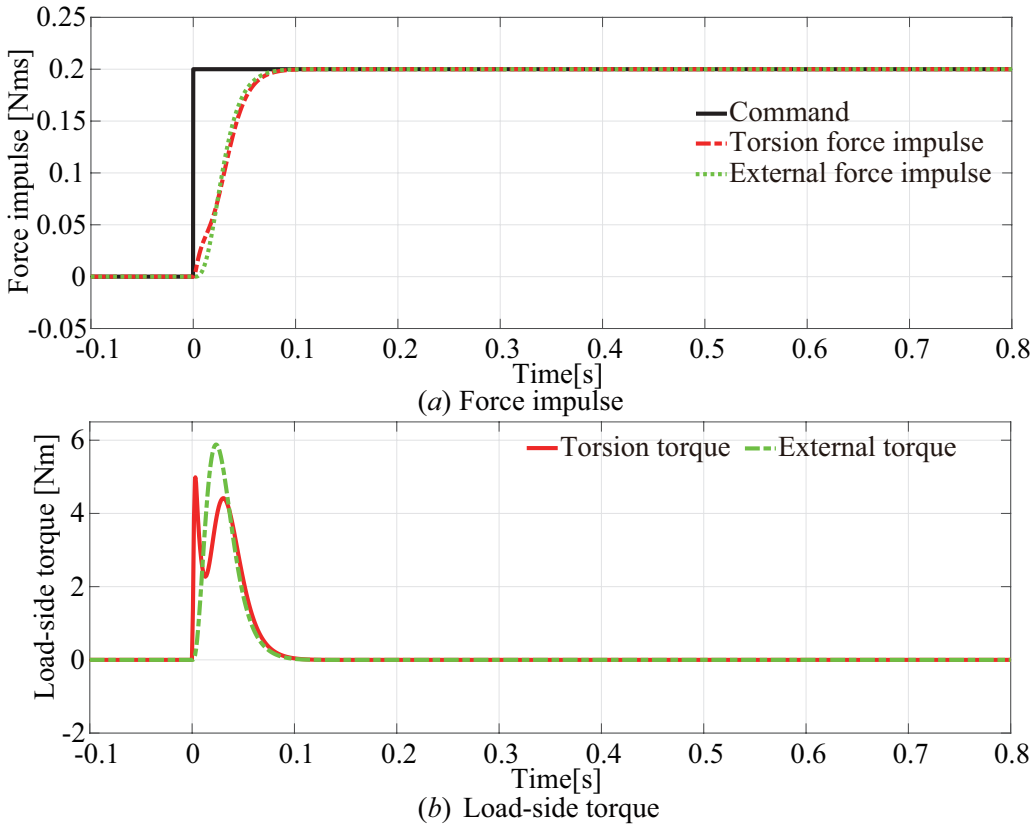


Figure5.6: Simulation results of proposed force impulse control. (a) Force impulse (b) Load-side torque.

Fig.5.7 shows the simulation results of contact motion from free motion. As shown in Fig.5.7, the force impulse response has an offset when the external torque is added during free motion; this occurs because the system does not account for environmental dynamics. Thus, constant-velocity motion is achieved after adding a pulse-like input in free motion because the force impulse corresponds to the velocity. After contact with the environment is established, the environmental dynamics are included and the force impulse response follows the force impulse command smoothly to zero. Therefore, the force impulse control achieves a stable contact motion after making contact with the environment.

### 5.3.3 Experimental Results of Force Impulse Control

Fig.5.8 shows the experimental results for force impulse control. The force impulse response in Fig.5.8 follows the force impulse command similar to that shown in Fig.5.6. Moreover, the estimated

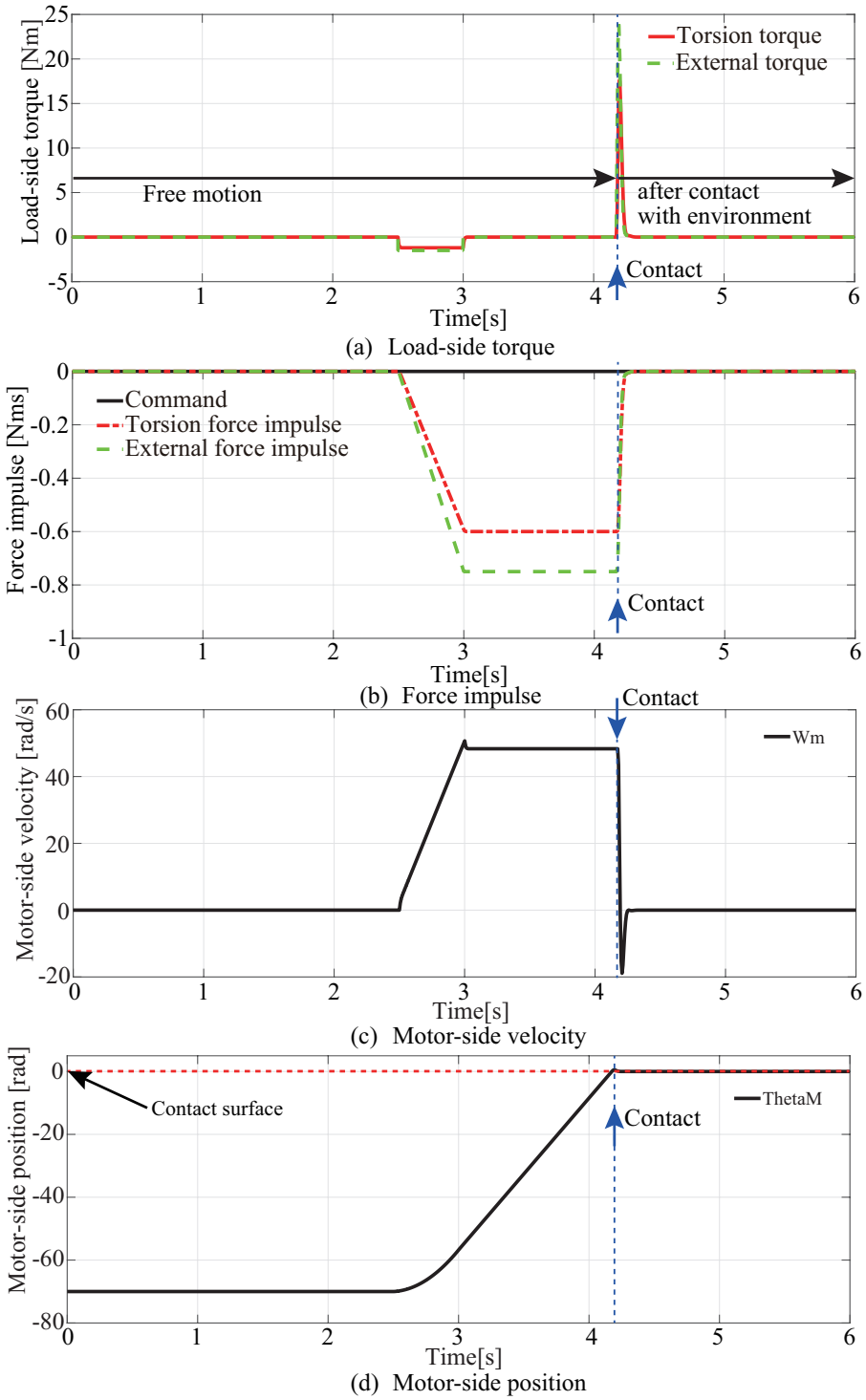


Figure5.7: Simulation results of contact motion using proposed method. (a) Load-side torque. (b) Force Impulse. (c) Motor-side velocity. (d) Motor-side position.

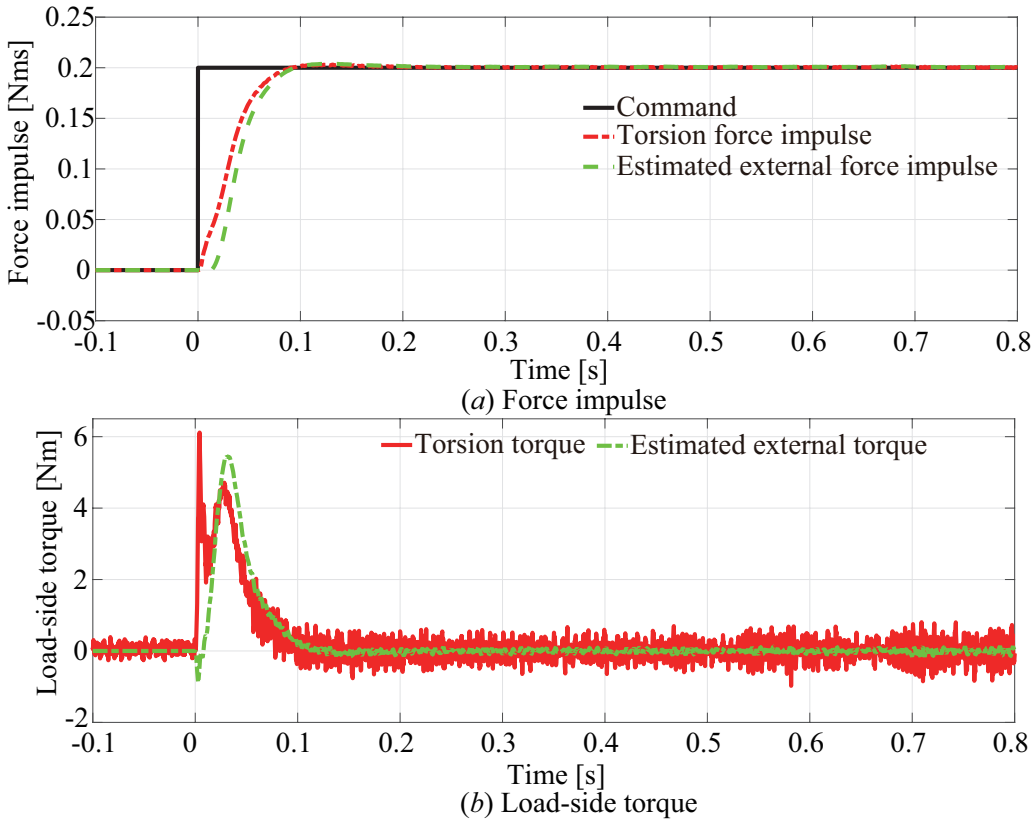


Figure5.8: Experimental results of proposed force impulse control. (a) Force impulse (b) Load-side torque.

external torque has occurred a negative response at zero seconds. This is because of the load-side inertia and torsion stiffness variations.

Fig.5.9 shows the experimental results for the contact motion from free motion. Not only force impulse response but also motor-side velocity become constant value after adding the pulse-like external torque by human hands at 2.5 s to 3 s. This is because that force impulse control in case of not contacting with environment satisfies the Newton's law, i.e., $\tau = Ja$, not including spring and damper. Here, bode diagram of load-side input characteristics, $a_l/\tau_l^{ext}$, in non-contact with environment is shown in Fig.5.10.

From Fig.5.10, load-side input characteristics, $a_l/\tau_l^{ext}$ indicate the constant in low-frequency range, i.e., $\tau = Ja$, is satisfied. Thus, direct teaching operation is realized. Force impulse and motor-side velocity responses convergent to zero after contact with environment at 4 s. This means that the actu-

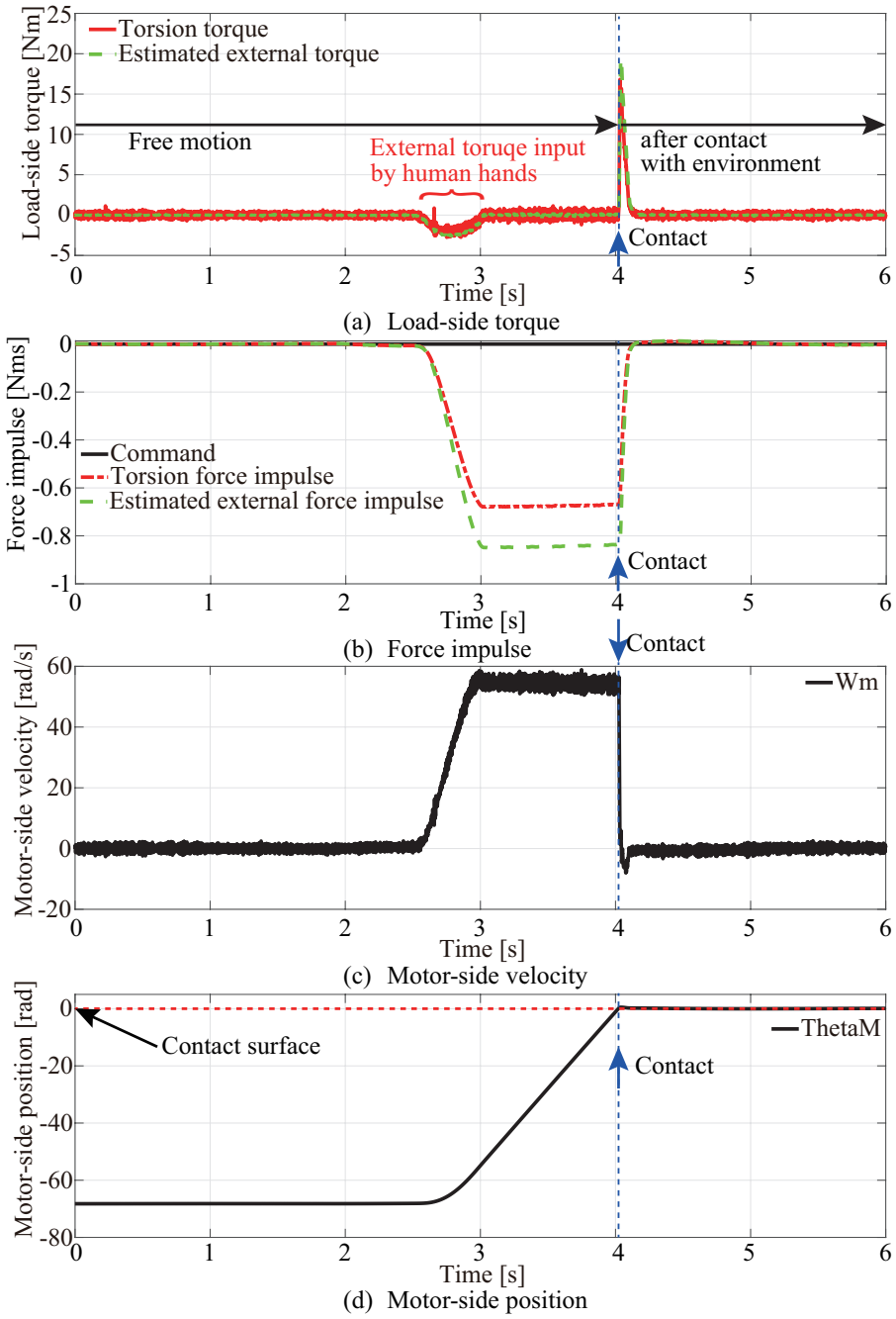


Figure5.9: Experimental results of contact motion using proposed method. (a) Load-side torque. (b) Force Impulse. (c) Motor-side velocity. (d) Motor-side position.

ator stopped after contact with environment. From Fig.5.9, the stable contact motion using the force impulse control is also achieved experimentally. The proposed force impulse control realizes the stable contact and teaching operations for polishing motion under direct teaching, and the effectiveness

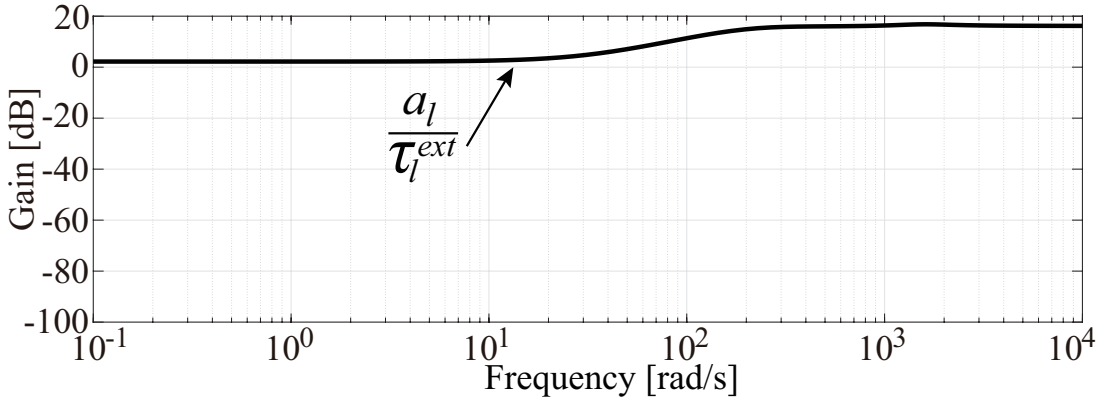


Figure5.10: Bode diagram of load-side input characteristics: $a_l/\tau_l^{ext}$ in terms of proposed force impulse control in case of non-contact with environment.

of the force impulse control is validated. However, the overshoot of the motor-side velocity occurred at 4 s is smaller than in the simulation. This is caused owing to the environmental viscosity.

### 5.3.4 Simulation and Experimental Results of Load-side Torque Control using Force Impulse Control

Finally, the load-side torque control is verified using the proposed force impulse control as an example of the application. Fig.5.11 shows the simulation results for the load-side torque control with contact motion. From Fig.5.11, the actuator makes contact with the environment at around 0.5 s. Then, the impact torque occurs, but the load-side torque response smoothly follows the load-side torque command after making contact with the environment. Furthermore, the force impulse responses also follow the force impulse command calculated from the torque command.

Fig.5.12 shows the experimental results for the load-side torque control including contact, obtained using force impulse control. Similar to the simulation results in Fig.5.11, the load-side torque response follows the load-side torque command smoothly after making contact with the environment. Based on these results, it is able to be concluded that the force impulse control achieves stable contact motion. Moreover, it also achieves human-robot interaction, such as direct teaching for polishing motions.

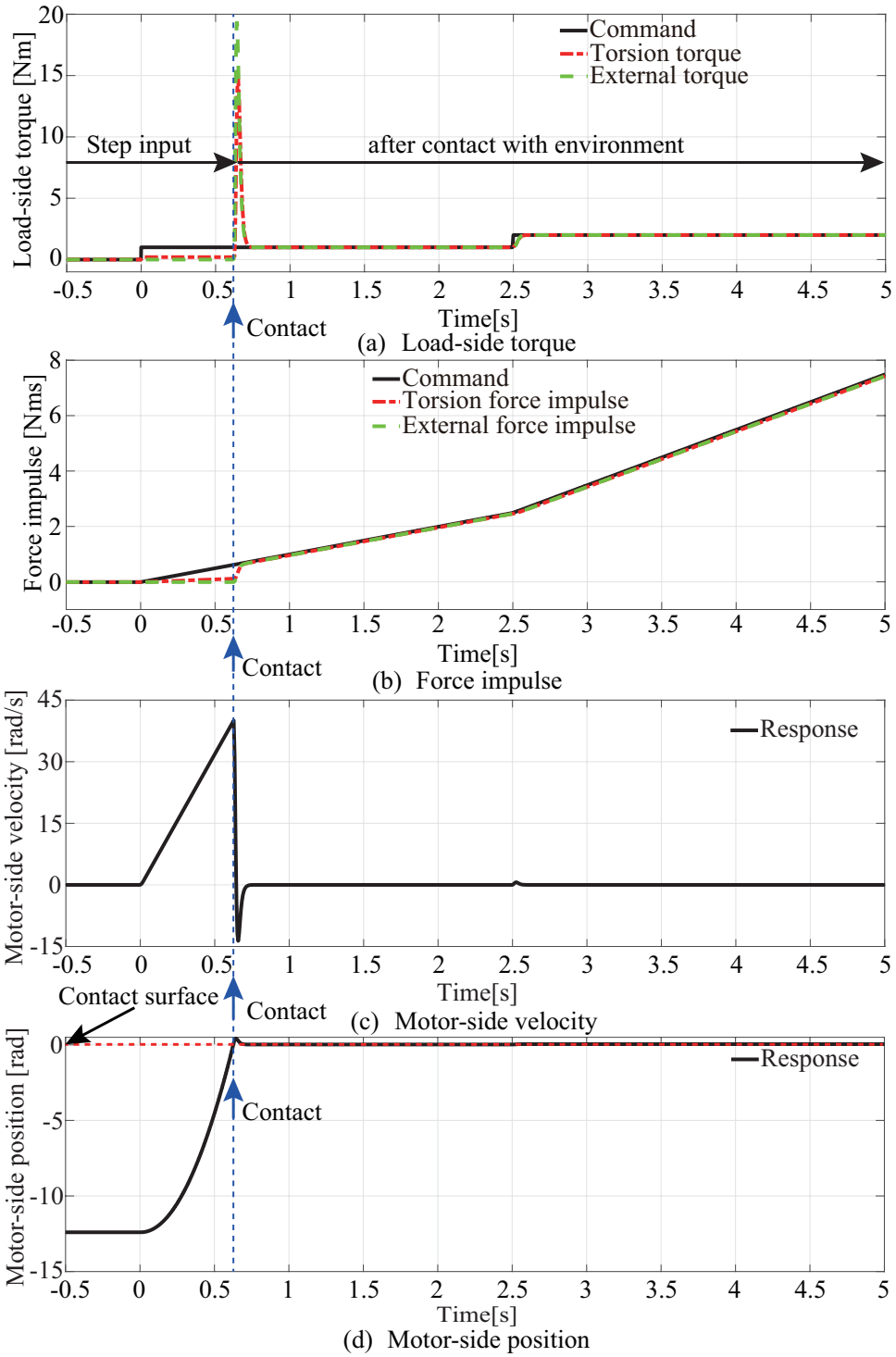


Figure5.11: Simulation results of load-side torque control including contact using proposed method. (a) Force impulse (b) Load-side torque. (c) Motor-side velocity. (d) Motor-side position.

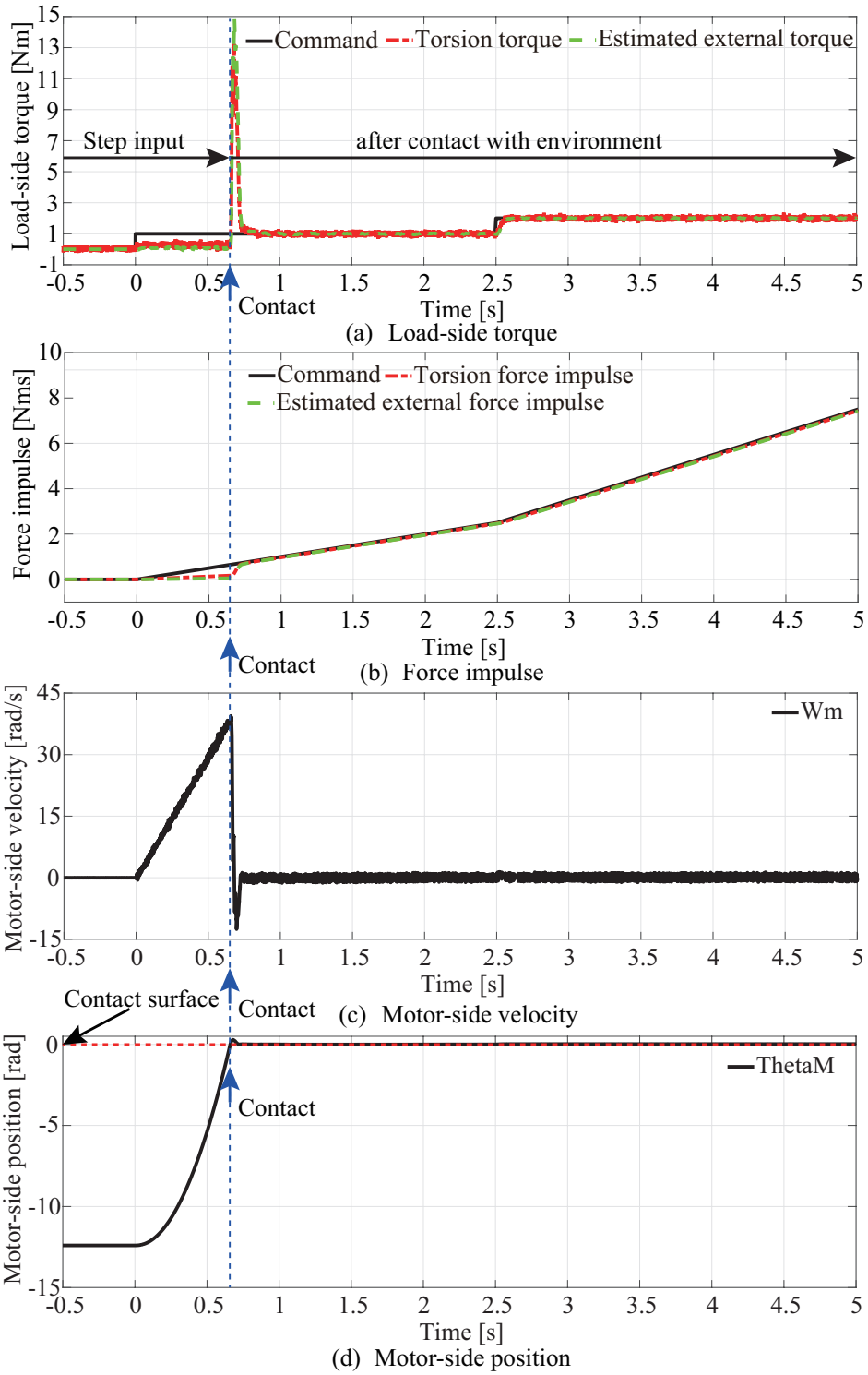


Figure5.12: Experimental results of load-side torque control including contact using proposed method. (a) Force impulse (b) Load-side torque. (c) Motor-side velocity. (d) Motor-side position.

## 5.4 Summary of Chapter5

This chapter proposes force impulse control based on back-forward drivable torsion torque control and ERRC for stable contact realization from free motion. The proposed force impulse control is constructed using a motor-side velocity control, first-order load-side velocity observer (First-order LVOB), and force impulse controller that is transformed from I-P torsion torque controller. The proposed method allows for the realization of stable contact motion by regulating the force impulse. Moreover, this study considers the load-side torque control as an example of the application. As a result, the good results in terms of the load-side torque control are also verified. The effectiveness of the proposed method is verified by numerical simulations and experiments.

# Chapter6

# Conclusions

## 6.1 Summary of Dissertation

Recently, the aging population is increasing, besides, the worker population is decreasing. For such problems, to improve the quality of life, demands of the human support system are increasing in industrial as well as non-industrial fields. In the dissertation, the research objective is to realize the stable human-robot interaction control that satisfies back drivability, the robustness of environmental stiffness variation, and stable contact. The stable environment interaction that satisfies the above issues is achieved by the back-forward drivable torsion torque control in the dissertation.

The contribution of the dissertation is summarized as follows.

Chapter 1 describes the issues for stable environment interaction and discusses the environmental interaction control for solving each issue.

Chapter 2 discusses force control for environment interaction and its issues. First, this chapter introduces acceleration-based force control. The acceleration-based force control is able to achieve ideal back drivability in the single-inertia system. In addition, the acceleration-based force control is also able to achieve the ideal back drivability in the two-inertia system. However, vibration has occurred and human-robot interaction performance is reduced. Moreover, the definition of back drivability in the two-inertia system the characteristics from the load side to the actuator side. In case of evaluat-

ing human-robot interaction in a two-inertia system, evaluation of the characteristics from load-side input to load side output, i.e., $a_l/\tau_l^{ext}$ is easy to understand, intuitively. Thus, this characteristic is defined as back-forward drivability. For this issue, the need for realizing both vibration suppression and back-forward drivability is described. Moreover, it is necessary to consider the environmental dynamics for stable force control design. Conventionally, force control based on RRC is proposed for environment interaction. In this force control system, the open-loop analysis indicated that there is an unstable condition against $K_e$ variation. For this, ensuring high-robustness of $K_e$ is also needed. Finally, stable contact realization discussed that velocity and acceleration need to be brought to zero after contact with the environment.

Chapter 3 described proposed high back-forward drivable torsion torque control focusing on back-forward drivability for human interaction. Proposed back-forward drivable control achieve vibration suppression while maintaining back-forward drivability. As a result, smooth human-robot interaction is realized and the effectiveness of the proposed approach is validated.

Chapter 4 described proposed high-robust force control based on back-forward drivable torsion torque control using ERRC against the environmental stiffness variation. ERRC is constructed based on motor-side velocity control and first-order LVOB. ERRC is a similar structure compared to the RRC of position/velocity controls. Therefore, the same control approaches proposed in position/velocity controls are also able to be applied based on the torque-velocity duality for force control design. In robust stability analysis, the proposed load-side torque control show that it is robust against the environmental stiffness variation. High-robust back-forward drivable torsion torque control using ERRC is realized by considering environmental dynamics.

Chapter 5 described proposed stable contact control based on force impulse control. The force impulse controller is transformed form I-P torque controller in the back-forward drivable torsion torque control, as indicated in Chapter 3. The ERRC is constructed based on the two-spring system focusing on the torque-velocity duality and is applied to improve the robustness against environmental stiffness variation, as indicated in Chapter 4. To achieve a stable contact motion without bouncing phenom-

ena, the velocity and acceleration need to be brought to zero after contact with the environment. Force impulse is dependent on velocity; therefore, velocity is also regulated to zero by regulating force impulse to zero. Force impulse control is constructed based on the back-forward drivable torsion torque control and the ERRC.

The results show that not only back-forward drivability is ensured is demonstrated, but also force impulse control is robust against the environmental stiffness variation. The high-performance environment interaction control, which realizes both back drivable and stable contact motion, was achieved based on force impulse control.

## 6.2 Future Tasks

This thesis has demonstrated new force control approach that satisfies some issues, back drivability, robustness of $K_e$, and stable contact, for improving environment interaction performance. Force control is designed focusing on torque-velocity duality in the geared actuator with torsion torque sensor. To expand proposed approach, there are some issues.

- Implementation to manipulator.
- Relationship between back-forward drivability and stable contact.
- Comparison of proposed control using other load-side sensors

In Chapters 4 and 5 of this thesis, the proposed method has considered environmental dynamics. Moreover, the control system is assumed as one joint model in the manipulator. To implement the proposed method to the manipulator, it is necessary to examine the dynamic influence on each axis. Dynamic force affects the control performance; thus, dynamic influence will be compensated using the dynamic equation or DOB scheme.

Chapter 3 has demonstrated proposed back-forward drivable torsion torque control for improving back-forward drivability. Ideal back-forward drivability is almost realized by the proposed method, but stable contact is not realized. On the other hand, chapter 5 has demonstrated the stable contact

motion using force impulse control based on back-forward drivable torsion torque control. In this proposed method, back-forward drivability in low-frequency range is lower than the proposed method of Chapter 3. From these results, trade-off relationship between back-forward drivability and stable contact realization is considered. Thus, control design will be considered to realize more high back-forward drivability and stable contact for high-performance environment interaction.

This thesis utilizes a geared actuator with a torsion torque sensor, which is assumed as one joint model of the manipulator. The proposed methods in this thesis are constructed using torsion torque feedback. To expand for general equipment, the proposed control design using other load-side sensors needs to be considered.

# A

# Analysis of High Back-Forward Drivable Control System, Including Sensor and Control dynamics

## A.1 Comparison of Back-Forward Drivability for Proposed and Conventional Back-Forward Drivable Control Systems Considering Bandwidth of Torsion Torque Sensor

This section indicates the Bode diagram in app. Fig. A.1 for the proposed and conventional back-forward drivable control systems considering bandwidth of the torsion torque sensor. In this analysis, the dynamics of the torsion torque sensor is expressed as a 1st-order LPF that is set to 1 kHz, i.e., 6280 rad/s.

From app. Fig. A.1 it is clear that, even though the torsion torque sensor is considered in the conventional and proposed methods, it does not affect the back-forward drivability of either method. Thus, the bandwidth of the torsion torque sensor $g_{trq}$ is able to be ignored in this study.

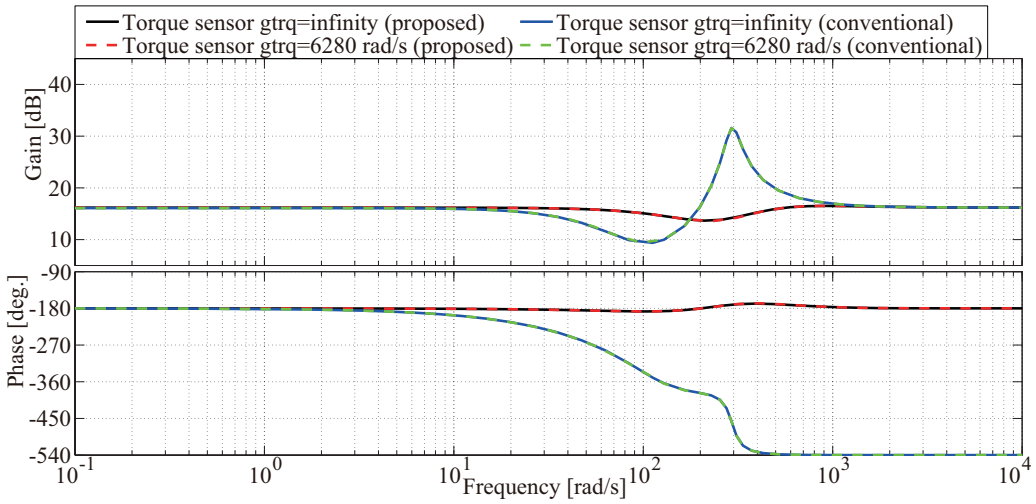


FigureA.1: Bode diagram of back-forward drivability in terms of proposed and conventional back-forward drivable control systems considering the bandwidth of torsion torque sensor.

## A.2 Comparison of PID type TTC and I-P+$\omega_s$ Feedback type TTC

This section describes the difference between PID type TTC and the proposed TTC. Moreover, this paper assumes that friction is compensated and sensor and observer estimation values are the same as the actual values. The transfer function of the TTC designed in this paper is given from (3.12)–(3.21). Next, the transfer function of the PID type TTC is derived as

$$\frac{\tau_s}{\tau_s^{ref}} = \frac{\frac{K_s K_t}{J_m R_g}\left(K_d s^2 + K_p s + K_i\right)}{s^3 + \frac{K_s K_t K_d}{J_m R_g} s^2 + \left\{\frac{K_s K_t K_p}{J_m R_g} + \left(\frac{K_s}{J_m R_g^2} + \frac{K_s}{J_l}\right)\right\} s + \frac{K_s K_t K_i}{J_m R_g}}. \tag{A.1}$$

Equations (3.12) and (A.1) are 3rd-order transfer functions. These equations do not include the observer dynamics of the VDO or pseudo differentiator. However, the actual system has observer dynamics or differentiator about feedback gains. Thus, this paper analyzes the block diagrams of the two type TTCs as shown in app.Fig. A.2 and app.Fig. A.3. From app. Fig. A.2, the transfer function of PID type TTC is derived as

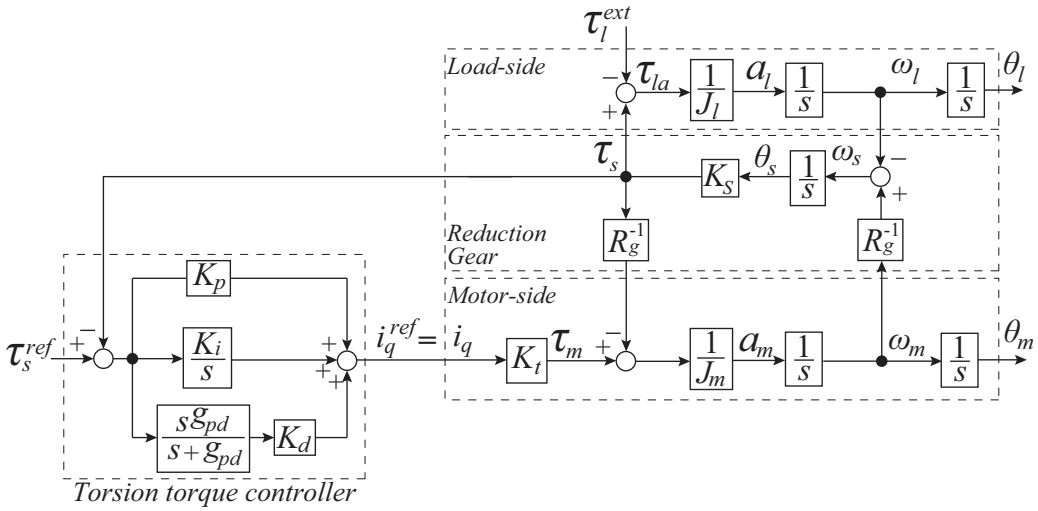


FigureA.2: Block diagram of PID type TTC.

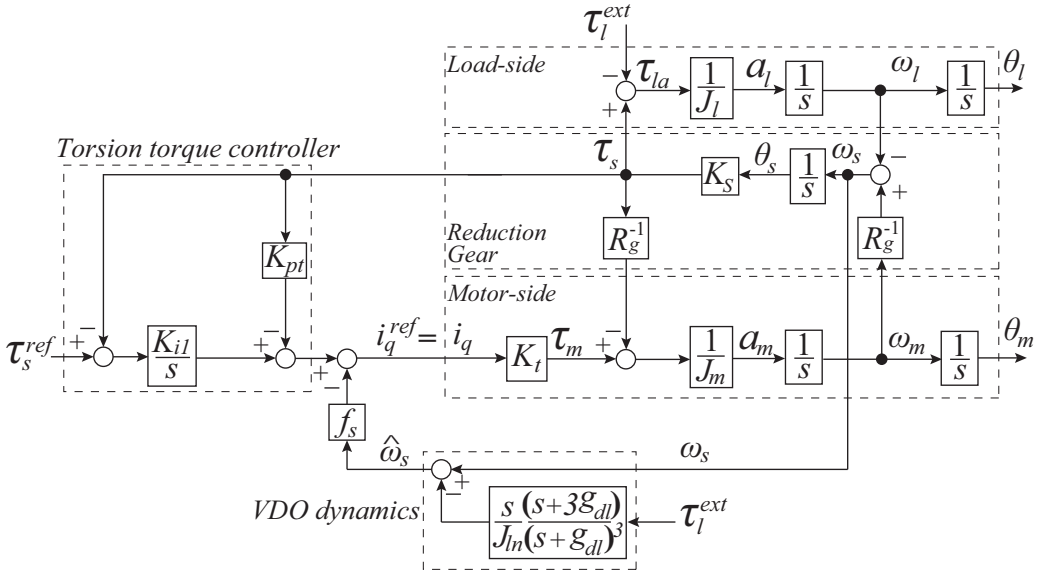


FigureA.3: Block diagram of I-P+$\omega_s$ feedback type TTC.

$$\frac{\tau_s}{\tau_s^{ref}} = \frac{\frac{K_s K_t}{J_m R_g}\Big\{(K_d g_{pd} + K_p)s^2 + (K_p g_{pd} + K_i)s + K_i g_{pd}\Big\}}{D_{en}^{PID}(s)} \tag{A.2}$$

$$\begin{aligned} D_{en}^{PID}(s) = s^4 + g_{pd}s^3 + \Big\{ & \frac{K_s K_t K_p}{J_m R_g} + \frac{K_s K_t K_d g_{pd}}{J_m R_g} \\ & + K_s\Big(\frac{1}{J_m R_g^2} + \frac{1}{J_l}\Big)\Big\}s^2 + \Big\{\frac{K_s K_t K_p g_{pd}}{J_m R_g} + \frac{K_s K_t K_i}{J_m R_g} \\ & + g_{pd} K_s\Big(\frac{1}{J_m R_g^2} + \frac{1}{J_l}\Big)\Big\}s + \frac{K_s K_t K_i g_{pd}}{J_m R_g} \end{aligned} \tag{A.3}$$

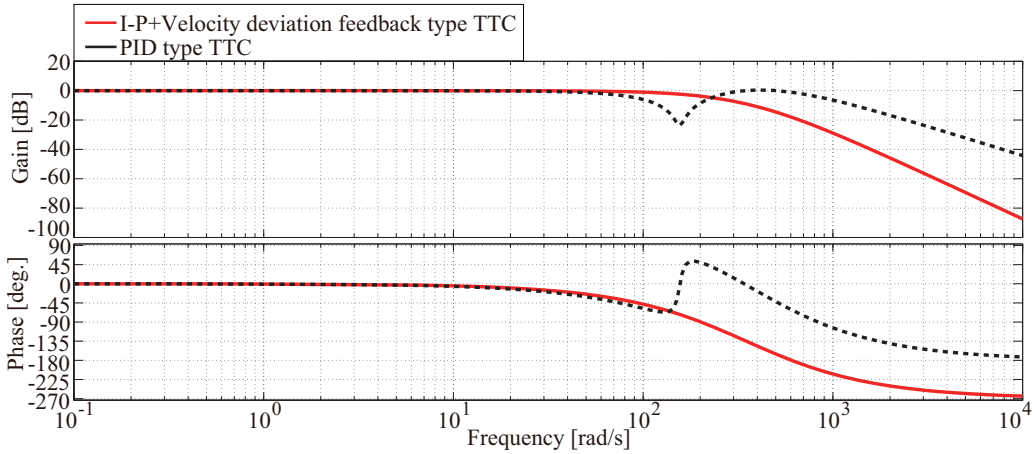


FigureA.4: Bode diagram of I-P+$\omega_s$ feedback type TTC and PID type TTC.

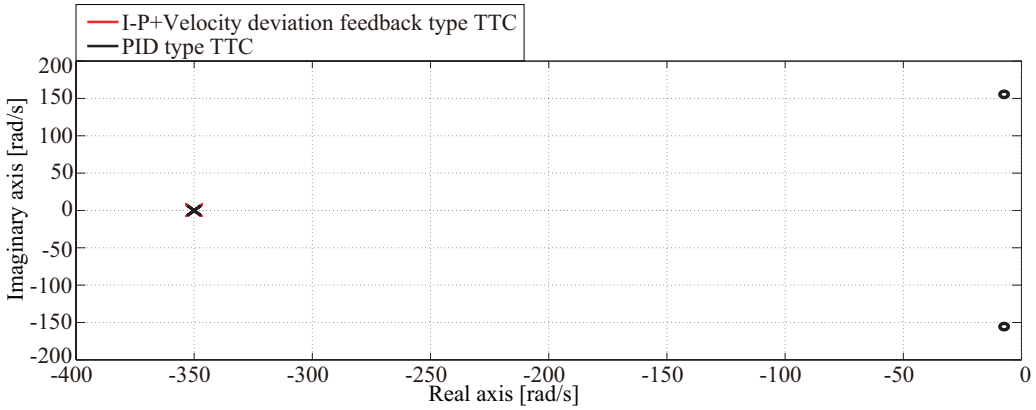


FigureA.5: Pole-zero assignment of I-P+$\omega_s$ feedback type TTC and PID type TTC.

In app. Fig. A.3, the velocity deviation estimation of the VDO is expressed as

$$\hat{\omega}_s = \omega_s - \frac{s}{J_{ln}} \frac{s + 3g_{dl}}{(s + g_{dl})^3} \tau_l^{ext}. \tag{A.4}$$

From (A.4), the estimated velocity deviation $\hat{\omega}_s$ is same as the actual velocity deviation $\omega_s$. Here, the external torque is not considered. Thus, the transfer function from torsion torque reference $\tau_s^{ref}$ to torsion torque $\tau_s$ in terms of app. Fig. A.3 is similar to (3.12). Next, the transfer functions in (3.12), (A.1), and (A.2) are compared. In (3.12) and (A.1), the two type TTCs have the same denominator after applying the pole placement method. However, the difference between the two type TTCs (PID, I-P+$\omega_s$ feedback) is the transfer function of the control system. Actually, it is necessary to use the differentiator for torque differential gain $K_d$ of PID type TTC, but the actual PID type TTC uses a

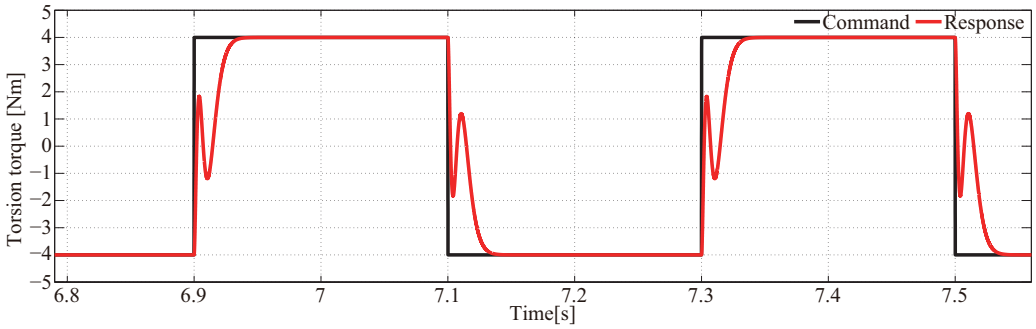


FigureA.6: Simulation result of PID type TTC.

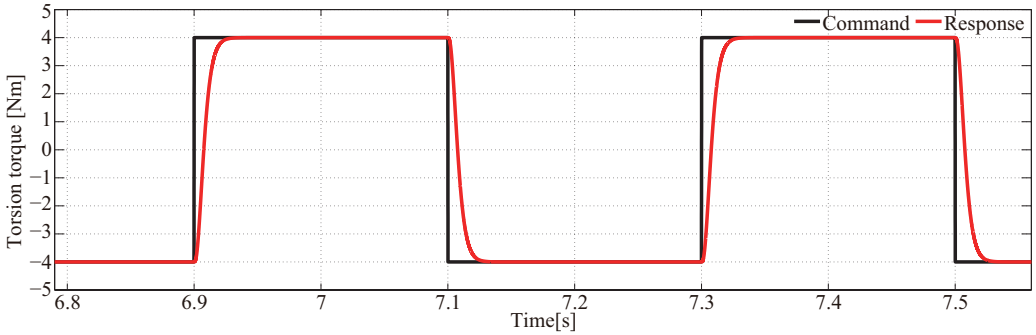


FigureA.7: Simulation result of I-P+$\omega_s$ feedback type TTC.

pseudo differentiator to differentiate the torsion torque as shown in app.Fig. A.2. By contrast, I-P+$\omega_s$ feedback type TTC in this paper uses a VDO to estimate the velocity deviation. The estimate of velocity deviation using a VDO is the same as actual velocity deviation in the case where there is no parameter variation. Thus, the transfer function of I-P+$\omega_s$ feedback type TTC considering VDO dynamics is the same as (3.12). This paper analyzes the bandwidth of the pseudo differentiator when designing control gains using the pole placement method. From (A.3), PID-type TTC is designed as

a 4th-order system. The control gains are calculated as follows:

$$\begin{aligned}
&(s+P_1)(s+P_2)(s+P_3)(s+P_4)\\
&= s^4 + (P_1+P_2+P_3+P_4)s^3 + (P_1P_2 + P_2P_3\\
&+ P_3P_4 + P_4P_1 + P_2P_4 + P_1P_3)s^2 + (P_1P_2P_3\\
&+ P_2P_3P_4 + P_3P_4P_1 + P_4P_1P_2)s + P_1P_2P_3P_4\\
&= s^4 + g_{t3}s^3 + g_{t2}s^2 + g_{t1}s + g_{t0} \qquad \text{(A.5)}
\end{aligned}$$

$$K_i = \frac{J_{mn}R_g}{K_{sn}K_{tn}g_{pd}}g_{t0} \qquad \text{(A.6)}$$

$$K_p = \frac{J_{mn}R_g}{K_{sn}K_{tn}g_{pd}}\left\{g_{t1} - \frac{K_{sn}K_{tn}K_i}{J_{mn}R_g} - \left(\frac{K_{sn}}{J_{mn}R_g^2} + \frac{K_{sn}}{J_{ln}}\right)g_{pd}\right\} \qquad \text{(A.7)}$$

$$K_d = \frac{J_{mn}R_g}{K_{sn}K_{tn}g_{pd}}\left\{g_{t2} - \left(\frac{K_{sn}K_{tn}K_p}{J_{mn}R_g} + \frac{K_{sn}}{J_{mn}R_g^2} + \frac{K_{sn}}{J_{ln}}\right)\right\} \qquad \text{(A.8)}$$

$$g_{pd} = g_{t3}. \qquad \text{(A.9)}$$

Control poles of the two types TTCs are set to 350 rad/s using the pole placement method. App. Fig. A.4 and app. Fig. A.5 show the Bode diagram and pole-zero assignment for the two types TTCs, respectively. In app. Fig. A.5, PID type TTC has two zeros, but I-P+$\omega_s$ feedback type TTC has none. Therefore, the zeros of PID type TTC change transient response. App. Fig. A.6 and app. Fig. A.7 show the torsion torque response for the two types TTCs. In these results, even though PID type TTC is designed by the pole placement method, the torsion torque response of PID type TTC is not better than that of I-P+$\omega_s$ feedback type TTC.

# B

# Analysis of Stable Contact Control System using on Force Impulse Based on Back-Forward Drivable Torsion Torque Control

## B.1 Analysis of Environmental Stiffness Variation in Command Response of Proposed Force Impulse Control

The contact motion should be stable with respect to various environmental perturbations. Therefore, this paper analyzes the robustness of the proposed approach with respect to the environmental stiffness variation ($K_e$ variation). App. Figs. B.1 and B.2 show the Bode diagram and pole-zero assignment in terms of the command response of the force impulse control system, for various of $K_e$. From app. Figs. B.1 and B.2, this paper concludes that the proposed force impulse control is robust to $K_e$ variations as strong as +500$\%$. Therefore, robustness with respect to environmental fluctuations is able to be achieved by setting the value of the nominal environmental stiffness, $K_{en}$, to be below the actual $K_e$ value, i.e., $K_{en} < K_e$.

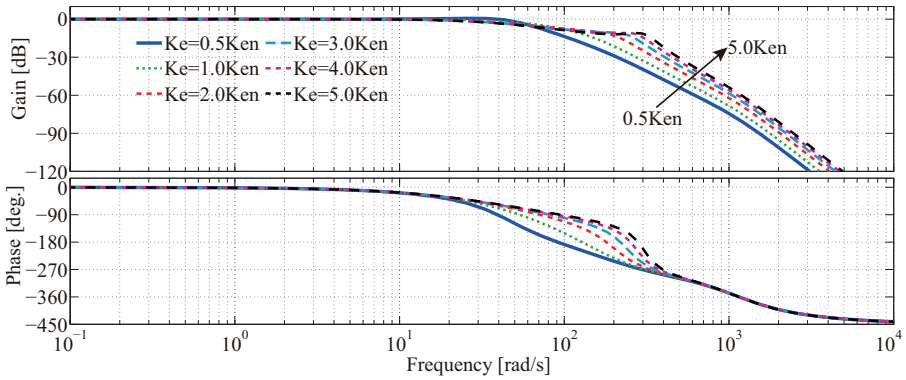


FigureB.1: Bode diagram of command response $P_e/P^{cmd}$ under $K_e$ variation.

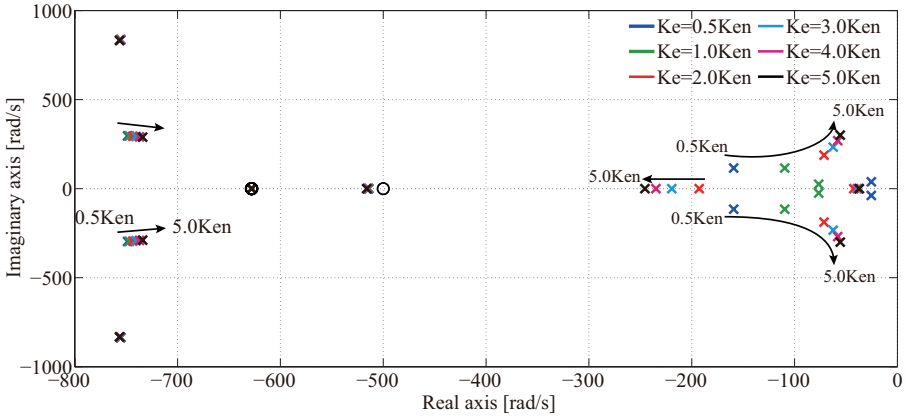


FigureB.2: Pole-zero assignment of command response $P_e/P^{cmd}$ under $K_e$ variation.

## B.2 Analysis of Load-side Inertia and Torsion Stiffness Variations in Proposed Force Impulse Control

To analyze the effect of parameter variations, this section evaluates the $J_l$ and $K_s$ variations in the proposed force impulse control system. app.Fig.B.3 shows the numerical simulation results of proposed force impulse control in case of $J_l$ and $K_s$ variations.

The simulation results of app.Fig.B.3 (a) and (b) in case of $J_l = 2.0J_{ln}$ has no negative response at zero second. Moreover, the force impulse and load-side torque responses around 0.1 s have a little vibration. On the other hand, the results of app.Fig.B.3 (a) and (b) in case of $J_l = 0.5J_{ln}$ indicate that

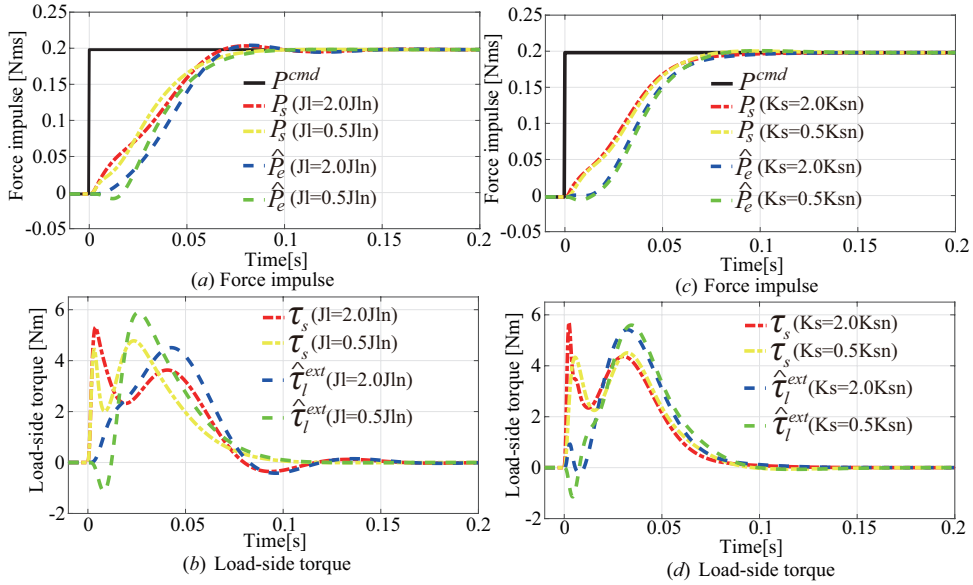


FigureB.3: Simulation results of proposed force impulse control in case of $J_l$ and $K_s$ variations. (a) Force impulse. (b) Load-side torque. (c) Force impulse. (d) Load-side torque.

there is a little negative response in the estimated external torque at zero second. Thus, $J_l$ variation is possible to affect the negative response of the estimated external torque at zero second in the force impulse control.

In app.Fig.B.3 (c) and (d), the simulation results in case of $K_s = 2.0K_{sn}$ has no negative response similar to that of $J_l = 2.0J_{ln}$ at zero second, but there is negative response at zero second in the simulation results in case of $K_s = 0.5K_{sn}$. However, both force impulse responses, considering $J_l$ and $K_s$ variations, follow the force impulse command, smoothly. Therefore, the proposed force impulse control is also stable against $J_l$ and $K_s$ variations of $\pm 100\%$.

## B.3 Comparison of Command Response in Motor-side Velocity and Force Impulse Controls

To compare the control bandwidth between the motor-side velocity control of the minor loop and the force impulse control, this section evaluates the Bode diagram of command response in terms

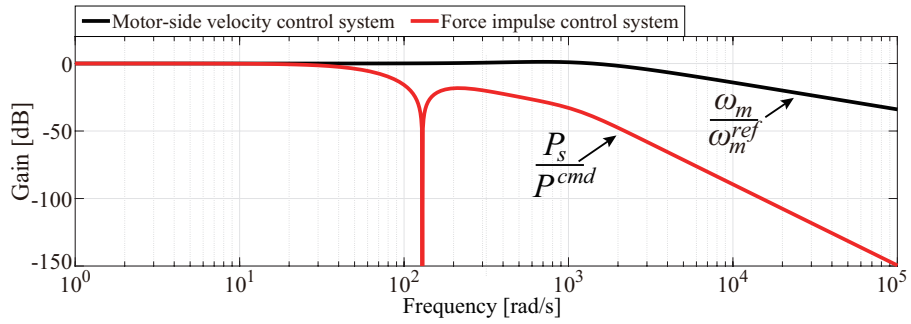


FigureB.4: Bode diagram of command response in both motor-side velocity control and force impulse control. Black and red lines are motor-side velocity control and force impulse control, respectively.

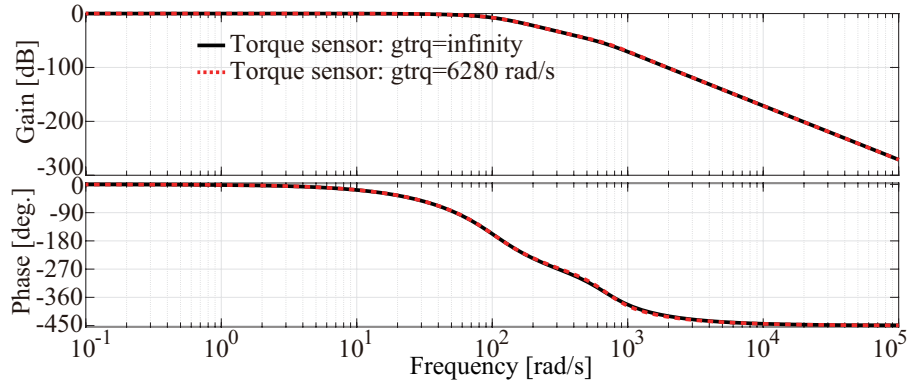


FigureB.5: Bode diagram in terms of command response of force impulse control considering bandwidth of torsion torque sensor.

of both motor-side velocity control and force impulse control. app.Fig.B.4 shows Bode diagram of command response in both motor-side velocity control and force impulse control.

In app.Fig.B.4, the bandwidth of motor-side velocity control is enough higher than that of force impulse control. Therefore, the transfer function of motor-side velocity control is regarded as one from the view of the force impulse controller and $J_m$ is able to be neglected.

## B.4 Verification of Command Response in Proposed Force Impulse Control Considering Bandwidth of Torsion Torque Sensor

This section indicates the Bode diagram show in app. Fig.B.5 in term of the command response of the proposed force impulse control considering bandwidth of the torsion torque sensor. Torque sensor dynamics is 1st-order LPF, i.e., $L_{trq}(s) = g_{trq}/(s + g_{trq})$. In app. Fig.B.5, the proposed force impulse control in case of ideal bandwidth and that of considering the bandwidth of torsion torque sensor, i.e., 1 kHz are same frequency characteristics. Therefore, bandwidth of the torsion torque sensor is able to be ignored in this paper.

# Acknowledgements

This Ph.D. thesis is the summary of research activities in the Doctoral course at Professor Ohishi ' s laboratory, Department of Science of Technology Innovation, Nagaoka University of Technology, Japan. I would never have been able to finish my dissertation without the guidance of my Professors, help from friends, and support from my family. First and foremost, I would like to express my deepest gratitude to my supervisor, Professor Kiyoshi Ohishi, for the insightful guidance and tremendous support of my study and research, for his patience, encouragement, enthusiasm, and immense knowledge. It is my honor to be a student under his supervision. I would like to thank Assistant Prof. Yuki Yokokura for his many helpful advice and many comments during my research work. I would like to thank Associate Prof. Toshimasa Miyazaki for his helpful advice and comments during my research work. I would like to sincerely thank Professor Toshiyuki Kanmachi, Professor Jun-ichi Itoh, Professor Yushi Miura, Associate Prof. Hitoshi Haga, Assistant Prof. Keisuke Kusaka for their invaluable comments and discussions to improve my research as well as to modify this thesis. I would like to thank Assistant Prof. Chowarit Mitsantisuk for providing valuable experience in overseas internships. I would like to thank all members in Ohishi laboratory for their kind help and support, for creating a good research environment and friendships.

I would like to give many thanks to my parents, Yutaka Kawai and Yukiko Kawai, and all other family members. I could not have finished the long journey of my study without their help and encouragement.

Finally, I would like to thank my beloved wife, Mai Kawai. She was always there cheering me up and stood by me through the good times and bad.

# References


［1］ “World Population Prospects 2019: Data Booklet,” in United Nations, Department of Economic and Social Affairs, Population Division (2019).

［2］ “https://www8.cao.go.jp/kourei/whitepaper/w-2018/html/zenbun/s1_1_1.html,” in Cabinet Office, Government of Japan (Sep. 21st, 2019, Access).

［3］ L. Basanez and J. Rosell : “Robotic polishing systems,” *IEEE Robotics and Automation Magazine*, Vol. 12, Issue 3, pp. 35–43, 2005.

［4］ A. Blomdell, G. Bolmsjo, T. Brogardh, P. Cederberg, M. Isaksson, R. Johansson, M. Haage, K. Nilsson, M. Olsson, T. Olsson, A. Robertsson and J. Wang : “Extending an industrial robot controller: implementation and applications of a fast open sensor interface,” *IEEE Robotics and Automation Magazine*, Vol. 12, Issue 3, pp. 85–94, 2005.

［5］ “https://ifr.org/ifr-press-releases/,” in IFR International Federation of Robotics (Sep. 21st, 2019, Access).

［6］ H. Nakamura, K. Ohishi, Y. Yokokura, N. Kamiya, T. Miyazaki, A. Tsukamoto : “Force Sensorless Fine Force Control Based on Notch-Type Friction-Free Disturbance Observers,” *IEEJ Journal of Indus., Appli.*, Vol. 7, No. 2, pp. 117–126, 2018.

［7］ S. Katsura and K. Ohishi : “Acquisition and Analysis of Finger Motions by Skill Preservation System,” *IEEE Trans. on Indus. Electro.*, Vol. 54, No. 6, pp. 3353–3361, 2007.

［8］ T. Nozaki, T. Mizoguchi, Y. Saito, D. Yashiro, and K. Ohnishi : “Recognition of Grasping Motion Based on Modal Space Haptic Information Using DP Pattern-Matching Algorithm,” *IEEE Trans. on Indus. Electro.*, Vol. 9, No. 4, pp. 2043–2051, 2013.

［9］ J. David, F. Heredia and J. Ota : "Semi-direct Teaching Method for Grasping Objects in Service Mobile Robot Systems - Teaching Data Generation," in *Proceedings in 2013 IEEE International Conference on Systems, Man, and Cybernetics, SMC2013*, 2013.

［10］ S. Robra-Gomez, V. M. Becerra, J. R. Llata, E. Gonzalez-Sarabia, C. Torre-Ferrero and J. Perez-Oria : "Working Together: A Review on Safe Human-Robot Collaboration in Industrial Environments," *IEEE Access*, Vol. 5, pp. 26754–26773, Nov. 2017.

［11］ G. B. Avanzini, N. M. Ceriani, A. M. Zanchettin, P. Rocco, and L. Bascetta : "Safety Control of Industrial Robots Based on a Distributed Distance Sensor," in *IEEE Trans. COntrol Syst. Technol.*, Vol. 22, No. 6, pp. 2127–2140, 2014.

［12］ C. H. Ko, K. Y. Young, Y. C. Huang and S. K. Agrawal : "Active and Passive Control of Walk-Assist Robot for Outdoor Guidance," *IEEE/ASME Trans. on Mechtro.*, Vol. 18, No. 3, pp. 1211–1220, June 2013.

［13］ Y. Kaida and T. Murakami : "An Approach to Sensorless Detection of Human Input Torque and Its Application to Power Assist Motion in Electric Wheelchair," *IEEJ Trans. on Industry Applications*, Vol. 126, No. 2, pp. 137–142, 2006.

［14］ F. Flacco and A. De Luca : "Safe Physical Human-Robot Collaboration," *Proceedings of 2013 IEEE/RSJ International Conference on Intelligent Robots and Systems*, p. 2072, 2013.

［15］ M. Geravand and F. Flacco and A. De Luca : "Human-robot physical interaction and collaboration using an industrial robot with a closed control architecture" in *Proc. of 2013 IEEE International Conference on Robotics and Automation*, pp. 4000–4007, 2013.

［16］ "DARPA Helps Paralyzed Man Feel Again Using a Brain-Controlled Robotic Arm, https://www.darpa.mil/news-events/2016-10-13," News event in Website of DARPA (Sep. 27th, 2019, Access).

［17］ T. Hayashi, H. Kawamoto, and Y. Sankai : "Control Method of Robot Suit HAL Working as Operator's Muscle Using Biological and Dynamical Information"

［18］ "https://www.cyberdyne.jp/," in website of CYBERDYNE, INC. (Sep. 27th, 2019, Access).

［19］ A. Zoss, H. Kazerooni, and A. Chu : "Biomechanical design of the Berkeley Lower Extremity Exoskeleton (BLEEX)" in *IEEE/ASME Trans. on Mechatronics*, Vol. 11, No. 2, pp. 128–138, 2006.

［20］ R. Steger, S.H. Kim, H. Kazerooni : "ControlScheme and Networked Control Architecture for the Berkeley Lower Extremity Exoskeleton (BLEEX)" in *Proc. of the 2006 IEEE Int. Conf. on Robotics and Automation*, pp. 3470–3476, 2006.

［21］ K. Kong and D. Jeon : "Design and Control of an Exoskeleton for the Elderly and Patients" in *IEEE/ASME Trans. Mechatronics*, Vol. 11, No. 4, pp. 428–432, 2006.

［22］ L. Chen, X. Wang, and W. L. Xu : "Inverse Transmission Model and Compensation Control of a Single-Tendon-Sheath Actuator" in *IEEE Trans. on Indus. Electro.*, Vol. 61, No. 3, pp. 1424–1433, 2014.

［23］ Q. Wu, X. Wang, L. Chen, and F. Du : "Transmission Model and Compensation Control of a Double-Tendon-Sheath Actuation System" in *IEEE Trans. on Indus. Electro.*, Vol. 62, No. 3, pp. 1424–1433, 2015.

［24］ K. Kong, H. Moon, B. Hwang, D. Jeon and M. Tomizuka : "Impedance Compensation of SUBAR for Back-Drivable Force-Mode Actuation," *IEEE Transactions on Robotics*, Vol. 25, No. 3, pp. 512–521, 2009.

［25］ Y. Hsieh and Y. Huang and K. Young and C. Ko and S. K. Agrawal : "Motion Guidance for a Passive Robot Walking Helper via User's Applied Hand Forces" in *IEEE Transactions on Human-Machine Systems*, Vol. 46, No. 6, pp. 869–881, 2016.

［26］ "https://www.meti.go.jp/press/2017/10/20171012001/20171012001.html," in Ministry of Economy, Trade and Industry (Sep. 23nd, 2019, Access).

［27］ K. Suzumori : "Backdrivability of Robots and Actuators," *Journal of RSJ*, Vol. 31, No. 6, pp. 548–551, 2013 (in Japanese).

［28］ H. Minakata : "Development of Leg Extender Exoskeleton with Active Ankle Joint," *IEEJ Trans. on Industry Applications*, Vol. 134, No. 3, pp. 252–257, 2014.

［29］ P. M. Wensing, A. Wang, S. Seok, D. Otten, J. Lang, and S. Kim : "Proprioceptive Actuator Design in the MIT Cheetah: Impact Mitigation and High-Bandwidth Physical Interaction for Dynamic Legged Robots," *IEEE Trans. on Robotics*, Vol. 33, No. 3, pp. 509–519, 2017.

［30］ H. Kaminaga, T. Yamamoto, J. Ono, and Y. Nakamura : "Anthropomorphic Robot Hand With Hydrostatic Actuators," in *Proc. of 7th IEEE-RAS Int. Conf. on Humanoid Robots*, pp. 36–41, 2007.

［31］ H. Kaminaga, S. Otsuki and Y. Nakamura : "Development of high-power and backdrivable linear electro-hydrostatic actuator," in *Proceedings in IEEE-RAS International Conference on Humanoid Robots*, pp. 973–978, 2014.

［32］ H. Kaminaga, K. Odanaka, Y. ando, S. Otsuki and Y. Nakamura : "Evaluations on contribution of backdrivabilty and force measurement performance on force sensitivity of actuators," in *Proceedings in IEEE/RSJ Int. Conf. on Intelligent Robots and Systems, Tokyo*, pp. 4472–4477, 2013.

［33］ H. Kaminaga, T. Ko, S. Yorita, S. Sato, R. Masumura, M. Komagata, T. Ishikawa, T. Miyatake, and Y. Nakamura : "Enhancement of Mechanical Strength, Computational Power, and Heat Management for Fieldwork Humanoid Robots," in *Proc. of IEEE-RAS 16th Int. Conf. on Humanoid Robots*, pp. 786–793, 2016.

［34］ G. Pratt and M. Williamson : "Series elastic actuators," in *Proceedings in IEEE IROS*, pp. 399–406, 1995.

［35］ K. Kong, J. Bae and M. Tomizuka : "Control of Rotary Series Elastic Actuator for Ideal Force-Mode Actuation in Human-Robot Interaction Applications," *IEEE/ASME Transactions on Mechatronics*, Vol. 14, No. 1, pp. 105–118, 2009.

［36］ K. Miura and S. Katsura : "Experimental validation of forward- and back-drivable characteristics on series clutch actuators using acceleration control," in *Proc. of 2016 IEEE International Conference on Advanced Intelligent Mechatronics (AIM)*, 716–720, 2016.

［37］ Y. Fujimoto, T. Kominami and H. Hamada : "Development and Analysis of a High Thrust

Force Direct-Drive Linear Actuator," *IEEE Trans. on Ind. Electron.*, Vol. 56, No. 5, pp. 1383–1392, May 2009.

[38] C. Mitsantisuk, K. Ohishi and S. Katsura : "Control of Interaction Force of Twin Direct-Drive Motor System Using Variable Wire Rope Tension With Multisensor Integration," *IEEE Trans. on Industrial Electronics*, Vol. 59, No. 1, pp. 498–510, 2012.

[39] N. Motoi and R. Kubo : "Human-Machine Cooperative Grasping/Manipulating System Using Force-based Compliance Controller with Force Threshold," *IEEJ Trans. on Industry Applications*, Vol. 5, No. 2, pp. 39–46, 2016.

[40] T. Yoshioka, A. Yabuki, Y. Yokokura, K. Ohishi, T. Miyazaki and T. T. Phuong : "Stable Force Control of Industrial Robot Based on Spring Ratio and Instantaneous State Observer," *IEEJ Journal of Industry Applications*, Vol. 5, No. 2, pp. 132–140, 2015.

[41] G. Zhang and J. Furusho : "Control of Robot Arms Using Joint Torque Sensors ," *IEEE Trans. on Control Systems Magazine*, Vol. 18, No. 1, pp. 48–55, 1998.

[42] Y. Kuroki, Y. Kosaka, T. Takahashi, E. Niwa, H. Kaminaga and Y. Nakamura : "Cr-N Alloy Thin-Film Based Torque Sensors and Joint Torque Servo Systems for Compliant Robot Control," in *Proceedings in The IEEE International Conference on Robotics and Automation 2013, ICORA2013-KARLSRUHE*, pp. 4939–4943, 2013.

[43] S. Yamada and H. Fujimoto : "Precise Joint Torque Control Method for Two-inertia System with Backlash Using Load-side Encoder," in *IEEJ Journal of Industry Applications*, Vol. 8, No. 1, pp. 75–83, 2019.

[44] H. Zhang, S. Ahmad and G. Liu : "Torque Estimation for Robotic Joint With Harmonic Drive Transmission Based on Position Measurements," in *IEEE Trans. on Robotics*, Vol. 31, No. 2, pp. 322–330, 2015.

[45] T.Ishida and A. Takanishi : "A Robot Actuator Development With High Backdrivability," in *Proceedings in IEEE Conf. on Robotics, Automation and Mechatronics, Bangkoku*, pp. 1–6, 2006.

[46] A. Albu-Schaffer, C. Ott and G. Hirzinger : "A Unified Passivity-based Control Framework for Position, Torque and Impedance Control of Flexible Joint Robots" in *The Int. J. of Robotics Research*, Vol. 26, No. 1, pp. 23–39, Jan. 2007.

[47] A. Calanca, R. Muradore, and P. Fiorini: "A Review of Algorithms for Compliant Control of Stiff and Fixed-Compliance Robots" in *IEEE/ASME Transactions on Machatronics*, Vol. 21, No. 2, Apl. 2016

[48] J. K. Salisbury : "Active stiffness control of a manipulator in Cartesian coordinates" in *Proc. of 19th IEEE Conf. Decis. and Control*, pp. 95–100, 1980.

[49] C. Ott, A. Albu-Schaffer, A. Kugi and G. Hirzinger : "On the Passivity-Based Impedance Control of Flexible Joint Robots" in *IEEE Trans. on Robotics*, Vol. 24, No. 2, pp. 416–429, Apr. 2008.

[50] N. Hogan : "Impedance Control: An Approach to Manipulation: Part I - Theory" in *ASME J. Dynam. Syst., Meas., Contro.*, Vol. 107, pp. 1–7, 1985.

[51] N. Hogan : "Impedance Control: An Approach to Manipulation: Part II - Implementation" in *ASME J. Dynam. Syst., Meas., Contro.*, Vol. 107, pp. 8–16, 1985.

[52] N. Hogan : "Impedance Control: An Approach to Manipulation: Part III - Applications" in *ASME J. Dynam. Syst., Meas., Contro.*, Vol. 107, pp. 17–24, 1985.

[53] S. Tungpataratanawong, K. Ohishi, T. Miyazaki and S. Katsura : "Force Sensor-less Workspace Virtual Impedance Control Considering Resonant Vibration for Industrial Robot" in *IEEJ Trans. on Ind. Appl.*, Vol. 127, No. 1, pp. 1–8, 2007.

[54] H. Kazerooni and T. Sheridan and P. Houpt : "Robust compliant motion for manipulators, part I: The fundamental concepts of compliant motion" in *IEEE Journal on Robotics and Automation*, Vol. 2, No. 2, pp. 83–92, 1986.

[55] H. Kazerooni and P. Houpt and T. Sheridan : "Robust compliant motion for manipulators, part II: Design method" in *IEEE Journal on Robotics and Automation*, Vol. 2, No. 2, pp. 93–105, 1986.

[56] R. Volpe and P. Khosla : "Experimental verification of a starategy for impact control" in *Proc. of IEEE Int. Conf. Rob. and Autom.*, pp. 1854–1860, 1991.

[57] H. Kazerooni and P. Houpt and T. Sheridan : "The fundamental concepts of robust compliant motion for robot manipulators" in *Proc. of 1986 IEEE International Conference on Robotics and Automation*, Vol. 3, pp. 18–427, 1986.

[58] N. Shimada, T. Yoshioka, K. Ohishi, T. Miyazaki and Y. Yokokura : "Variable Dynamic Threshold for Jerk Signal for Contact Detection in Industrial Robot without Force Sensor" in *IEEJ Transactions on Industry Applications*, Vol. 133, No. 3, pp. 368–377, 2013.

[59] N. Shimada, T. Yoshioka, K. Ohishi and T. Miyazaki : "Fine-Motion-Control for Realizing High-Accuracy and High-Speed Contact Motion of Industrial Robots by Employing Sensorless Force Control" in *IEEJ Transactions on Industry Applications*, Vol. 132, No. 3, pp. 322–332, 2012.

[60] W. Maebashi, K. Ito, K. Matsuo and M. Iwasaki : "High-Precision Sensorless Force Control by Mode Switching Controller for Positioning Devices with Contact Operation" in *IEEJ Transactions on Industry Applications*, Vol. 134, No. 5, pp. 535–543, 2014.

[61] A. De Luca and R. Mattone: "Actuator Failure Detection and Isolation Using Generalized Momenta" in *ICRA*, 2003

[62] J. Vorndamme, M. Schappler, A. Todtheide and S. Haddadin: "Soft Robotics for the Hydraulic Atlas Arms: Joint Impedance Control with Collision Detection and Disturbance Compensation" in *2016 IEEE/RSJ International Conference on Intelligent Robots and Systems (IROS)*, Oct. 2016

[63] S. Haddadin, A. De Luca and A. Albu-Schaffer : "Robot Collisions: A Survey on Detection, Isolation, and Identification" in *IEEE Trans. on Robotics*, Vol. 33, No. 6, pp. 1292–1312, Dec. 2017.

[64] S. Katsura and K. Ohnishi : "Force Servoing by Flexible Manipulator Based on Resonance Ratio Control," *IEEE Trans. on Indus. Electronics*, Vol. 54, No. 1, pp. 539–547, 2007.

[65] S. Morimoto, M. Sugimoto, Y. Takeda, T. Hirasa : "Vibration Suppression and Pole Assignment of Two-Mass System by State Feedback Control," in *IEEJ Transactions on Electronics, Information and Systems*, Vol. 113, No. l0, pp. 781–788, 1993.

[66] I. H. Akyuz, E. Yolacan, H. M. Ertunc and Z. Bingul : "PID and State Feedback Control of a Single-Link Flexible Joint Robot Manipulator," in *Proc. of the 2011 IEEE Int. Conf. on Mechatronics*, pp. 409–414, 2011.

[67] M. Matsuoka and T. Murakami and K. Ohnishi : "Vibration Suppression and Disturbance Rejection Control of a Flexible Link Arm," *Proceedings of IECON '95 - 21st Annual Conference on IEEE Industrial Electronics*, Vol. 2, pp. 1260–1265, 1995.

[68] S. Oh and K. Kong : "Two-Degree-of-Freedom Control of a Two-Link Manipulator in the Rotating Coordinate System," *IEEE Transactions on Industrial Electronics*, Vol. 62, No. 9, pp. 5598–5607, 2015.

[69] A. Suzumura and Y. Fujimoto and T. Murakami and R. Oboe : "A General Framework for Designing SISO-Based Motion Controller With Multiple Sensor Feedback," *IEEE Transactions on Industrial Electronics*, Vol. 63, No. 12, pp. 7607–7620, 2016.

[70] E. Saito and S. Katsura : "Vibration Control of Two-Mass Resonant System Based on Wave Compensator," in *IEEJ Journal of Industry Applications*, Vol, 132, No. 4, pp. 473–479, 2012.

[71] E. Saito, S. Katsura : "Position Control of Resonant System with Load Force Suppression Using Wave Observer," *IEEJ Journal of Industry Applications*, Vol. 3, No. 1, pp. 18–25, 2014.

[72] K. Yuki, T. Murakami, and K. Ohnishi : "Vibration control of 2 mass resonant system by resonance ratio control," *IEEJ Transactions on Industry Applications*, Vol. 113, No. l0, pp. 1162–1169, 1993.

[73] Y. Hori : "2-Inertia System Control using Resonance Ratio Control and Manabe Polynomials," in *IEEJ Journal of Industry Applications*, Vol, 114, No. 10, pp. 1038–1045, 1994.

[74] Y. Hori, H. Sawada and Y. Chun : "Slow resonance ratio control for vibration suppression and disturbance rejection in torsional system," in *IEEE Trans. on Ind. Electron.*, Vol, 46, No.

1, pp. 162–168, 1999.

[75] K. Ohishi, K. Ohnishi, and K. Miyachi : "Torque-Speed Regulation of DC Motor Based on Load Torque Estimation Method," *Proc. IEEJ Int. Power Electron. Conf.*, pp. 1209-1216, Mar. 1983.

[76] K. Ohnishi, M. Shibata, and T. Murakami : "Motion Control for Advanced Mechatronics," *IEEE/ASME Trans. Mechatronics*, Vol. 1, No. 1, pp. 56–67, 1996.

[77] K. Sakata, H. Asaumi, K. Hirachi, K. Saiki and H. Fujimoto : "Self Resonance Cancellation Techniques for a Two-Mass System and Its Application to a Large-Scale Stage," *IEEJ Journal of Industry Applications*, Vol. 3, No. 6, pp. 455–462, 2014.

[78] Y. Yoshiura, Y. Kaku : "Vibration Suppression Control by Acceleration Sensor's Feedback," *IEEJ Transaction on Industrial Applications*, Vol. 134, No. 9, pp. 801–806, 2014.

[79] W. L. Xu, J. D. Han, and S. K. Tso : "Experimental study of contact transition control incorporating joint acceleration feedback" in *IEEE/ASME Trans. Mechatronics*, Vol. 5, No. 3, pp. 292–301, 2000.

[80] N. Kobayashi and T. Murakami : "Comparison of Force Control Performance Based on Only Acceleration Sensor with KF/EKF" in *IEEJ Transaction of Indus. Appli.*, Vol. 4, No. 5, pp. 559–567, 2015.

[81] K. Irie, S. Katsura and K. Ohishi : "Wideband Motion Control by Position and Acceleration Input Based Disturbance Observer" in *IEEJ Trans. IA*, Vol. 127, No. 6, pp. 579–586, 2007.

[82] A. Yabuki, K. Ohishi, T. Miyazaki and Y. Yokokura : "Force Control Including Contact Process Using Acceleration-sensor-based Instantaneous State Observer for High-stiffness Gear Drive" in *Proc. of 2016 IEEE 25th Int. Symp. on Indus. Electro. (ISIE)*, pp. 651–656, 2016.

[83] "http://www.robotec.tokyo/en/uniservo.html," in ROBOTEC Corporation, Japan.

[84] Y. Kawai, Y. Yokokura, K. Ohishi and P. Boonwong: "Analysis and Realization of Robot Actuator Based on Bidirectional Drivability Matrix," in *Proceedings in The 20th World Congress of the International Federation of Automatic Control(IFAC2017 World Congress)*, pp. 12553–

12558, 2017.

[85] E. Sariyildiz and K. Ohnishi : "Stability and Robustness of Disturbance-Observer-Based Motion Control Systems," in *IEEE Trans. on Ind. Electron.*, Vol. 62, No. 1, pp. 414–422, 2015.

[86] E. Sariyildiz and K. Ohnishi : "On the Explicit Robust Force Control Via Disturbance Observer," *IEEE Transactions on Industrial Electronics*, Vol. 62, No. 3, pp. 1581–1589, 2015.

[87] H. Kurumatani and S. Katsura : "Design of Nominal Parameters for Robust Sensorless Force Control Based on Disturbance Observer," *IEEJ Journal of Industry Applications*, Vol. 8, No. 2, pp. 342–351, 2019.

[88] N. Motoi and T. Shimono and R. Kubo and A. Kawamura : "Task Realization by a Force-Based Variable Compliance Controller for Flexible Motion Control Systems," *IEEE Transactions on Industrial Electronics*, Vol. 61, No. 2, pp. 1009–1021, 2014.

[89] S. Katsura and J. Suzuki and K. Ohnishi : "Pushing Operation by Flexible Manipulator Taking Environmental Information Into Account," *IEEE Transactions on Industrial Electronics*, Vol. 53, No. 5, pp. 1688–1697, 2006.

[90] S. Manabe : "The coefficient diagram method," in *Proc. in The 4th IFAC Symposium on Automatic Cont. in Aerospace*, pp. 199–210, 1998.

[91] S. Manabe : "Brief tutorial and survey of coefficient diagram method," in *Proc. in The 4th Asian Control Conference*, 2002.

[92] W. S. Levine : "The CONTROL HANDBOOK," in *A CRC Handbook Published in Cooperation with IEEE Press*, ISBN 0-8493-8570-9, Chapter 9.4, pp. 152–156, 1996.

[93] C. Chen, F. L. Lewis, S. Xie, H. Modares, Z Liu, S. Zuo, and A. Davoudi : "Resilient adaptive and H $\infty$ controls of multi-agent systems under sensor and actuator faults" in *Automatica*, Vol. 102, pp. 19–26, 2019.

[94] Y. Kawai, Y. Yokokura, K. Ohishi and P. Boonwong: "High-Robust Acceleration Control Using Force and Position Sensors Integrated Disturbance Observer," in *Proc. of IECON 2016*

*- 42nd Annual Conf. of the IEEE Ind. Electron. Society*, pp. 5802-5807, 2016.

[95] M. Ikeda., M. Koujitani and T. Kida: "Optimality of Direct Velocity and Displacement Feedback for Large Space Structures with Collocated Sensors and Actuators," in *Proc. of The 12th IFAC World Congress*, Vol. 26, No. 2, Part 2, pp. 495-498, 1993.

[96] S. Eppinger and W. Seering : "Understanding bandwidth limitations in robot force control" in *Proceedings. 1987 IEEE International Conference on Robotics and Automation*, Vol. 4, pp. 904–909, 1987.

[97] S. Eppinger and W. Seering : "On Dynamic Models of Robot Force Control" in *Proc. of the IEEE Conference on Robotics and Automation*, Vol. 4, pp. 29–34, 1986.

[98] S. D. Eppinger and W. P. Seering: "Three dynamic problems in robot force control," in *IEEE Trans. on Robotics and Automation*, Vol. 8, No. 6, pp. 751-758, 1992.

[99] S. Katsura and Y. Matsumoto and K. Ohnishi : "Analysis and Experimental Validation of Force Bandwidth for Force Control," *IEEE Transactions on Industrial Electronics*, Vol. 53, No. 3, pp. 922–928, 2006.

[100] S. Katsura, Y. Matsumoto, and K. Ohnishi : "Modeling of Force Sensing and Validation of Disturbance Observer for Force Control" in *IEEE Trans. Ind. Electron.*, Vol. 54, No. 1, pp. 530–538, Feb. 2007.

[101] M. Ruderman, W. Maebashi and M. Iwasaki: "Semi-dual Loop Control of Two-Mass Actuator System using Luenberger State Observer," in *Proc. of IECON 2013 - 39th Annual Conf. of the IEEE Ind. Electron. Society*, pp. 6561-6556, 2013.

[102] H. Mizukawa and Y. Nakamura: "Motion Control of Humanoid Robot Based on Control of Impulse" in *SI2003*, 2003 (in Japanese).

[103] E. V. Poorten and Y. Yokokohji: "Rendering a Rigid Virtual World through an Impulsive Haptic Interface" in *Proceedings in 2006 IEEE/RSJ International Conference on Intelligent Robots and Systems (IROS)*, 2006

[104] S. Sakaino, T. Sato and K. Ohnishi: "A Stability Analysis of Force Control Based on

Momentum" in *IEEJ Trans. IA*, Vol. 129, No. 6, pp. 614–621, 2009

[105] S. Sakaino and K. Ohnishi: "A Composition of Decoupling Motion Controller based on Momentum and Its Application for Singular Configurations" in *Proc. the 33rd Annual Conference of the IEEE Ind. Electron.*, pp. 2331–2336, 2007

[106] S. Sakaino and K. Ohnishi: "A Composition of Dynamic Force Control System Based on Momentum" in *IEEJ Trans. IA*, Vol. 128, pp. 694–700, 2008

# List of Achievements

## Journals

1. **Yusuke Kawai**, Yuki Yokokura, Kiyoshi Ohishi, and Toshimasa Miyazaki, “Smooth Human Interaction Control using Torsion Torque Controller and Motor-side Normalization Compensator Focusing on Back-forward Drivability,”, IEEJ Journal of Industry Applications, Vol. 8, No. 2, pp. 322–333, 2019.
2. **Yusuke Kawai**, Yuki Yokokura, Kiyoshi Ohishi, and Toshimasa Miyazaki, “Equivalent Resonance Ratio Control of Two-Spring System for Stable Contact Motion of Industrial Robot,”, IEEJ Journal of Industry Applications, Vol. 9, No. 1, pp. 51–60, 2020.

## International Conference (Peer review)

1. **Yusuke Kawai**, Yuki Yokokura, Kiyoshi Ohishi, Kotaro Saito and Atsushi Shimamoto : “Equivalence of Resonance Ratio and I-PD Controllers in Zero Stiffness Torque Control for Soft Robot”, The 41th Annual Conference of the IEEE Industrial Electronics Society (IECON2015-Yokohama), pp. 1424-1429, (2015.11) (Oral session)
2. **Yusuke Kawai**, Yuki Yokokura, Kiyoshi Ohishi, Kotaro Saito and Atsushi Shimamoto : “High Back-drivable Pseudo I-PD Torque Control Using Load-side Torque Observer With Torsion Torque Sensor”, 2016 IEEE 14th International Workshop on Advanced Motion Control (AMC2016-Auckland), pp. 175-180, (2016.4) (Oral session)
3. **Yusuke Kawai**, Yuki Yokokura, Kiyoshi Ohishi and Pattawan Boonwong : “High-Robust Acceleration Control Using Force and Position Sensors Integrated Disturbance Observer”, The 42th Annual Conference of the IEEE Industrial Electronics Society (IECON2016-Florence),

pp. 5802–5807, (2016.10) (Oral session)

4. **Yusuke Kawai**, Yuki Yokokura, Kiyoshi Ohishi and Toshimasa Miyazaki : ”Design Strategy of MIMO System Based on Bidirectional Drivability Matrix”, The 3rd IEEJ international workshop on Sensing, Actuation, Motion Control, and Optimization (SAMCON2017-Nagaoka), (2017.3) (Oral session)
5. **Yusuke Kawai**, Yuki Yokokura, Kiyoshi Ohishi and Pattawan Boonwong : ”Analysis and Realization of Robot Actuator Based on Bidirectional Drivability Matrix”, The 20th World Congress of the International Federation of Automatic Control (IFAC2017 World Congress, Toulouse), Volume 50, Issue 1, July 2017, pp. 12047-12052,
6. **Yusuke Kawai**, Yuki Yokokura, Kiyoshi Ohishi and Toshimasa Miyazaki : ”Forward-back and Back-forward Drivable Controls for Human-robot Interaction”, 2018 IEEE 15th International Workshop on Advanced Motion Control (AMC2018-Tokyo), pp. 669–674, (2018.3)
7. **Yusuke Kawai**, Chowarit Mitsantisuk, Hikaru Matsui, Kiyoshi Ohishi and Yuki Yokokura : ”Workspace Force Control using Workspace PAIDO Based on Workspace Modeling”, The 4th IEEJ international workshop on Sensing, Actuation, Motion Control, and Optimization (SAMCON2018-Tokyo), (2018.3) (Poster session)
8. **Yusuke Kawai**, Yuki Yokokura, Kiyoshi Ohishi and Toshimasa Miyazaki : ”Analysis of Estimation Performance of Load-side Torque and Load-side Velocity Observers for Human Interaction Control Based on Torsion Torque Control”, 2018 IEEE/ASME International Conference on Advanced Intelligent Mechatronics (AIM2018-Auckland, NewZealand), pp. 652–657, (2018.7)
9. **Yusuke Kawai**, Yuki Yokokura, Kiyoshi Ohishi and Toshimasa Miyazaki : ”Force Impulse Control Based on Resonance Ratio Control for Anti-bouncing Motion”, The 5th IEEJ international workshop on Sensing, Actuation, Motion Control, and Optimization (SAMCON2019-Chiba), (2019.3) (Oral session)
10. **Yusuke Kawai**, Yuki Yokokura, Kiyoshi Ohishi and Toshimasa Miyazaki : ”Realization of

Resonance Ratio Control Focusing on Duality of Torque and Velocity for Two-Inertia System with Environment", The 28th IEEE International Symposium on Industrial Electronics(ISIE2019-Vancouver, Canada), pp. 641–646, (2019.6) (Oral session)

## Domestic Conference (As a first author)

1. **Yusuke Kawai**, Yuki Yokokura，Kiyoshi Ohishi，Kotaro Saito，Atsushi Shimamoto : "High Performance Back-drivable Torque Control with Torsion Torque Sensing in Load-side Torque Feedback"，The 2015 IEEJ Workshop of Mechatronics Control "Real World Haptics"，MEC-15-008，pp.41-46，Tokyo，(2015.8) (in Japanese)
2. **Yusuke Kawai**, Yuki Yokokura，Kiyoshi Ohishi，Kotaro Saito，Atsushi Shimamoto : "Equivalence between Resonance Ratio Control and I-PD Control in Zero Stiffness Torque Control for Soft Robot"，The 2015 IEEJ Industry Applications Society Conference，JIASC2015-R2-1, 2-1，Oita，(2015.9) (in Japanese)
3. **Yusuke Kawai**, Yuki Yokokura, Kiyoshi Ohishi, Toshimasa Miyazaki, Kotaro Saito, Atsushi Shimamoto : "Consideration of High Stabilization in the Back-drivable Control of the Servo Motor with a Torque Sensor"，The 2015 IEEJ Niigata Conference，NGT-15-087, Nagaoka，(2015.10) (in Japanese)
4. **Yusuke Kawai**, Yuki Yokokura and Kiyoshi Ohishi : "Analysis of Back-drivability in Load-side Torque Control on New Index"，The 2016 IEEJ Industry Applications Society Conference，JIASC2016-HB-1, 2-14，Maebashi，(2016.9) (in Japanese)
5. **Yusuke Kawai**, Yuki Yokokura and Kiyoshi Ohishi : "Consideration of Back-drivable Control Focused on Load-side Acceleration"，The 2016 IEEJ Workshop of Mechatronics Control "Real World Haptics"，MEC-16-006，pp.25-30，Tokyo，(2016.9) (in Japanese)
6. **Yusuke Kawai**, Yuki Yokokura and Kiyoshi Ohishi : "Analysis of Actuator with Bidirectional Drivability Matrix Characteristics"，The 2016 IEEJ Niigata Conference，NGT-16-044, Nagaoka，(2016.11) (in Japanese)
7. **Yusuke Kawai**, Yuki Yokokura，Kiyoshi Ohishi and Toshimasa Miyazaki : "Back-forward

Drivable Torque Control Based on Torsion Torque Control Using Motor-side Normalization Compensator”，The 2017 IEEJ Industry Applications Society Conference，R2-3-2-18，Hakodate，(2017.8) (in Japanese)

8. **Yusuke Kawai**, Yuki Yokokura，Kiyoshi Ohishi and Toshimasa Miyazaki : “Force Control Based on Contact Vibration Suppression Controller”，The 35th Annual Conference of the RSJ (RSJ2017)，2G2-04，Kawasaki，(2017.9) (in Japanese)
9. **Yusuke Kawai**, Yuki Yokokura，Kiyoshi Ohishi and Toshimasa Miyazaki : “Broadband of Torsion Torque Control Using Load-side Velocity Observer for High-response Back-forward Drivability”，The 2018 IEEJ Industry Applications Society Conference，(2018.8) (in Japanese)
10. **Yusuke Kawai**, Shunsuke Suzuki, Yuki Yokokura，Kiyoshi Ohishi, Toshimasa Miyazaki : “Consideration of control design focused on bidirectional drivability matrix”，The 2018 IEEJ Workshop of Mechatronics Control “Real World Haptics”, MEC-18-024, pp.49-54，Tokyo，(2018.9) (in Japanese)
11. **Yusuke Kawai**, Yuki Yokokura，Kiyoshi Ohishi and Toshimasa Miyazaki : “Stable Contact Control Using Force Control of Two-Spring System Focusing on Duality”，The 2019 IEEJ Industry Applications Society Conference，Nagasaki, 2019 (in Japanese).
12. **Yusuke Kawai**, Yuki Yokokura, Kiyoshi Ohishi, Toshimasa Miyazaki : “Human-Interaction Robot by Realization of Stable Force Control Techniques for Enabling Interaction with Various Environments”，The 10th Conf. on Transdisciplinary Federation of Science and Technology (TraFST2019)，Nagaoka, 2019 (in Japanese).

Doctor of Engineering, Doctoral Thesis

The Back-Forward Drivable Torsion Torque Control

of Two-Inertia System For Environment Interaction

Publication February 2020

Author Yusuke KAWAI